Technische Universität München
Institut für Energietechnik

Lehrstuhl für Thermodynamik

Experimental Study on the Identification of Heat Transfer Characteristics for Subcooled Flow Boiling of Novec 649

Moritz Till Bruder

Vollständiger Abdruck der von der Fakultät für Maschinenwesen der Technischen Universität München zur Erlangung des akademischen Grades eines

DOKTOR – INGENIEURS

genehmigten Dissertation.

Vorsitzender:

   Prof. Dr.-Ing. Wolfram Volk

Prüfer der Dissertation:

   1. Prof. Dr.-Ing. Thomas Sattelmayer
   2. Prof. Dr.-Ing. habil. Andrea Luke

Die Dissertation wurde am 27.06.2019 bei der Technischen Universität München eingereicht und durch die Fakultät für Maschinenwesen am 20.12.2019 angenommen.

Acknowledgments

Wesentliche Teile dieser Dissertation wurden vom Autor bereits vorab als Konferenz- und Zeitschriftenbeiträge veröffentlicht [1–10]. Alle Vorveröffentlichungen sind entsprechend der gültigen Promotionsordnung ordnungsgemäß gemeldet. Sie sind deshalb nicht zwangsläufig im Detail einzeln referenziert. Vielmehr wurde bei der Referenzierung eigener Vorveröffentlichungen Wert auf Verständlichkeit und inhaltlichen Bezug gelegt.

Parts of this Ph.D. thesis were published by the author beforehand in conference proceedings, journal papers, and reports [1–10]. All of these prior printed publications are registered according to the valid doctoral regulations. However, not all of them are quoted explicitly everywhere as they are part of this present work being official documents. Whether these personal prior printed publications were referenced, depended on maintaining comprehensibility and providing all necessary context.

Kurzfassung

Die Wärmeübertragung durch Blasensieden ist durch das Auftreten der kritischen Wärmestromdichte limitiert. Der darauffolgende schnelle Anstieg der Oberflächentemperatur kann zur Zerstörung des wärmeabgebenden Bauteils führen und katastrophale Folgen haben. Die präzise Vorhersage des Auftretens der kritischen Wärmestromdichte ist daher von hoher technischer Bedeutung. Diese experimentelle Studie trägt für unterkühltes Strömungssieden anhand detaillierter lokaler Messdaten entlang der Siedekurve zu einem tieferen Verständnis der Prozesse bei, die für das Auftreten der kritischen Wärmestromdichte ursächlich sind. Das Siedeverhalten des Kältemittels Novec 649 wurde in einem rechteckigen Strömungskanal an zwei Heizerkonfigurationen untersucht - einem wandbündigen Kupferheizer und einem kupferbeschichteten Einzelstabheizer aus Edelstahl. So konnte der Einfluss des unterschiedlichen Heizermaterials auf den Siedeprozess unabhängig von Oberflächeneffekten untersucht werden. Neben den Messgrößen Wärmestromdichte und Oberflächentemperatur werden quantitative Daten zum Verhalten der Dampfphase entlang der Siedekurve präsentiert. Mit diesen Daten wurde die Vorhersagegenauigkeit von drei etablierten mechanistischen Modellen zum Auftreten der kritischen Wärmestromdichte untersucht. Keines der Modelle konnte die experimentell ermittelte kritische Wärmestromdichte zufriedenstellend vorhersagen. Es wurden zusätzlich zwei neuere mechanistische Modelle zur Vorhersage der kritischen Wärmestromdichte untersucht. Deren Kernannahmen konnten mit den experimentellen Daten bestätigt werden. Ein Vergleich der experimentellen Daten beider Heizerkonfigurationen wird präsentiert. Es wurde beobachtet, dass die gesamte Siedekurve mit hoher Genauigkeit mit der Dreiphasenkontaktliniendichte auf der Siedeoberfläche korreliert. Das Verhalten der Dampfphase beim Zusammenbruch der Wärmeübertragung bei Auftreten der kritischen Wärmestromdichte ist für beide Heizerkonfigurationen ähnlich. Diese Daten implizieren, dass ein bisher hauptsächlich bei Behältersieden beobachteter Dry-Spot-Mechanismus auch für Strömungssieden plausibel ist. Eine phänomenologische Erweiterung dieses Mechanismus für Strömungssieden wird vorgestellt. Es wurde außerdem ein Stabilitätskriterium für den Siedeprozess identifiziert: Der Siedeprozess wird instabil, sobald die thermische Diffusionszeit des Heizermaterials deutlich größer als die Interaktionszeit von Dampfstrukturen mit der Heizeroberfläche wird.

Abstract

Nucleate boiling heat transfer is limited by the occurrence of critical heat flux (CHF). The associated rapid increase in surface temperate can lead to the destruction of the heat-dissipating device with possibly catastrophic consequences. The accurate prediction of critical heat flux therefore remains one of the most important challenges in two-phase heat transfer research. In this study, local measurements along the boiling curve of surface heat flux, surface temperature and void data from fiber-optic microprobes are presented for vertical subcooled flow boiling of refrigerant Novec 649 in a square flow channel. Two heaters of technically relevant thickness made of two different materials but with identical surface characteristics were investigated: a wall-mounted copper heater and a single-rod copper-coated stainless steel heater. Boiling curves for both heater configurations are provided alongside data on void fraction, void frequency and void ligament length obtained from fiber-optic microprobes placed in the immediate vicinity of the heater surface. With the experimental data, the prediction accuracy of three established mechanistic models for the prediction of critical heat flux in flow boiling was assessed. All investigated models failed to accurately reproduce the experimental data. In contrast, the experimental data of this study agrees well with some of the core assumptions of two more recent mechanistic critical heat flux models. To contribute to the understanding of the fundamental processes leading to critical heat flux, a comparison of the void morphology along the boiling curve between the two heater configurations is presented. The data is discussed with respect to recent advancements in identifying the governing parameters for boiling heat transfer in pool boiling. It was found that the entire boiling curve correlates well with the triple-phase contact line density on the heater surface. Recurrent patterns in the morphology of the void phase in close proximity of the boiling surface were observed at critical heat flux. Based on the data, a dry-spot CHF mechanism appears viable. A phenomenological extension of the dry-spot mechanism for pool boiling to flow boiling is presented. Additionally, a common stability limit for the boiling process for the two heater configurations was identified based on the fiber-optic microprobe data. It was found that the boiling process becomes unstable when the thermal diffusivity time of the heater substrate becomes much longer than the void interaction time at the heater surface.

Contents

List of Figures

List of Tables

Nomenclature

Abbreviations

BOH Breakdown of heat transfer

CFD Computational fluid dynamics

CHF Critical heat flux

DNB Departure from nucleate boiling

FDB Fully-developed boiling

FDFB Fully-developed film boiling

HTC Heat transfer coefficient

ONB Onset of nucleate boiling

PIF Phase indicator function

PIV Particle image velocimetry

RH Single rod copper-coated stainless steel heater

TC Thermocouple

TCR Thermocouple row

WH Wall-mounted copper heater

WMS Wire-mesh sensors

Dimensionless numbers

Ja Jakob number —

NA Numerical aperture —

Nu Nusselt number —

Nu_∞ Nusselt number for a fully developed flow —

Pr Prandtl number —

Re	Reynolds number	—

Greek letters

α	Void fraction	—
Δ	Denotes a difference	—
Δh_{evap}	Specific enthalpy of evaporation	$\mathrm{kJ\,kg^{-1}}$
δ_{g}	Average thickness of the vapor layer above the heater surface	m
δ_{l}	Thickness of liquid layer/sublayer	m
ϵ	Friction factor	—
λ	Thermal conductivity	$\mathrm{W\,m^{-1}\,K^{-1}}$
λ_{c}	Critical wavelength of the Kelvin-Helmholtz instability	m
ν	Kinematic viscosity	$\mathrm{m^2\,s^{-1}}$
Ψ	Function to correct influence of turbulence	—
ρ	Density	$\mathrm{kg\,m^{-3}}$
$\overline{\rho}$	Average density across the flow channel	$\mathrm{kg\,m^{-3}}$
σ	Surface tension	$\mathrm{mN\,m^{-1}}$
$\sigma_{(\ldots)}$	Standard deviation	—
τ	Period of wetting front	s
θ	Contact angle	rad
φ	Angle	$^{\circ}$

Roman letters

a	Thermal diffusivity	$\mathrm{m^2\,s^{-1}}$
b	Ratio of the length of a wetting front to the total wavelength	—
C_1	Constant	$\mathrm{s\,m^{-1}}$
C_2	Constant	$\mathrm{J\,m^{-2}\,K^{-1}}$

C_D	Drag coefficient	—
c	Specific heat capacity	$J\,kg^{-1}\,K^{-1}$
c_r	Real component of wetting front wave speed	$m\,s^{-1}$
d	Diameter	m
$\dot{E}$	Rate of change of thermal energy	W
F	Lift force	N
f	Frequency	Hz
G	Mass flux	$kg\,m^{-2}\,s^{-1}$
G'	Mass flux from core to bubbly layer	$kg\,m^{-2}\,s^{-1}$
g	Gravitational acceleration	$m\,s^{-2}$
h	Heat transfer coefficient	$W\,m^{-2}\,K^{-1}$
h	Specific enthalpy	$J\,kg^{-1}$
i	Index variable	—
i_b	Turbulence intensity between the bubbly layer and the bulk flow	—
j	Index variable	—
k	Index variable	—
k	Wave number	m^{-1}
L_i	Triple-phase contact line density	$m\,m^{-2}$
l	Length	m
N	Quantity	—
N''	Nucleation site density	m^{-2}
n	Number of samples	—
n	Refractive index	—
P	Probability	—

p	Pressure	$\mathrm{N\,m^{-2}}$
Q	Heat	J
$\dot{Q}$	Heat flow	W
$\dot{q}$	Surface heat flux	$\mathrm{W\,m^{-2}}$
R	Correlation coefficient	—
r	Radius	m
sr	Sample rate	Hz
T	Temperature	K
t	Time	s
t_a	Cavity activation time	s
t_c	Bubble condensation time	s
t_g	Bubble growth time	s
t_r	Recovery time of the thermal boundary layer	s
t_w	Bubble waiting time	s
U	Voltage	V
u	Velocity	$\mathrm{m\,s^{-1}}$
u'	Radial fluctuating velocity	$\mathrm{m\,s^{-1}}$
u_y	Radial velocity created by vapor generation	$\mathrm{m\,s^{-1}}$
x_1	Quality in the core flow	—
x_2	Quality in the bubbly layer	—
y	Distance in wall normal direction	m
z	Distance in flow direction	m
z^*	Distance of upstream wetting front to leading edge of heater	m

Subscripts

conv   Convection

crit   Conditions at critical point

cu   Copper

diff   Thermal diffusivity

eff   Effective

evap   Refers to evaporation

g   Gas phase

hyd   Hydraulic

l   Liquid phase

lig   Void ligament

p   Isobaric

probe   Refers to a characteristic of a fiber-optic microprobe

sat   Refers to saturation conditions

sub   Subcooling

sup   Refers to the superheat of the boiling surface

th   Threshold

tip   Fiber probe tip

w   Refers to the boiling surface

Chapter 1

Introduction

1.1 Background

A growing technological need for the dissipation of high heat fluxes over small surfaces has led to a recent increase in two-phase flow heat transfer research. For many applications such as power electronics, micro-processors, medical X-ray equipment, heat exchangers for hydrogen storage in automobiles or particle accelerators, single-phase cooling systems often fail to meet the cooling requirements [11]. There is a gradual switch to phase change cooling in many industries.

The performance of two-phase cooling systems is limited by the occurrence of critical heat flux (CHF) and the associated transition from nucleate boiling to film boiling. This causes the rapid deterioration of the overall heat transfer coefficient. The subsequent steep increase in heater temperature may in many circumstances lead to system failure. Predicting this design limit remains one of the most important challenges in two-phase heat transfer research.

The most widely used tools to predict CHF are semi-empirical or empirical correlations. A key drawback to using these correlations is their general limitation to a small set of fluids and operating conditions. The user might be compelled to apply a correlation to other fluids and conditions outside of its validity range, which usually leads to erroneous results. To circumvent this shortcoming, so-called universal CHF correlations were derived from comprehensive experimental data bases. However, using theoretical models based on experimental observations to predict CHF is favorable [12]. Numerous mechanistic models have been developed over the years. They are based on a variety of underlying physical pictures regarding the morphology of the two-phase mixture near the heated wall at CHF. Three of the most widely rec-

ognized mechanistic models for the prediction of CHF in flow boiling are the bubble crowding model [13], the sublayer dry-out model [14], and the interfacial lift-off model [15]. Several studies have assessed the validity of their assumptions regarding the underlying physical processes leading to CHF [9, 10, 16, 17]. In contrast, validation studies assessing the models' quantitative prediction accuracy for CHF data other than the data used to developed the models are scarce. Most mechanistic models perform well on the data sets with which they were developed. However, many mechanistic models make use of empirical constants or employ empirical submodels [12]. Hence, these models are likely bound by the same limitations as purely empirical correlations when subjected to data from other experiments with different conditions.

With the advancement of computational fluid dynamics (CFD), new models [18, 19] and new computational techniques for the simulation of two-phase systems are constantly emerging. However, current simulation tools still largely incorporate empirical models, too [11]. Even though advancements and new ideas are continuously published, there is a delay between the development of new and improved modeling approaches and their implementation in available numerical tools. There is only a small number of comprehensive validation test cases against which CFD approaches can be benchmarked, for example [20–22]. Many of these validation test cases are water-based. Consequently, there is a need for comprehensive quantitative experimental data for fluids other than water for the validation of new models and numerical techniques.

In general, the modeling of boiling phenomena and CHF should be improved by

- focusing on modeling parameters based on quantitative experimental data [23] and by

- further clarifying the understanding of the fundamental processes leading to the termination of nucleate boiling at CHF [24].

For pool boiling, the experimental progress in recent years has led to a much better understanding of the boiling process and the mechanisms leading to CHF. In the nucleate boiling regime, heat transfer is governed by convection, microlayer evaporation and transient single-phase conduction in the immediate vicinity of the triple-phase contact line [25]. Many studies found the ex-

istence of unquenchable dry-spots on the heater surface at high heat fluxes and linked this with the occurrence of CHF [25–29]. Despite the solid quantitative experimental foundation, the general description of the dry-spot CHF process to date lacks a clear explanation of why dry-spots begin to form on the heater surface [30]. Moreover, only few studies have found direct evidence for the formation of dry-spots on the boiling surface for flow boiling so far [31, 32]. Very thin heaters were used in many of the recent studies on the fundamentals of the boiling crisis in pool and flow boiling. This precludes the thermal properties of the heater substrate, which heavily influence the boiling process at high heat flux [30, 33, 34]. Therefore, there is a persisting need for quantitative fundamental experiments in subcooled flow boiling on heaters with technically relevant thickness to

- substantiate the notion that the dry-spot CHF mechanism is universal for pool and flow boiling on both thin and thick heaters and

- to identify the governing parameters, which cause the stability limit of the boiling process at CHF.

1.2   Scope and Value of this Dissertation

The scope of this dissertation is to contribute to the understanding of the fundamental heat transfer processes at the wall during subcooled flow boiling along the boiling curve and especially at CHF. This is done by providing locally coupled, synchronous measurements of temperature, heat flux and quantitative data of the void phase from fiber-optic microprobes along the boiling curve for subcooled flow boiling of refrigerant Novec 649. Two heaters made of different materials but with the same surface characteristics are investigated: a wall-mounted copper heater and a single-rod copper-coated stainless steel heater. This allows to study the influence of the heater material on the heat transfer processes independently of surface effects like nucleation site density or wetting characteristics.

This dissertation provides comprehensive local data of heat flux and surface temperature along the boiling curve as well as void data profiles above the heater surface for both heater configurations at different operating condi-

tions. Additionally, quantitative experimental data about the morphology of the void phase in the immediate vicinity of the heated wall along the boiling curve and during the CHF transient is presented. With the experimental data, the predictive capabilities and the plausibility of underlying assumptions of different modeling approaches can be assessed. To date, there is no detailed experimental data in literature on the behavior of the void phase very close to the boiling surface along the boiling curve for subcooled flow boiling on heaters with technically relevant thickness. This dissertation therefore

- complements the available, mostly water-based validation test cases for current and future models and numerical tools with comprehensive experimental data for a fluid different than water,

- contributes to the understanding of the fundamental heat transfer mechanisms along the boiling curve and

- contributes to the identification of the parameters leading to the breakdown of heat transfer at CHF and their evolution along the boiling curve.

1.3   Research Aims and Objectives

The dissertation has three research aims:

1. Assess whether established and more recently published mechanistic models for the prediction of CHF in flow boiling possess universal predictive capabilities using the experimental data of this study with the following objectives:

   - Test the performance of established and more recently published mechanistic models with the CHF data of this dissertation.

   - Assess the validity of the underlying assumptions regarding the flow morphology with the experimental data.

2. Identify the governing parameters for boiling heat transfer along the boiling curve up to CHF with the following objectives:

   - Investigate how the morphology of the two-phase mixture in the immediate vicinity of the heated wall evolves along the boiling curve.

- Determine whether there are shared characteristics for the two heater configurations.

3. Investigate the trigger mechanism for the occurrence of CHF with the following objectives:

   - Examine whether there are fundamental changes in flow morphology close to the wall at CHF.

   - Identify recurrent patterns for the two heater configurations.

   - Assess whether a dry-spot CHF mechanism is viable for flow boiling on heaters with technically relevant thickness.

   - Identify a criterion for which nucleate boiling becomes unstable and CHF is triggered.

1.4   Dissertation Outline

Following this introduction, Chapter 2 provides the fundamentals relevant to this dissertation. Chapter 3 describes the experimental setup, the measurement techniques used, the post-processing of measurement data and the measurement procedure. In Chapter 4, the experimental results are introduced and discussed. First, experimental data is presented for both heater configurations. Secondly, the data is analyzed and discussed in relation to the research aims and objectives. The analysis is split into two parts: In the first part, current mechanistic models are discussed with respect to the experimental data. In the second part, the data from both heater configurations is compared with each other and analyzed in more detail regarding the governing parameters of boiling heat transfer along the boiling curve and the trigger mechanism at CHF. The dissertation is concluded by Chapter 5, where the key findings are summarized and a conclusion is drawn.

Chapter 2

Fundamentals

This chapter contains the fundamentals relevant to this dissertation. First, an overview of the modes of boiling, the boiling curve and critical heat flux is given. Second, the parametric trends of critical heat flux are highlighted. Third, the modeling of boiling phenomena is summarized focusing on the prediction of critical heat flux in flow boiling. Here, prevalent mechanistic models are summarized followed by the identification of recent experimental advancements in fundamental boiling research. This research resulted in the development of so-called next-generation critical heat flux models for the application in multi-phase CFD-codes. Subsequently, two of these next-generation models are introduced. As experimental validation is an essential part of model development, this chapter concludes with a short overview about available measurement techniques for experiments in two-phase flow.

2.1   Modes of Boiling

Boiling can occur under several conditions. Two main modes of boiling have to be distinguished: pool boiling, where the fluid is static and any motion near the boiling surface is due to either free convection or bubble-induced stirring, and flow boiling, where the fluid is subjected to forced convection. In either mode, boiling may occur under subcooled or saturated conditions. In subcooled boiling, the average liquid temperature is below the saturation temperature and therefore vapor bubbles may recondense after their formation. In saturated boiling, the liquid temperature is at the saturation temperature or even slightly exceeds the saturation temperature. Therefore, bubbles formed at the boiling surface cannot be condensed by surrounding liquid. Subcooled flow boiling is used in many technical applications, as it provides

the highest heat transfer rates. In the present study, subcooled flow boiling was investigated.

2.2 Boiling Curve and Critical Heat Flux

For both pool and flow boiling, the same qualitative boiling curve as first introduced by Nukiyama [35] can be observed. Fig. 2.1 shows surface heat flux $\dot{q}$ plotted versus the wall superheat $\Delta T_{sup} = T_w - T_{sat}$. The boiling curve can be divided into different sections [36].
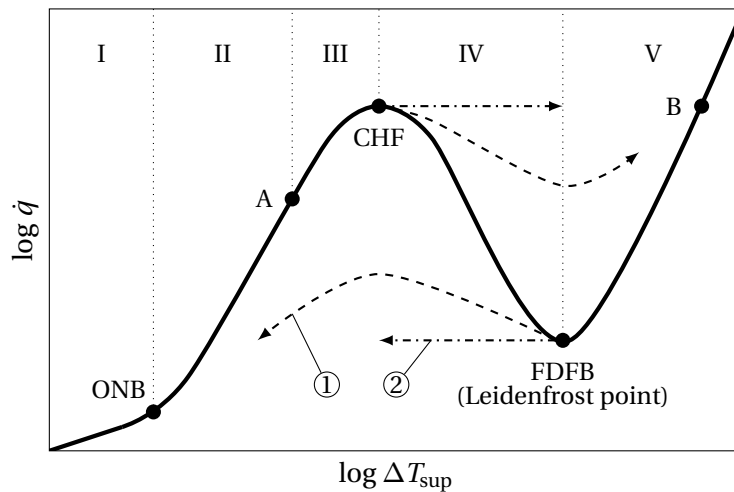
Figure 2.1: Characteristic boiling curve for pool and flow boiling, adapted from [37].

Section I - Single-phase convection: Below the onset of nucleate boiling (ONB), heat is transferred from the heated surface to the fluid by single-phase convection. As wall superheat ΔT_{sup} increases, bubble formation will eventually occur. Due to boiling retardation, the wall superheat at ONB must slightly exceed the saturation temperature to trigger bubble formation.

Section II - Isolated bubble regime: At ONB, bubbles begin to form at active nucleation sites on the surface. The periodic growth and detachment of individual bubbles from the surface induce considerable fluid mixing near the surface. In conjunction with the latent heat of phase change, this significantly increases the heat transfer coefficient h. As wall superheat increases,

8

the boiling surface becomes more densely populated with individual bubbles forming at active nucleation sites.

Section III - Fully-developed nucleate boiling: As ΔT_{sup} further increases, more and more nucleation sites become active and increased bubble formation causes interference and bubble coalescence. At point »A« in Fig. 2.1, individual bubbles merge to form vapor slugs or so-called void ligaments. As vapor structures during fully-developed nucleate boiling cannot be regarded as spherical bubbles, the term void ligament is used from here on to refer to void structures in close proximity to the heater surface. In the fully-developed nucleate boiling regime an inflection point exists, at which the effective heat transfer coefficient reaches a maximum before continuously decreasing towards CHF. Stable nucleate boiling is limited by a maximum attainable surface heat flux $\dot{q}_{CHF}$ at CHF. This point is often termed the boiling crisis or the departure from nucleate boiling (DNB), too.

Section IV - Transition boiling: Section IV is termed transition boiling or partial film boiling. Increasing the heat flux beyond $\dot{q}_{CHF}$ leads to a rapid increase in heater temperature. This temperature excursion can lead to system failure and must usually be avoided in technical systems. Nucleate boiling breaks down as the surface temperature increases and a vapor film is formed on the heater surface. At any point, the conditions during transition boiling may oscillate between nucleate boiling and film boiling.

Section V - Film boiling: At the Leidenfrost point, termed fully-developed film boiling (FDFB), the surface is completely covered by a vapor film. Heat transfer is dominated by conduction and radiation through the vapor phase. In a temperature-controlled system, the system follows the boiling curve from CHF to point »B« in the fully-developed film boiling regime as depicted in Fig. 2.1. For a power-controlled system, the transient behavior during transition boiling depends on its thermal inertia [37]. This is schematically depicted for two systems with different thermal inertia by lines »1« and »2«.

2.3 Parametric Trends of Critical Heat Flux

The magnitude of CHF is heavily governed by the system's operating parameters. These can be classified into: thermal-hydraulic, geometric and external parameters. Main thermal-hydraulic parameters of interest are system pressure, mass flux and local subcooling. For geometric parameters, channel diameter, surface roughness and heater thickness and for external parameters, heat flux distribution and dissolved gases are generally regarded as important for subcooled flow boiling [12, 38]. Due to the assumption of uniformly heated surfaces and the absence of gas solubility in most mechanistic models for subcooled flow boiling, external parameters are excluded in this overview for brevity.

2.3.1 Thermal-Hydraulic Parameters

2.3.1.1 System Pressure

In a tubular test section operating at a pressure range of 0.1 MPa - 5.0 MPa, Celata et al. [39] reported a negligible influence of pressure on CHF for equal subcooling and liquid velocity. Celata and Mariani [12] stated that similar behavior has been observed in most other experimental studies (e.g. [40]). In contrast, for tubes of similar dimensions at significantly higher pressures of up to 21 MPa, Cheng and Xia [41] observed a slight decrease of the critical heat flux with increasing pressure. Despite this discrepancy, the change of CHF with variable pressure can be considered less distinct compared to the impact of other parameters [16].

2.3.1.2 Mass Flux

With increasing mass flux, CHF increases linearly for a wide range of mass fluxes [42]. This has been shown by many experimental studies for tubular [43–45] and rectangular [46–48] test sections. In their experimental study, Bloch et al. [47] observed a varying dependency of CHF on mass flux, depending on the turbulence intensity present in the flow channel. Dependency of

CHF on mass flux increased with increased turbulence, showing the steepest increase while using an orifice to induce high turbulence.

2.3.1.3 Subcooling

Many experimental studies show an almost linear relationship between liquid subcooling and CHF [12, 40, 47, 48]. Bloch et al. [47], although their experiments confirmed common literature for channel flows without inserts, observed a deviation from a linear relationship between CHF and subcooling for high-turbulence flows induced by orifices.

2.3.2 Geometric Parameters

2.3.2.1 Channel Diameter

CHF and channel diameter have been reported to be inversely related by many authors [12, 38, 42, 49]. For given thermal-hydraulic conditions, CHF increases with a decrease in flow channel diameter. This effect is less significant at small mass fluxes and diameters above 5 mm. A threshold can be observed, above which the effect of an increased tube diameter in relation to the channel length has no observable influence on the magnitude of CHF anymore. This threshold ratio of the length l to the diameter d of the respective tube was found to be around $l/d > 30$ [50].

2.3.2.2 Surface Modifications

According to Liang and Mudawar [51], surface modifications can be grouped into three main categories: (i) macro-scale modifications with features larger than 1 mm, (ii) micro-scale modifications in the range of 1 μm - 1000 μm and (iii) nano-scale modifications with features smaller than 1 μm. Enhancement methods from any of these categories can be combined to create hybrid-scale enhancement [51]. A short overview about surface modifications at these three scales and their influence on nucleate boiling as well as their CHF amelioration is given in the following.

Macro-scale enhancements: Typical macro-scale surface modifications include finned surfaces, porous meshes or foam attachments to the boiling surface. In the case of finned surfaces, these fins are usually spaced similar to the bubble departure diameter of the fluid used [52]. Yu and Lu [53] showed that more closely spaced and taller fins provide superior nucleate boiling performance and higher critical heat flux for highly wetting fluids. Modifying the boiling surface at the macro-scale can lead to CHF augmentation of up to 400 % [54]. With the rapid development of micro- and nano-fabricated surfaces, research on macro-scale enhancement has declined, despite its superior aging behavior [51].

Micro-scale enhancements: There are a variety of micro-scale surface modification such as surface roughening, micro-fin surfaces, micro-porous coatings and submerged tunnels with reentry cavities. Kandlikar [55] demonstrated an eight-fold heat transfer enhancement in the nucleate boiling regime and an augmentation of CHF by 250 % using a micro-finned surface. Surface roughness can have a profound effect on nucleate boiling [51]. In general, higher surface roughness leads to an increase of CHF in subcooled flow boiling in comparison to a smooth surface. However, there exists a threshold roughness for which the influence on CHF is negligible [12]. This is in accordance to Kandlikar [42], who assessed experimental studies investigating the effect of surface roughness on CHF. CHF augmentation of up to 100 % was possible with a threefold increase in roughness compared to a smooth surface. However, a complementary study by Kandlikar and Spiesman [56] showed that altering an already rough surface will not change nucleation site characteristics and therefore will not affect CHF. This behavior could be confirmed by the author, where using different polishing techniques with different emery papers on a thick copper heater did not alter the heat flux at CHF.

Nano-scale enhancements: Nano-scale surface modifications typically consist of nano-tubes, nano-wires or nano-fibers which are attached to the boiling surface. Other enhancement methods include nano-coating and etched nano-ridges. While these methods generally achieve high heat flux enhancement in the order of several hundred percent compared to a non-

enhanced surface [57], nano-scale enhancements suffer from poor aging characteristics [51].

2.3.2.3 Heater Thickness

Heater thickness and the associated thermal capacitance of a heater does not show a consistent trend regarding the magnitude of CHF. Celata et al. [58] conducted experiments with round tubes of equal inner diameter with different wall thicknesses between 0.25 mm and 1.75 mm and found a slight decrease of CHF as wall thickness increased. In contrast, in their experiment with similar geometric dimensions Fiori and Bergles [59] observed an increasing CHF with increasing wall thicknesses. Considering the temperature fluctuation at the boiling surface as reported for boiling experiments by for example Fiori and Bergles [59] or Katto [60], it is without question that a different thermal capacitance influences CHF. However, as reported by Konishi et al. [61], CHF variation with heater thickness is negligible for more voluminous heaters with larger thermal inertia.

2.4   Modeling of Boiling Phenomena

There is a recent rise in the rate of heat dissipation in many technical applications. The concurrent trend to decrease the size of cooling hardware often-times renders single-phase cooling systems incapable to meet the cooling requirements. There is a gradual application of two-phase cooling systems across many industries [11]. Two-phase cooling is limited by the occurrence of CHF. Due to its high technical importance, extensive theoretical and experimental research has been conducted on the critical heat flux phenomenon. This has spawned many different approaches to predict CHF. These approaches range from empirical correlations to mechanistic models based on physical mechanisms and models for application in CFD codes. Extensive reviews on this topic have been published by for example Kharangate and Mudawar [11], Konishi et al. [61], Kandlikar [42] and Celata and Mariani [12].

In the following sections, a short overview about the empirical and mechanistic modeling of the CHF phenomenon is given followed by a summary of recent experimental advancements. These advancements lead to the development of next-generation mechanistic models for CFD applications for the prediction of boiling phenomena along the boiling curve and beyond CHF. Concluding this section, two particularly promising modeling approaches are therefore introduced.

2.4.1 Empirical Critical Heat Flux Models

The most prevalent approach to predict boiling two-phase flow to-date is the use of empirical or semi-empirical correlations. Empirical modeling relies greatly on the availability of data for both the development of a correlation as well as the assessment of its applicability. This limits the predictive capabilities of most correlations to one or a few fluids and to a narrow range of operating parameters and geometrical configurations. This can lead to erroneous results as often-times the user of these correlations is compelled to use them beyond their range of validity [11]. To circumvent this shortcoming, more universal correlations were derived based on large databases consisting of different fluids and covering a wide range of operating and geometrical parameters. For flow boiling, there are many collections of correlations available for the prediction of CHF in subcooled flow boiling [62–65] and saturated flow boiling [66–71]. In their review, Celata and Mariani [12] identified the most widely used and most applicable empirical correlations for subcooled flow boiling [63–65] and for saturated flow boiling [69–71]. However, they too stress the correlations' high inaccuracies outside the range of their underlying data. Tong and Tang [38] assessed the use of correlations for predicting the departure from nucleate boiling for flow boiling in nuclear reactors. The authors state that when using empirical correlations to determine operating conditions and safety margins of nuclear reactors, highly conservative operating conditions are usually chosen to guarantee the safe operation of the reactor core under all circumstances. Minimizing this conservatism constitutes great economic potential, for example in terms of monetizing more flexible operation or increased productivity. The same is true for other applications of flow boiling as a heat removal mechanism. In principle, this can be achieved by mechanistic modeling.

2.4.2 Mechanistic Critical Heat Flux Models

Mechanistic modeling is based on either physical mechanisms, which were observed in experiments, or analytically derived physical relations. Numerous models for the prediction of CHF in pool and flow boiling have been proposed and developed over the years.

2.4.2.1 Overview

Existing mechanistic models for the prediction of CHF in flow boiling are generally based on six different mechanisms. Celata and Mariani [12] and Kandlikar [42] grouped the major theoretical CHF modeling approaches into five model categories according to their main CHF trigger mechanisms. Additionally, Galloway and Mudawar [15] postulated another CHF trigger mechanism in their model, which was not covered in [12] and [42]. Although the details of each mechanism may differ for each model depending on the authors, the basic concept is usually retained. These prevalent six mechanisms are briefly summarized in the following.

1. Liquid layer superheat limit model:
   A bubbly layer is assumed to obstruct the heater. This limits heat transport away from the heater and causes a critical superheat in the liquid layer in the immediate vicinity of the heater, which subsequently induces CHF.

2. Boundary layer separation model:
   An injection of vapor due to the evaporation of liquid on the heated surface is assumed to cause a deceleration of the flow close the heater. CHF is postulated to occur abruptly when vapor effusion increases beyond a critical value and induces a stagnation of the bulk flow close to the heater.

3. Liquid flow blockage model:
   CHF is assumed to occur when liquid flow normal to the heater is obstructed by the outward vapor flow at a critical velocity due to instabilities in the vapor-liquid layer or the equilibrium between the kinetic energies of the two phases.

4. Vapor removal limit and near-wall bubble crowding model:
   Turbulent interchange between the bulk flow and a bubbly layer close to the heated surface is assumed to be limited. As a result, the crowding of bubbles in the region close to the heated wall prevents the replenishment with fresh bulk liquid and causes CHF after reaching a critical void fraction. A simplified illustration of the general mechanism is shown in Fig. 2.2a.

5. Liquid sublayer dry-out model:
   Vapor stems originate from the evaporation of liquid at the heater. Their columnar structure collapses due to a Helmholtz instability and forms a vapor blanket covering a thin liquid film underneath. CHF is assumed to occur when the rate of evaporation exceeds the rate by which bulk liquid is fed to the heater. A simplified illustration of the general mechanism is shown in Fig. 2.2b.

6. Interfacial lift-off model:
   A continuous wavy vapor layer covers the heater. Due to interfacial instability, wetting fronts occur and periodically touch the heated surface, providing the heater with fresh liquid. CHF is assumed to occur when vapor efflux normal to the heater is big enough to push away the first upstream wetting front from the heater. The subsequent temperature increase of the heater precludes all future wetting fronts. A simplified illustration of the general mechanism is shown in Fig. 2.2c.

The latter three of the models have received considerable attention. Kandlikar [42] and Celata and Mariani [12] both provided some examples of the inadequacies of the other models. In case of the liquid layer superheat limit model [59], the absence of a clear explanation of the CHF phenomenon was noted [42], despite the observation of periodically increasing wall temperature in [72] on which the model was based. The boundary layer separation model was criticized for its assumption of an abrupt change in the macroscopic structure of the flow close to CHF and its weak physical basis [73, 74]. Experimental studies [75–77] suggest a non-abrupt change in macroscopic flow conditions during the transition from nucleate to film boiling. While the underlying mechanism of the liquid flow blockage model possesses potential feasibility for pool boiling, Kandlikar [42] attested this model inadequate evidence supporting its applicability to flow boiling.
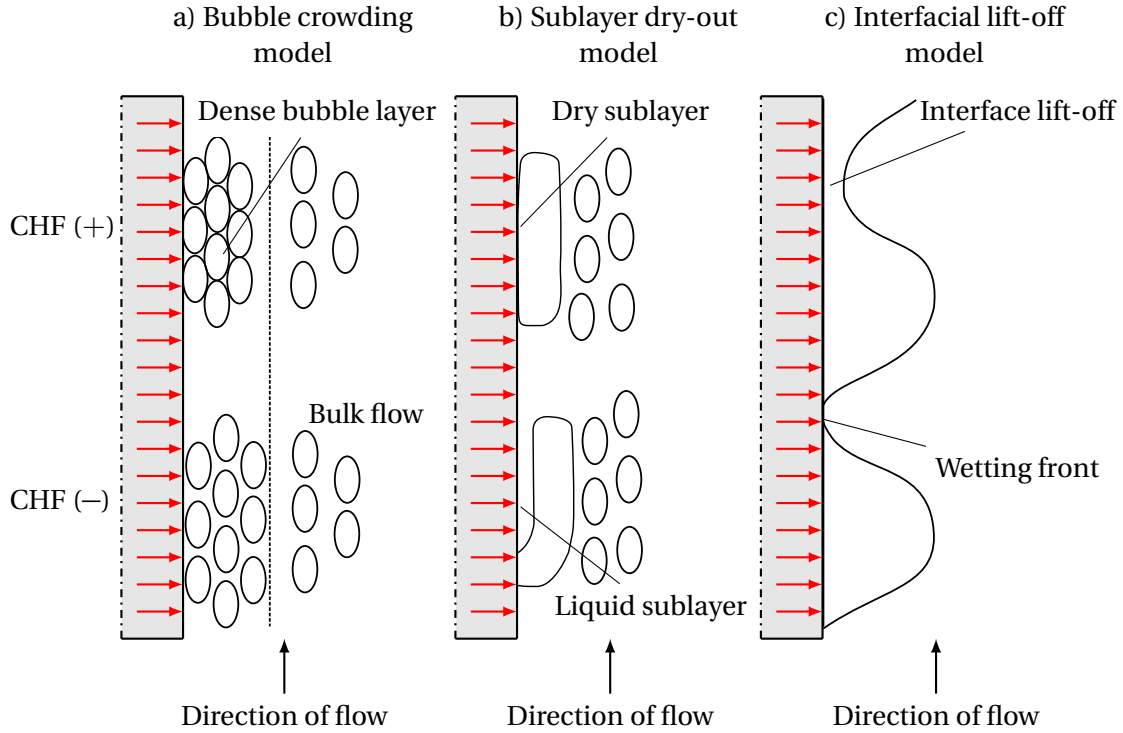
Figure 2.2: Schematic representation of the DNB trigger mechanisms for three mechanistic CHF models, adapted from [61].

In the following, the main mechanisms of the three favored mechanistic models are examined in more detail. In addition, their mathematical formulation is succinctly summarized by citing main equations to provide an overview of the underlying physical concepts.

2.4.2.2 Bubble Crowding Model

Main mechanism: Models based on the bubble crowding mechanism generally assume that an accumulation of bubbles near the wall inhibits the transport of fresh liquid to the heater surface. At CHF, the bubble layer is assumed to be at its maximum thickness [13]. CHF is postulated to occur when the void fraction in the bubbly layer just exceeds a critical void fraction. This critical void fraction was derived by Weisman and Pei [13] to be $\alpha_{\mathrm{CHF}} = 82\,\%$. This value stems from the void fraction of an array of ellipsoidal bubbles, which can be maintained in the bubbly layer without significant contact between individual bubbles. The general flow morphology close to

critical heat flux and the structure of the bubble layer above the heater surface are schematically illustrated in Fig. 2.3.
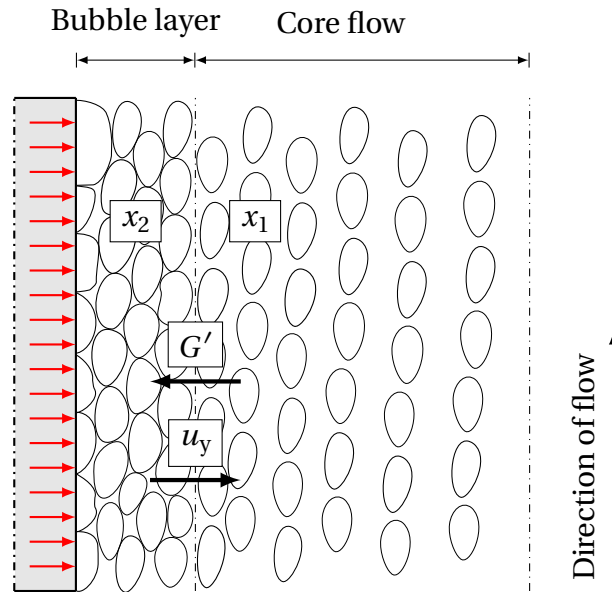
Figure 2.3: Flow morphology and the structure of the bubble layer above the heater surface at CHF according to the bubble crowding model.

The mechanism of bubble crowding in the vicinity of a heated surface was first introduced by Hebel et al. [78], who proposed an incipient hydrodynamic model for the departure from nucleate boiling in water under forced convection based on experimental observations. The first model for subcooled flow boiling based on the bubble crowding mechanism was introduced by Weisman and Pei [13]. The model has received considerable attention over the years [79–86]. The original model [13] was successively extended to other operating conditions. Weisman and Ying [79] applied the theoretical background of the bubble crowding model to heat flux prediction for rod bundles at pressurized water reactor conditions. In a later study, Ying and Weisman [80] introduced an evolution of the model allowing for a non-uniform void profile. Weisman and Illeslamlou [81] extended the original model [13] to higher subcooling. Lim and Weisman [82] considered the application to annuli with one unheated wall. Weisman et al. [83] introduced a model for boiling heat transfer and critical heat flux prediction for tubes containing twisted tapes. Yang and Weisman [84] developed a phenomenological extension of the bubble crowding model to the boiling process in the detached bubble region in subcooled flow. Chang and Lee [85] extended the model for the prediction of CHF at low qualities for uniformly heated tubes. Kwon [86] proposed

an analytical model, which shared some of the features of the initial bubble crowding model but included significant modifications of the underlying physical concept. The bubbly layer of the original bubble crowding model [13], which is postulated to be several bubble diameters thick, was replaced in this work by the concept of single, wall-attached bubbles, which act as a surface roughness equivalent and therefore affect the local flow conditions. The authors utilized the work of Chang and Lee [85] as a starting point for their work and based their postulated flow structure on experimental work by Gunther [65] and Kirby and Westwater [75], who observed that the two-phase layer at the wall of a heated tube is in the order of magnitude of one bubble diameter. Even though the model still employs the idea of a critical void fraction in the bubble wall layer, Kwon [86] assumes that a compact single layer of bubbles at the heater poses the physical barrier to the liquid supply from the core and thus inhibits the heat transfer process at CHF.

Mathematical formulation: The formulation of the bubble crowding model according to Weisman and Pei [13] is succinctly summarized in the following.

CHF is calculated according to Eq. (2.1).

$$\dot{q}_{\mathrm{CHF}} = \Delta h_{\mathrm{evap}} G'(x_2 - x_1) \frac{h_{\mathrm{l,sat}} - h_{\mathrm{ld}}}{h_{\mathrm{g}} - h_{\mathrm{ld}}} \tag{2.1}$$

CHF is dependent on the lateral mass flux G' due to turbulent interchange at the edge between the bubbly layer near the wall and the core flow, the qualities in the core flow x_1 and in the bubbly layer x_2 at the critical void fraction of $\alpha_{\mathrm{crit}} = 82\,\%$ and the specific enthalpy at bubble detachment h_{ld} from Levy [87].

The lateral mass flux between the bubbly layer and the core flow is calculated based on the axial mass flux G according to Eq. (2.2).

$$G' = i_{\mathrm{b}} \Psi G \tag{2.2}$$

In this equation, i_{b} denotes the turbulence intensity at the boundary between the bubbly layer and the bulk flow. This quantity is calculated as

$$i_{\text{b}} = 0.790 \text{Re}^{-0.1} \left(\frac{d_{\text{lig}}}{d_{\text{hyd}}} \right)^{0.6} \left(1 + \text{C} \frac{\rho_{\text{l}} - \rho_{\text{g}}}{\rho_{\text{g}}} \right) \tag{2.3}$$

In this equation Re is the Reynolds number, ρ_{l} and ρ_{g} are the liquid and vapor densities, d_{lig} is the bubble diameter, d_{hyd} the hydraulic diameter of the flow channel and C is a constant with a value of C $=$ 0.135 for $G \leq 9.7 \times 10^6\,\text{kg}\,\text{h}^{-1}\,\text{m}^{-2}$ and C $= 0.135\,(G/9.7 \times 10^6)^{-0.3}$ for $G > 9.7 \times 10^6\,\text{kg}\,\text{h}^{-1}\,\text{m}^{-2}$.

Radial vapor production inhibits turbulent eddies to reach the wall and to replenish the boiling surface with fresh liquid. This influence is accounted for by a function Ψ, which is calculated according to Eq. (2.4).

$$\Psi = \left\{ \frac{1}{\sqrt{2\pi}} \exp \left[-\frac{1}{2} \left(\frac{u_{\text{y}}}{\sigma_{u'}} \right)^2 \right] - \frac{1}{2} \left(\frac{u_{\text{y}}}{\sigma_{u'}} \right) \text{ercfc} \left(\frac{1}{\sqrt{2}} \frac{u_{\text{y}}}{\sigma_{u'}} \right) \right\} \tag{2.4}$$

In this equation, u_{y} is the radial velocity due to vapor generation, which is calculated by Eq. (2.5) using the portion of total surface heat flux effective in generating vapor $\dot{q}_{\text{lig}}$ according to Lahey and Moody [88].

$$u_{\text{y}} = \frac{\dot{q}_{\text{lig}}}{\rho_{\text{g}} \Delta h_{\text{evap}}} \tag{2.5}$$

Further, the standard deviation of the radial fluctuating velocity u' is calculated as

$$\sigma_{u'} = \frac{i_{\text{b}} G}{\overline{\rho}}. \tag{2.6}$$

2.4.2.3 Sublayer Dry-out Model

Main mechanism: Models based on the sublayer dry-out mechanism usually assume that vapor blankets form from small bubbles at high heat flux. These blankets grow as vertically distorted vapor cylinders, whose circumferential growth is confined by neighboring vapor blankets. The equivalent

diameter of the vapor cylinders is assumed to be equal to the departure diameter of individual bubbles at the respective thermal-hydraulic conditions and is expected to stay constant. These void structures obstruct liquid flow to the heater and therefore enclose a thin liquid layer underneath. The liquid layer beneath the vapor blankets is terminated by the stem of the vapor blanket. The length of this blanket is essential to the calculation of the CHF. The blanket length is assumed to be equal to the critical Helmholtz wavelength. CHF is postulated to occur when the rate of sublayer mass loss due to evaporation exceeds the rate of the liquid entering the sublayer from the core region due to a velocity difference between bulk flow and the vapor blankets caused by the buoyancy force [14]. The general flow morphology close to critical heat flux and the structure of the liquid sublayer beneath a vapor blanket are schematically illustrated in Fig. 2.4.
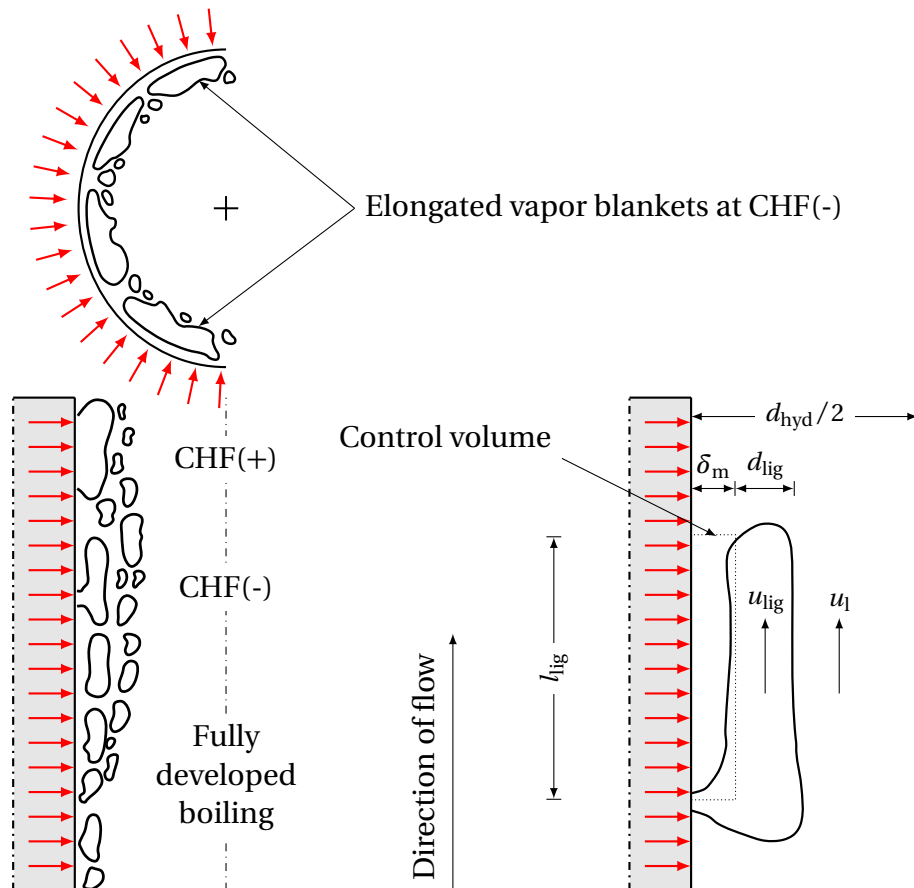
Figure 2.4: Flow morphology just before CHF (CHF(-)) and just after CHF (CHF(+)) (left) and the structure of the liquid sublayer beneath a vapor blanket (right) according to the sublayer dry-out model. Adapted and reprinted from [14].

21

The sublayer dry-out model was first introduced for flow boiling by Lee and Mudawar [14]. It expanded the model of Haramura and Katto [89], who adapted their model for pool boiling to forced convection boiling based on a similar mechanism. The model has received great attention over the past decades [49, 74, 90–92]. The original model [14] as well as early evolutions, e.g. by Katto [90], featured extensive empiricism, especially describing the bubble dynamics in the near-wall region. Celata et al. [74] therefore presented a rationalization of the model without the use of empirical parameters. The formulation of the sublayer dry-out model according to Celata et al. [74] is succinctly summarized in the following.

Mathematical formulation: Critical heat flux is calculated according to Eq. (2.7), which is adopted from Katto [90]. The heat flux necessary to evaporate the liquid sublayer of initial thickness δ_1 during the passage time of a vapor ligament with the velocity u_{lig} and the length l_{lig} can be expressed as

$$\dot{q}_{\text{CHF}} = \rho_1 \Delta h_{\text{evap}} \delta_1 \frac{u_{\text{lig}}}{l_{\text{lig}}}. \tag{2.7}$$

Three submodels are used for the calculation of the length l_{lig} of the vapor ligaments, the velocity u_{lig} of the vapor ligaments and the initial thickness of the liquid sublayer δ_1.

First, the length of the vapor blankets is calculated according to Lee and Mudawar [14] and Katto [90]. The liquid sublayer is generally very thin and can therefore be assumed to rest on the wall. The vapor blanket flows over the liquid sublayer at the velocity u_{lig}. It is postulated that the length l_{lig} of this blanket is equal to the critical wavelength of the Helmholtz instability of the interface between the liquid and the vapor. The length of the vapor blanket l_{lig} is then calculated according to Eq. (2.8).

$$l_{\text{lig}} = \frac{2\pi\sigma\left(\rho_{\text{g}} - \rho_1\right)}{\rho_{\text{g}}\rho_1 u_{\text{lig}}^2} \tag{2.8}$$

Second, the velocity u_{lig} of a vapor blanket is calculated. The velocity of a blanket in vertical turbulent flow is obtained by a force balance [14] considering buoyancy and drag forces according to Eq. 2.9.

$$\frac{\pi d_{\text{lig}}^2}{4} l_{\text{lig}} g (\rho_{\text{l}} - \rho_{\text{g}}) = \frac{1}{2} \rho_{\text{l}} C_{\text{D}} \left(u_{\text{lig}} - u_{\text{l}}|_{y = \delta_{\text{l}} + d_{\text{lig}}/2} \right)^2 \frac{\pi d_{\text{lig}}^2}{4} \tag{2.9}$$

Here, C_{D} is the drag coefficient and $u_{\text{lig}} - u_{\text{l}}|_{y = \delta_{\text{l}} + d_{\text{lig}}/2}$ corresponds to the relative velocity between the vapor blanket and the liquid at the center of the vapor blanket at a wall distance of $y = \delta_{\text{l}} + d_{\text{lig}}/2$. This velocity difference can be rewritten to

$$u_{\text{lig}} - u_{\text{l}}|_{y = \delta_{\text{l}} + d_{\text{lig}}/2} = \left(\frac{2 l_{\text{lig}} g (\rho_{\text{l}} - \rho_{\text{g}})}{\rho_{\text{l}} C_{\text{D}}} \right)^{1/2} . \tag{2.10}$$

The drag coefficient is calculated according to Eq. 2.11, which stems from the work of Ishii and Zuber [93].

$$C_{\text{D}} = \frac{2}{3} \frac{d_{\text{lig}}}{\left(\frac{\sigma}{g(\rho_{\text{l}} - \rho_{\text{g}})} \right)^{1/2}} \tag{2.11}$$

A force balance based on the work of Staub [94] is used to approximate the diameter d_{lig} of the vapor blanket.

$$d_{\text{lig}} = \frac{32}{\epsilon} \frac{\sigma f(\theta) \rho_{\text{l}}}{G^2} \tag{2.12}$$

In this equation, the friction factor ϵ is calculated using the Colebrook-White model in combination with a rough surface model by Levy [87]. The effect of the contact angle on CHF is considered in principle by a function $f(\theta)$. However, a fixed value of $f(\theta) = 0.03$ was chosen in [74]. Concluding the calculation of the blanket velocity, the liquid velocity at the centerline of the vapor blanket $u_{\text{l}}|_{y = \delta_{\text{l}} + d_{\text{lig}}/2}$ is calculated based on a von Karman velocity distribution.

Third, the initial thickness of the liquid sublayer is calculated according to Eq. (2.13). The distance from the wall, where the liquid temperature is equal

to the saturation temperature is obtained using the temperature distribution for turbulent flow in a tube as described in [95].

$$\delta_{\mathrm{l}} = y\big|_{T(y)=T_{\mathrm{sat}}} - d_{\mathrm{lig}} \qquad (2.13)$$

2.4.2.4 Interfacial Lift-off Model

Main mechanism: The interfacial lift-off model, being the most recent one of the three, was first proposed by Galloway and Mudawar [15]. Preceding its introduction, the same authors conducted an extensive photographic study of the flow boiling crisis in a narrow rectangular flow channel with one heated copper wall for refrigerant FC-72 [96]. Flow regimes along the boiling curve were classified into three main categories: First, the discrete bubble regime for heat fluxes slightly above the onset of nucleate boiling. Second, the coalescent bubble regime for heat fluxes above 40 % of CHF, in which discrete bubbles merge downstream to form larger coalesced bubbles. Third, the wavy liquid-vapor layer regime for heat fluxes above 60 % of CHF. At approximately 85 % of CHF, a continuous vapor layer covering the entire heated surface formed. This resulted in the intermittent supply of liquid to the heater through the vapor layer via wetting fronts moving along the heater. Vigorous boiling was observed where the wetting fronts came in contact with the heater surface. At steady state heat fluxes of approximately 95 % of CHF, some parts of the heater were observed to dry out before being replenished by a following wetting front. Galloway and Mudawar [96] noted that interfacial instability acted as a wave generator, locking the first wetting front at a fixed axial position. At CHF, the curvature of the liquid-vapor interface flattened at the point of contact and the wetting front at the leading edge of the heater was lifted away from the surface by the momentum flux of evaporated liquid. The following temperature increase of the heater promoted intense boiling at the remaining wetting fronts and triggered a cascading effect disabling consecutive wetting fronts and precluding any sustained contact of liquid with the heater. The general flow morphology close to critical heat flux and the conceptualization of the lift-off of the wetting front at the leading edge of the heater are schematically illustrated in Fig. 2.5.
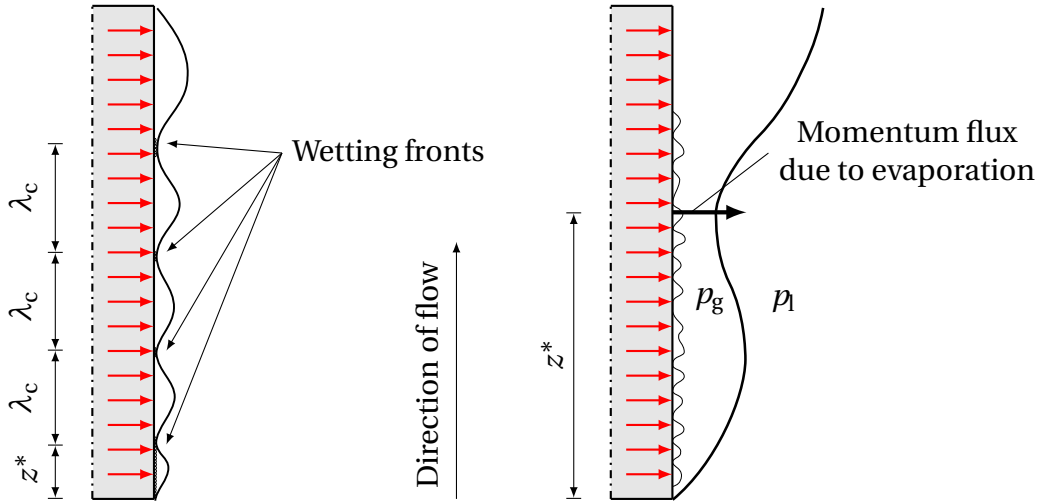
Figure 2.5: Flow morphology at CHF (left) and the conceptualization of the lift-off of the vapor layer above the heater surface (right) according to the interfacial lift-off model.

The model has received considerable attention [97–101]. Gersey and Mudawar [97] expanded the original model to different heater orientation angles. Zhang and Mudawar [98] as well as Konishi et al. [99] introduced a model based on the interfacial lift-off mechanism for application to microgravity flow boiling. Kharangate et al. [100] expanded the model for applications with significant inlet vapor content.

Mathematical formulation: In the following, the formulation of the interfacial lift-off model is succinctly summarized.

The model is divided into three submodels: (i) a surface energy balance to calculate surface heat flux and derive the CHF criterion, (ii) an instability analysis of the liquid-vapor interface to determine wetting front characteristics and (iii) a separated flow model to calculate the velocities of the liquid phase and the vapor phase.

The total surface heat flux $\dot{q}$ is calculated according to Eq. (2.14) as the sum of the surface heat fluxes $\dot{q}_1$ to $\dot{q}_n$ of n discrete wetting fronts propagating along the heater surface at the same time.

$$\dot{q} = \frac{c_{\mathrm{r}}/(2\lambda_{\mathrm{c}})}{l-z*}\left(\int_0^\tau \int_{z*}^l \dot{q}_1 \mathrm{d}z\mathrm{d}t + ... + \int_0^\tau \int_{z*}^l \dot{q}_{n-1}\mathrm{d}z\mathrm{d}t + \int_0^\tau \int_{z*}^l \dot{q}_n \mathrm{d}z\mathrm{d}t \right)$$

(2.14)

In this equation, c_{r} is the real component of the wetting front wave speed, λ_{c} is the critical wavelength of the instability, τ is the wetting front period, z^* is the distance of the upstream wetting front from the leading edge of the heater and l is the length of the heater surface. The number of discrete wetting fronts n on the heater surface is specified by the integer value of Eq. (2.15).

$$n = \left(\frac{l-z^*}{2\lambda_{\mathrm{c}}} + 1 \right)$$

(2.15)

The critical wavelength can be obtained by Eq. (2.16) [99].

$$\lambda_{\mathrm{c}} = \frac{2\pi\sigma\left[(\rho_{\mathrm{l}}\coth(k\delta_{\mathrm{l}}) + \rho_{\mathrm{g}}\coth(k\delta_{\mathrm{g}}) \right]}{\rho_{\mathrm{l}}\coth(k\delta_{\mathrm{l}})\rho_{\mathrm{g}}\coth(k\delta_{\mathrm{g}})(u_{\mathrm{g}} - u_{\mathrm{l}})^2}$$

(2.16)

Determining z^* and λ_{c} requires information about the vapor and liquid velocities as well as the mean thickness of the vapor and liquid layers δ_{g} and δ_{l}. These quantities are determined from a one-dimensional separated flow model.

To initiate critical heat flux by lifting the first wetting front from the heater surface, the momentum of generated vapor has to overcome the pressure difference $p_{\mathrm{l}} - p_{\mathrm{g}}$ across the liquid-vapor interface. It is assumed that wetting fronts make up a fixed fraction b of the total wavelength of the liquid-vapor instability. Assuming a sinusoidal wave shape, the average pressure difference across the interface can then be expressed by Eq. (2.17) [61].

$$p_{\mathrm{l}} - p_{\mathrm{g}} = \frac{4\pi\sigma\delta_{\mathrm{g}}}{\mathrm{b}\lambda_{\mathrm{c}}{}^2}\sin(\mathrm{b}\pi)$$

(2.17)

The lift-off heat flux required to push the interface of the first wetting front away from the heater surface is then calculated based on a force balance according to Eq. (2.18).

$$\dot{q}_{1,\mathrm{CHF}} = \rho_{\mathrm{g}} \Delta h_{\mathrm{evap}} \left(1 + \frac{c_{\mathrm{p,l}} \Delta T_{\mathrm{sub}}}{\Delta h_{\mathrm{evap}}} \right) \left(\frac{p_{\mathrm{l}} - p_{\mathrm{g}}}{\rho_{\mathrm{g}}} \right)^{1/2} \qquad (2.18)$$

2.4.3 Recent Experimental Advancements in Critical Heat Flux Research

Although all three mechanistic models are based on experimental observations, recent experimental data suggests that there is still potential for improvement, both for the modeling of boiling phenomena in general as well as the CHF phenomenon in particular. For example, the thermal response of the heater substrate to nucleation events on the surface is disregarded in the above models. Recent research on dry-spot behavior at the wall in pool boiling has provided evidence that CHF is closely associated with the thermal behavior of dry patches at the wall [25, 29, 102]. The interaction between the fluid and the surface is not adequately considered in any of the models discussed above as they all postulate a hydrodynamic limitation of the boiling process. A strong dependence of CHF on the wetting properties of the fluid at the surface [103] suggests that the triple-phase contact line between vapor, liquid and the heater material plays an important role in the initiation of the boiling crisis. The unbound growth of residual vapor structures on the heater surface has been linked closely to the increase in apparent contact angle [104]. Additionally, CHF is treated as an independent phenomenon in the models discussed above. As pointed out by Lüttich et al. [23], existing correlations are often only valid for one of the boiling regimes due to limited experimental data along the entire boiling curve. It appears reasonable to assume that the different physical phenomena contributing to overall heat flux in the nucleate boiling regime interact in a way which eventually causes CHF. For a universal boiling model, the governing physical parameters need to be identified and modeled along the entire boiling curve for both pool and flow boiling.

For pool boiling, the experimental progress in recent years has led to a much better understanding of the boiling process and the mechanisms leading to CHF. In the nucleate boiling regime, microlayer theory [27, 105–109] predicts that heat transfer is governed by microlayer evaporation, micro-convection

and transient conduction in the immediate vicinity of the triple-phase contact line. Nishi et al. [110] found that area-averaged contact line density at the boiling surface correlates well with high boiling heat flux around CHF. Lüttich et al. [23] measured the evaporation rate at the triple-phase contact line at the boiling surface with fiber-optic microprobes along the entire boiling curve for pool boiling. They showed that the entire boiling curve correlates well with the contact line density and proposed that either this parameter or the interfacial area density should be used for a unifying mechanistic heat transfer model for the entire boiling curve.

Many studies on the fundamentals of the boiling crisis linked the existence of unquenchable dry-spots on the heater surface with the occurrence of CHF [25, 28, 29, 111–113]. Theofanous et al. [26, 27] found quenchable dry-spots on the heater surface below CHF. They observed the formation of irreversible dry-spots at CHF, which are never rewetted. These dry-spots grew to cover the entire boiling area, which led to heater failure. Several other authors confirmed this behavior, for example Gong et al. [28] and Kim et al. [29]. Ha and No [114, 115] postulated that the formation of an irreversible dry-spot occurs when a critical number of bubbles form around an active nucleation site of a departing bubble and inhibit bulk liquid supply as schematically depicted in Fig. 2.6.

Departing bubble with reversible dry-spot

Heavy nucleation at the triple-phase contact line
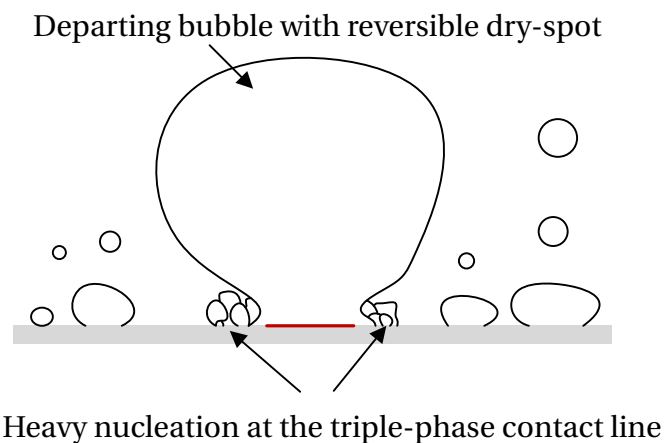
Figure 2.6: Hydrodynamic limitation of the liquid supply to a reversible dry-spot, adapted from Kim et al. [29].

This postulate is supported by the work of Chung and No [116], who investigated the dynamics of dry-spots using high-speed videography. They observed an accumulation of nucleation events around a large dry-spot close to CHF inhibiting the quenching of the dry surface area. Chu et al. [111, 112]

reported similar behavior and concluded that CHF is triggered by the irreversible expansion of dry-spots to a dry-patch due to the lateral merging of surrounding void structures as shown in Fig. 2.7.
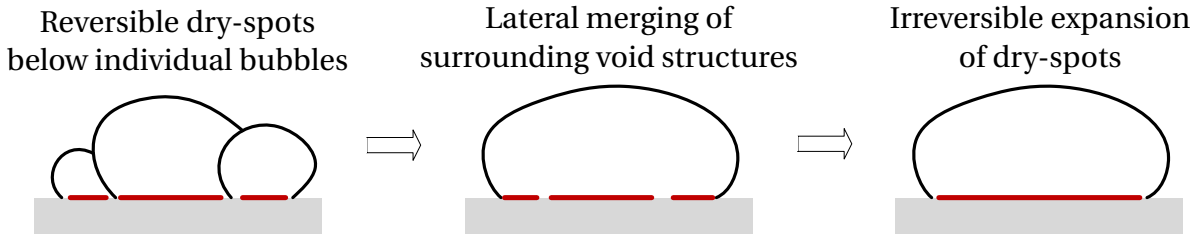
Figure 2.7: Dry-patch formation due to lateral merging of void structures, adapted from Choi et al. [117].

Kim et al. [29] found irreversible dry-spots on the heater surface below the Leidenfrost temperature by means of IR thermography. They observed irreversible dry-spot formation from the cyclic coalescence of shrinking and re-expanding residual vapor on the heater surface from individual nucleation events. After the dry-spot could not be rewetted for several milliseconds, it expanded quickly to cover the entire heater area. During the expansion, the regions not yet covered by the dry-spot maintained a high nucleation site activity. Jung et al. [25] observed increasing dry-spot sizes as wall heat flux was increased. This resulted in longer dry-spot lifetimes as CHF was approached. When heat flux was increased above CHF, rapid coalescence between active nucleation sites was observed alongside a sudden increase in the dry area fraction on the heater surface. New mechanistic models for the prediction of CHF in pool boiling have been proposed based on these findings, for example by Choi et al. [117]. To date however, only few studies have found evidence for the formation of dry-spots in flow boiling, for example [31, 32, 118].

Many studies on dry-spot phenomena were conducted using infrared thermometry to measure the surface temperature distribution of very thin heaters. This disregards the effects of the thermal properties of the heater substrate, which has been shown to heavily influence the boiling process in the nucleate boiling regime and at CHF [30, 33, 34]. Additionally, only few studies on the morphology of the void phase during the CHF transient have been published so far. Most of them were conducted for pool boiling, for example [30, 34, 119]. A lack of experimental data for flow boiling in close proximity to the boiling surface was noted in [20]. Auracher and Marquardt [30] state the need for further studies on the geometry, dynamics and stability of

dry-spots as well as studies on the general behavior of the two-phase mixture in close proximity to the heater surface along the boiling curve. This is especially true for flow boiling. Further small scale fundamental experiments are therefore needed for flow boiling to

- support the supposition that, like for pool boiling, the triple-phase contact line density on the heater surface is the governing parameter for boiling heat transfer along the entire boiling curve up to CHF,

- and to identify the contributing parameters to the stability limit of the boiling process and their evolution along the boiling curve.

2.4.4 Next-Generation Mechanistic Critical Heat Flux Models for Computational Fluid Dynamics

In contrast to empirical correlations and the classic mechanistic models, CFD provides the ability to simulate transient fluid flow and heat transfer and provides the spatial and temporal distribution of all simulated parameters. Next-generation mechanistic CHF models designed for CFD, for example by Ding et al. [19] and by Baglietto et al. [18, 120] are beginning to incorporate some of the experimental findings highlighted in the previous section.

2.4.4.1 Prediction of Critical Heat Flux Initiation in Pool and Flow Boiling

Ding et al. [19] introduced a new mechanistic concept for the quantitative prediction of CHF for use in CFD codes based on an analysis of the time scales involved in the boiling process at the cavity of a characteristic nucleation site. Following the work of Le Corre et al. [33], the authors attempt to explain why the rewetting process at CHF is not able to prevent the wall temperature from continuously rising anymore. The key novelty is the consideration that CHF is initiated by the thermal interaction of individual nucleation events on the heater surface with the heater substrate.

The concept calculates the surface heat flux during a representative bubble cycle at a characteristic nucleation site, which consists of four phases: (i) inertia-controlled growth, (ii) thermal-diffusion-controlled growth, (iii) bub-

ble departure and (iv) quenching at the heater wall. Three time scales are considered during this cycle: The combined bubble growth time t_g, the bubble condensation time t_c for subcooled boiling and the waiting time t_w of either the recovery of the thermal boundary layer after quenching or the cavity until it can be reactivated to form a new bubble. The mean surface heat flux during a bubble cycle is calculated using the removed heat per bubble period Q according to Eq. (2.19).

$$\dot{q} = \frac{Q}{\pi \left(r_{\mathrm{lig}} \right)^2 \left(t_g + t_c + t_w \right)} \tag{2.19}$$

The limitation of the boiling process: The model uses the work of Zhao et al. [107] to calculate the individual time scales of the representative bubble cycle. Before the bubble cycle closes after bubble departure, a certain waiting time passes until a new bubble is formed at the representative nucleation site. It is assumed that the cavity of the nucleation site is filled with liquid except for a small volume of remaining vapor at the bottom of the cavity. To form a new bubble, the liquid in the cavity needs to be at a certain superheat. Three modes of bubble formation are distinguished along the boiling curve:

1. In the nucleate boiling regime at low wall superheat, heat conduction through the heater substrate towards the liquid inside the cavity is the main heat removal mechanism for the cavity after bubble departure. Because the superheat of the heater substrate is relatively low in this regime, it is assumed that the activation time t_a of the cavity until a new bubble can be formed is much longer than the recovery time t_r of the thermal boundary layer. Hence, the cavity activation time governs the waiting time t_w at low wall superheat.

2. The enclosed vapor volume below the liquid inside the cavity leads to higher local superheat in the heater substrate at the bottom of the cavity. This decreases the cavity activation time for increasing wall superheat. At some point, the heating of the liquid inside the cavity occurs at the same rate as the recovery of the thermal boundary layer in the vicinity of the heated surface. The activation time of the cavity and the recovery time t_r of the thermal boundary layer are the same. At this point, the

waiting time t_w is equal to the recovery time of the thermal boundary layer, which is calculated according to Eq. (2.20).

$$t_r = \left(\frac{\pi \lambda_l}{2 \dot{q}} \right)^2 \frac{(T_w - T_l)^2}{\pi a_l} \tag{2.20}$$

3. For even higher wall superheat, the activation time of the cavity becomes smaller than the recovery time of the thermal boundary layer. This state is unstable and marks the beginning of transition boiling. As the forming bubble expands into the not-yet recovered thermal boundary layer, it transfers additional heat into it. This diminishes its capability to remove excess heat from the wall, which increases wall superheat and further shortens the cavity activation time. At some point, the surrounding temperature of the cavity becomes high enough to vaporize any liquid before it can reach the cavity. According to Ding et al., this marks the onset of film boiling.

Ding et al. postulate that the point where the recovery time of the thermal boundary layer becomes equal to the cavity activation time, i.e. $t_a = t_r = t_w$, governs the occurrence of CHF. The authors argue that this marks the last point where a boiling system is still stable. In their concept, this criterion is subsequently used to determine the onset of CHF.

2.4.4.2 Prediction of Critical Heat Flux in Multi-Phase Computational Fluid Dynamics

Baglietto et al. [18, 120] introduced an innovative framework for an improved multi-phase CFD boiling model. Like the majority of all multi-phase CFD heat transfer models, it is based on a heat partitioning approach by Kurul and Podowski [121] given in Eq. (2.21).

$$\dot{q} = \dot{q}_{conv,l} + \dot{q}_{evap} + \dot{q}_{quench} \tag{2.21}$$

In this equation, total heat flux $\dot{q}$ is the sum of several individual components. In the above case these are the heat flux due to liquid convection $\dot{q}_{conv,l}$, the

evaporation heat flux $\dot{q}_{\text{evap}}$ and the quenching heat flux after bubble departure $\dot{q}_{\text{quench}}$. Models based on this approach are generally referred to as »RPI boiling models«. They are usually highly sensitive to several closure parameters such as bubble departure diameter, bubble departure frequency and active nucleation site density [122, 123] and have been shown to require extensive calibration for different applications [6]. Baglietto et al. [18, 120] introduced an improved mechanistic modeling framework based on the general concept of surface heat flux partitioning, which is supposed to circumvent these shortcomings. To improve the calculation of surface heat flux, their mechanistic model tracks

- the size and dynamics of bubbles on the heater surface,

- the area of the microlayer and the dry area beneath the formed bubbles,

- the area of influence of bubbles sliding on the heater surface,

- the quenching of the boiling surface after bubble departure and

- the statistical bubble interaction on the heater surface.

Total surface heat flux is partitioned into four main components:

1. The surface heat flux due to liquid forced convection. It includes the effect of bubble interaction and surface roughness to account for different surface properties.

2. The surface heat flux due to evaporation, which is comprised of (i) the heat transfer during the initial inertial growth of forming bubbles, (ii) the microlayer evaporation during the growth of bubbles attached to a nucleation site and (iii) the microlayer evaporation under the bubbles sliding on the heater surface.

3. The surface heat flux due to sliding conduction, which accounts for the disturbance of the thermal boundary layer by sliding bubbles and the associated stirring of surrounding single-phase liquid.

4. The surface heat flux due to quenching, which accounts for (i) the heat removal by single-phase liquid after bubble departure and (ii) the heat stored inside the heater substrate below the dry area of not-yet departed bubbles.

All of these heat flux components have a high dependency on the bubble departure diameter [120]. To provide improved accuracy in comparison to other RPI boiling models, the modeling of bubble detachment is extended. Three ways of bubble detachment are considered:

1. The departure into the bulk flow, where bubbles depart from a nucleation site without any further surface interaction.

2. The departure by sliding, where bubbles depart from nucleation sites by sliding along the heater wall.

3. The lift-off of bubbles, where sliding bubbles detach from the heater surface.

Temporary deactivation of nucleation sites: The model's main innovation is the modeling of the interaction between bubbles and the surface. First, the coalescence of sliding bubbles is considered, which influences the calculation of the bubble departure diameter. Second, the temporary deactivation of nucleation sites on the heater surface is modeled. Nucleation sites can be deactivated either by a lower surrounding temperature close to a bubble after nucleation or due to the overlapping of bubbles between neighboring nucleation sites. While traditional nucleation site density models provide an estimate for the total number of sites at which bubbles may nucleate [124], these models do not account for the likely inevitable interaction of bubbles at the surface at higher heat fluxes. For this, Baglietto et al. use a complete spatial randomness statistical method to calculate the probability of a temporary deactivation of nucleation sites with rising wall superheat. It is assumed that bubbles are randomly distributed and an effective number of bubbles $N_{\mathrm{eff}}^{''}$ is present on the heater surface [125]. This number is calculated according to Eq. (2.22), using the ratio of the growth time of a bubble t_{g} to the bubble period $1/f_{\mathrm{lig}}$ and the nucleation site density $N^{''}$ calculated according to Hibiki and Ishii [124].

$$N_{\mathrm{eff}}^{''} = \left(\frac{1}{t_{\mathrm{g}} + t_{\mathrm{w}}} \right) t_{\mathrm{g}} N^{''} = f_{\mathrm{lig}} t_{\mathrm{g}} N^{''} \tag{2.22}$$

A nearest-neighbor method is then applied to determine the probability P of a nucleation site being within one bubble radius of another nucleation site according to Eq. (2.23).

$$P = 1 - e^{-N_{\text{eff}}^{''} \pi \left(\frac{l_{\text{lig}}}{2} \right)^2} \tag{2.23}$$

The number of active nucleation sites is then calculated as

$$N_{\text{active}}^{''} = (1 - P) N^{''}. \tag{2.24}$$

This limits the number of available nucleation sites, which eventually reaches a saturation condition at higher wall superheat. This is schematically illustrated in Fig. 2.8.
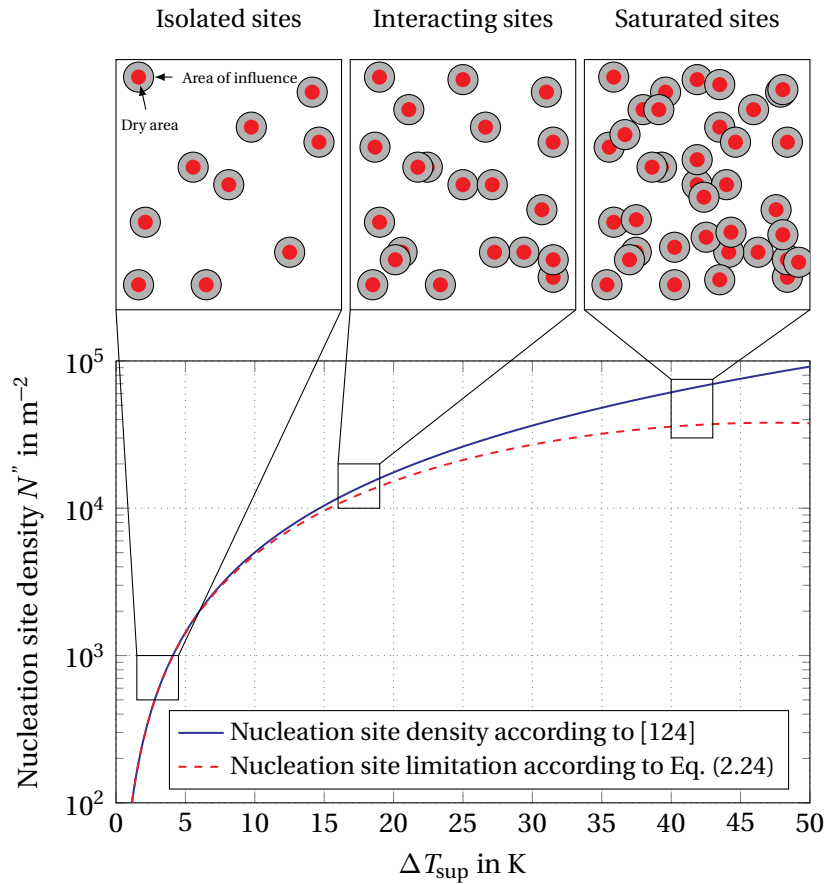
Figure 2.8: Schematic illustration of the limitation of available nucleation sites on a heater surface in comparison to traditional nucleation site models. Adapted from [120].

Limitation of the boiling process: Similar to the findings of Le Corre et al. [33] and based on the dry-spot literature presented before, the authors argue that this limitation of available nucleation sites leads to a natural limitation of the heat transfer at high wall superheat. An increasing number of nucleation sites are activated after the onset of nucleate boiling with rising wall superheat. This induces all the heat transfer mechanisms associated with boiling mentioned above and leads to an exponential increase in overall heat transfer across the boiling surface as illustrated in Fig. 2.1. As more nucleation sites are activated, the formed bubbles begin to interact and temporarily deactivate new nucleation sites. The fraction of dry area on the heater surface increases, which leads to a continuous reduction of the rate of increase of overall heat transfer. When the surface reaches a saturation condition for active nucleation sites, the number of bubbles which can be formed cannot increase further. At some point the heat transfer mechanisms are not able to keep up with the increase in surface temperature and total heat flux will reach a maximum. This represents a critical condition as an increase in surface temperature is not balanced by the same increase in surface heat flux. This eventually leads to an exponential increase in surface temperature and constitutes CHF.

2.5 Measurement Techniques in Boiling Research

The modeling of boiling phenomena requires an understanding of the underlying physical mechanisms of the process looked upon. Therefore, the modeling process heavily relies on the availability of measurement data to substantiate the mathematical formulation of a model. In two-phase flow, measurements can be conducted in the flow itself or in the surrounding walls of the flow channel. Measurements can generally be classified into time-averaged and transient measurements. Regarding time-averaged measurements, global steady-state system characteristics, local time-averaged values or one-dimensional (e.g. values averaged over a cross-section), two-dimensional (e.g. local averaged values over a cross-section) or three-dimensional data are commonly obtained. Regarding transient measurements, usually local transient data is collected. Measurement techniques can be classified according to their influence on the measurement itself and are split into two main groups: non-invasive measurement techniques and in-

vasive measurement techniques. The former do not affect the process to be measured while invasive techniques, in the case of two-phase flow are inserted directly into the flow and hence pose a possible disturbance. In the following, an overview about commonly used measurement techniques in two-phase flow research is given.

2.5.1 Measurements in Two-Phase Flow

General reviews on measurements in multi-phase flows are available by Hewitt [126], Boyer et al. [127], Mewes and Tauscher [128] and Mayinger and Feldmann [129]. The later two have an emphasis on optical measurement techniques.

2.5.1.1 Non-Invasive Techniques

Photography and videometry: Photography and videometry are commonly used for two-phase flow of transparent liquids. These measurement techniques allow for an easy interpretation but are prone to misunderstandings. They are depth-integrated and may suffer from a limited field of depth. For videometry, the number of images which can be recorded per measurement is usually limited due to the need for high frame rates. This results in either recording times too short for observing processes on a longer time scale (like transition processes or the passing of periodic events in the vapor layer) or long recording times with intervals between the pictures too long for the observation of for example bubble formation or bubble coalescence. Despite these shortcomings, both photography and videometry have been extensively used in boiling research in the past [59, 65, 76, 96, 101, 130–132].

Shadowgraphy and schlieren: These well-known optical measurement techniques require a rather simple setup for the visualization of density gradients in transparent media. A detailed description of the optical setup can be found in [133]. Desse and Deron [134] concluded that while shadow and schlieren measurements provide an easy-to-implement measurement technique for qualitative data, obtaining quantitative data proves challenging.

Despite this assessment, shadowgraphy and schlieren have been used as velocimetric techniques in turbulent single-phase flows with promising results [135, 136]

Holographic interferometry: Holographic interferometry detects variations in optical path lengths in a transparent medium. A detailed description of the technique can be found in [137] and [138]. The technique has been applied in multi-phase research before, for example [139] and [140], and was used to visualize density gradients in boiling processes in [77]. Holographic interferometry too is depth-integrated and therefore suffers from the same shortcomings as mentioned above. Moreover, a rather sophisticated optical setup is required and the numerical reconstruction techniques for recorded images are far from trivial. To the knowledge of the authors, other interferometric techniques like Michelson interferometry or electronic speckle pattern interferometry to this point have not been used in boiling research.

Laser-based techniques: A commonly used laser-based measurement technique is particle image velocimetry (PIV). This technique uses a laser sheet to illuminate tracer particles submerged in the flow, which are then captured by a high-speed camera. The displacement of the particles in each subsequent frame can then be used to calculate the local velocity of the flow. Detailed descriptions of the technique can be found in [141] and [142]. PIV has been used successfully in two-phase flows before [8].

Another well-known laser-based techniques is laser doppler anemometry, where the relative motion between a laser and seeding particles induces a doppler wave shift. This shift is then used to calculate the flow velocity. Details can be found in [143]. In the last decade, laser doppler anemometry was used extensively to determine the liquid velocities in bubble columns with high gas throughput [127]. Similarly to laser doppler anemometry, phase doppler anemometry uses the doppler effect of the reflected light to gain access to the flow velocities but uses two photo detectors to additionally measure the phase difference between the two signals. For a known geometry, this phase difference can then be directly correlated to particle size. According to Boyer et al. [127], phase doppler anemometry is currently limited to applications with small spherical bubbles and low void fractions. Although in principal

non-invasive, these techniques usually use tracer particles to capture the motion of the flow. This possibly contaminates heater surfaces and can introduce systematical errors to the measurement. Moreover, measurements at high void fractions are challenging due to bubbles obstructing the laser beam and high reflections from the void in the flow channel.

Radiographic techniques: Radiographic measurement techniques, an extension of the traditional photographic techniques, use high-energy radiation to analyze flow conditions. Typically, γ-rays or x-rays are used [144]. The advantage is the ability to measure hydrodynamic parameters even in non-transparent fluids. Traditional radiographic techniques suffer from the same shortcomings of photographic measurements like depth integration and the inability to reliably analyze for example several bubble layers at once. Radiographic tomography overcomes this shortcoming and provides three-dimensional access to flow channels. However, this technique usually only provides small spatial resolutions and because the measurement time is source dependent, can sometimes only be used for steady-state flows [127].

Thermocromatic liquid crystals: Thermocromatic liquid crystals can be used to measure temperature fluctuations in the immediate vicinity of the boiling activity. Thermocromatic liquid crystals are usually applied on the backside of a thin heated foil as a continuous layer. When heated, thermocromatic liquid crystals reflect a distinct color depending on temperature when subjected to white light. The reflections can then be used to calculate quantitative temperatures on the surface of the heated foil. This experimental approach has been used by Sodtke et al. [145] to verify a nucleate boiling heat and mass transfer model on a microscopic scale. Other authors have successfully used thermocromatic liquid crystals in flow boiling applications to investigate heat transfer characteristics [146–148]. Kenning et al. [149] have discussed the advantages and limitations of liquid crystal thermography with regards to their ability to provide necessary information for the development of deterministic nucleate boiling models. While highlighting the valuable insights from using thermocromatic liquid crystals, the authors point out the narrow boiling regimes for which thermocromatic liquid crystals can be applied. Due to the low thermal mass of the thin foil where the boiling activity

takes place, it was therefore deemed unlikely that this technique can be used at high heat fluxes for CHF measurements.

Infrared imaging: Infrared imaging techniques are able to deliver time-resolved and space-resolved information about bubble nucleation and heat transfer mechanisms at the surface of a heater. This technique has been deployed in nucleate pool boiling by Gerardi et al. [150], who used a thin electrically heated foil on a sapphire substrate for their measurements. While studies on nucleate pool boiling are often far from direct technical applications, infrared thermography was recently used in an industrially relevant setup by Visentini et al. [151], who investigated rod-clad failure during transient boiling. Flow boiling applications include [146, 152, 153]. However, like in the case of thermocromatic liquid crystals, the thin and sophisticated heater construction hinders the use of this measurement technique in most applications where very high heat fluxes need to be applied to system with technically relevant heater dimensions.

2.5.1.2 Invasive Techniques

Boyer et al. [127] note that despite the advancement of optical and tomographic techniques for the analysis of two-phase flow, invasive measuring cannot be fully avoided. Especially for turbulent systems at high void fractions, non-invasive measurements become prone to uncertainties. Moreover, non-steady-state phenomena are often cumbersome to analyze and equipment for non-invasive measurements is generally more expensive. Therefore, many studies in boiling heat transfer research are conducted using invasive technology.

Thermocouples: Thermocouples are likely the most common and well-known invasive measurement devices. Available in many different sizes for many different uses, they have been used for discrete temperature measurements in countless publications. Due to their wide-spread use in the scientific community, it is deemed unnecessary to explain this technique in more detail.

Wire-mesh sensors: Wire-mesh sensors (WMS) are devices which are inserted into the flow to measure the local void fraction at discrete points in a plane in the flow channel. There are two main groups of WMS, conductive WMS as introduced by Prasser et al. [154] and capacitance WMS as introduced by Da Silva et al. [155]. A comparison between WMS and γ-ray densitometry was given by Sharaf et al. [156], who concluded that WMS performed better regarding the accuracy of the measurements especially at the edges of a flow channel. However, as seen in [157], WMS are highly invasive and lead to fragmentation and break-up of bubbles.

Hot-wire anemometry: Hot-wire anemometry has been available for single-phase flow for a long time and is experiencing increased attention in the field of two-phase flow [127]. Hot-wire anemometry uses the heat exchange between a very thin electrically heated wire-probe and the surrounding fluid to measure the voltage drop at the heated wire, which is dependent on the phase present at the probe. The reliability for air-water mixtures was shown by Utiger et al. [158]. Although hot-wire anemometry is not a very expensive technology and it can be applied in many media, its application is limited by some of its technical characteristics. For example, high momentum flows have to be avoided as not to damage the probe, due to the fragile wires. Moreover the signal interpretation is challenging for turbulent and low velocity flows [127].

Fiber-optic microprobes: Fiber-optic microprobes are very thin glass fibers, which are inserted into the flow channel to measure parameters like local void fraction or the velocity of the fluid at the probe tip in high void fraction environments. Fiber-optic microprobes usually face the direction of flow and pierce oncoming bubbles. Due to the change in the refractive index, the probe tip either reflects the light from a light source or transmits the light into the flow channel. This results in a series of light pulses for intermittent two-phase flow, which can then be analyzed. A lot of work regarding this measurement technique was done by the groups of Auracher [23, 24, 34, 119, 159], Cartellier [160–168] and Bloch [8, 17, 48, 169], who successfully used fiber-optic microprobes for local void fraction measurements in boiling systems. A combination of multiple probes can be used to measure further pa-

rameters such as bubble velocity and bubble diameter as shown by Lim et al. [170]. Lüttich et al. [23] stated that optical probes are the only means to measure interfacial phenomena in terms of liquid-vapor fluctuations very close to the surface of both thin or thick heaters. They provide the only data base to extract useful information about the interfacial evolution in boiling processes on technically relevant heaters. This highlights the importance of this measurement technique for boiling research.

2.5.2   Measurements in Surrounding Walls

While the vast majority of parameters of interest occur at the boiling surface or within the two-phase flow itself, measurements in surrounding walls need to be conducted to complement the two-phase flow data. Usually, the walls of the flow channel are equipped with measurement technology to measure surface temperatures and heat flux. The actual surface temperature, which is needed to calculate the heat flux that the fluid is subjected to, is not trivial to obtain. The prevalent way of measuring temperature in surrounding walls is to use thermocouples. These can be directly attached to the heater surface, which yields accurate values for the surface temperature of a heater in a relatively fast manner but also potentially interferes with bubble formation and disturb the flow at the heater surface. Therefore, many experimental apparatus use thermocouples mounted at different distances from the boiling surface inside the heater, as shown in [17, 48]. Surface temperature is calculated via the temperature gradient, which is then used to subsequently calculate the heat flux transmitted through the heater. This procedure is widely used and offers reasonable accuracy. However, it is only possible if the heater thickness allows for installation of at least two thermocouples. Thus, it is not possible to use this approach in thin heated pipes, foils or similar devices. Other approaches to obtaining the wall temperature have been investigated by for example Celata et al. [130], who used the physical expansion of a rod heater to calculate its wall temperature. As this methods only yields an average surface temperature and therefore overall heat flux, it is not well suited for investigation of CHF using larger and more complex heater geometries.

Chapter 3

Experimental Setup

This chapter describes the experimental setup, the measurement techniques used for data acquisition, the post-processing of measurement data and the measurement procedure. Experiments were conducted with the refrigerant Novec 649 using two different heater configurations in a square flow channel at several mass fluxes and subcoolings. Single-fiber and double-fiber optic microprobes were used for the acquisition of quantitative data about the void phase in the flow channel and the immediate vicinity of the heater wall.

3.1   Boiling Test Rig

Fig. 3.1 shows a schematic depiction of the boiling test rig. The fluid is circulated through the system by a centrifugal pump. Mass flux can be varied between $G = 500\,\mathrm{kg\,m^{-2}\,s^{-1}}$ and $G = 2000\,\mathrm{kg\,m^{-2}\,s^{-1}}$. The main flow loop during data acquisition is marked in bold blue. The vertically oriented stainless steel test section has a total length in flow direction of 500 mm and a square cross section of 40 mm by 40 mm. Due to its modular design, different heaters and measurement modules can be fitted. After passing the test section, the two-phase mixture is condensed and cooled down in a counter flow heat exchanger. Any remaining gaseous fluid is separated from the main flow in a phase separator and condensed in a reflux condenser, which is open to the environment and mounted at the highest point of the test rig. Thus, no pressure other than the hydrostatic pressure is imposed on the test section. A preheater with a maximum power of 3 kW is installed before the inlet of the test section and controls the inlet subcooling. Subcooling can be varied between $\Delta T_{\mathrm{sub}} = 33\,\mathrm{K}$ and $\Delta T_{\mathrm{sub}} = 1\,\mathrm{K}$. Temperature measurements at positions »1« and »2« determine the amount of preheater power needed. A pressure measurement at position »2« is used to determine the saturation temperature of

the fluid at the inlet of the test section. To reach critical heat flux and capture a full transition to film boiling at moderate temperatures, a fluid with a low boiling point is used in the experiments. The fluid used in this study is Novec 649. Its boiling point at ambient conditions is 49 °C and it has an evaporation enthalpy of 88 kJ kg^{-1}. Its thermal stability limit is approximately 300 °C. Its main physical properties in comparison to water are given in Table A.1 in Appendix A for saturation conditions at the inlet pressure of the test section of 1.15 bar.
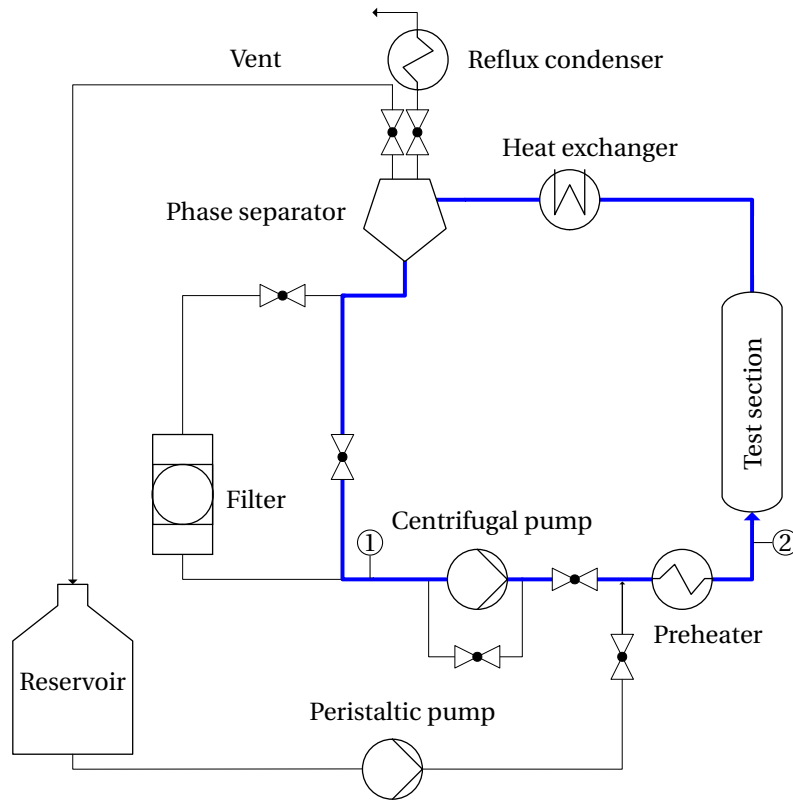
Figure 3.1: Schematic of the boiling loop (main flow loop is marked in bold blue).

3.2   Heater Configurations

Two heater configurations were used in this study: a wall-mounted copper heater and a single-rod copper-coated stainless steel heater.

3.2.1 Wall-Mounted Copper Heater

The test section with the wall-mounted heater installed is shown in Fig. 3.2. The boiling surface begins 150 mm downstream of the inlet of the test section. The boiling surface of the copper heater is mounted flush in the middle of the right-hand-side wall of the test section in Fig. 3.2. The boiling surface has a width of 15 mm and a length of 200 mm. As depicted in Fig. 3.3, the boiling surface is the tip of a copper bar with the same cross section extending from a large copper block, which accommodates twelve heater cartridges with a combined maximum power of 2.4 kW. The copper bar is insulated from the surrounding steel wall of the test section by a silicone layer.
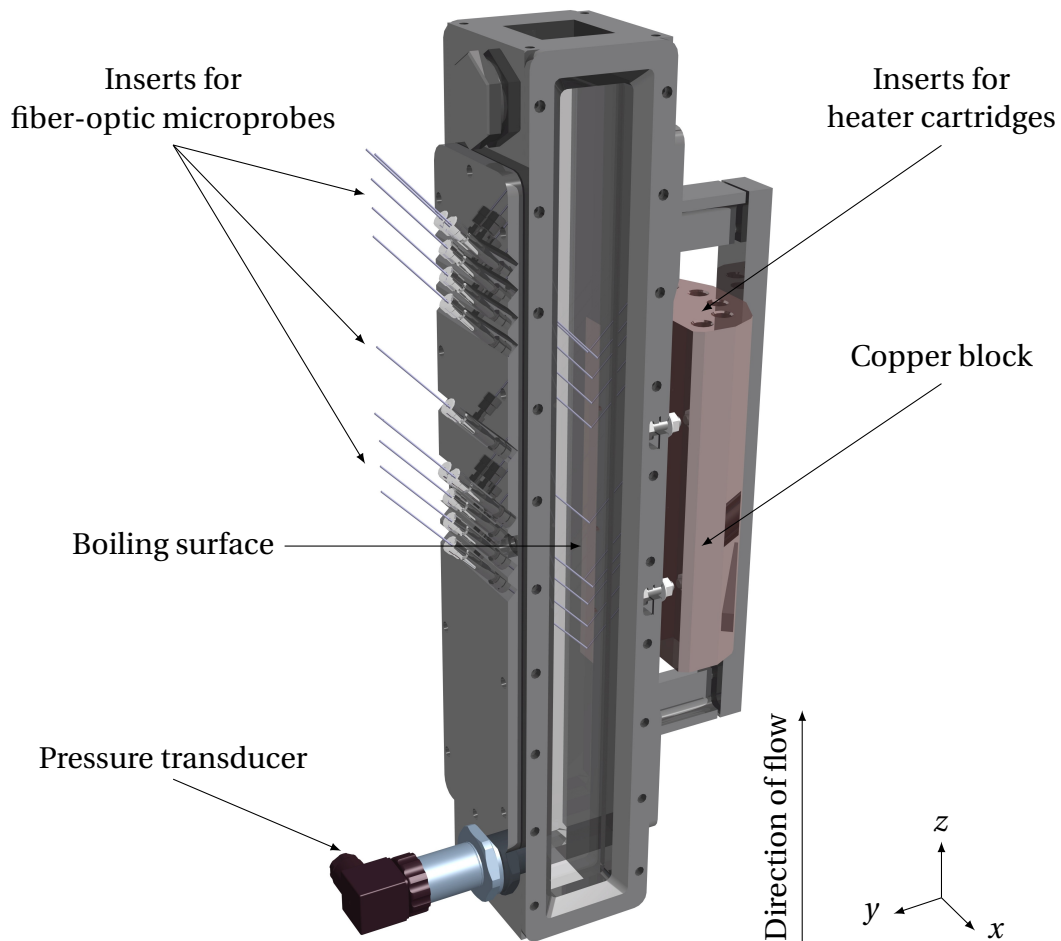
Figure 3.2: Three-dimensional view of the test section with the wall-mounted copper heater installed.
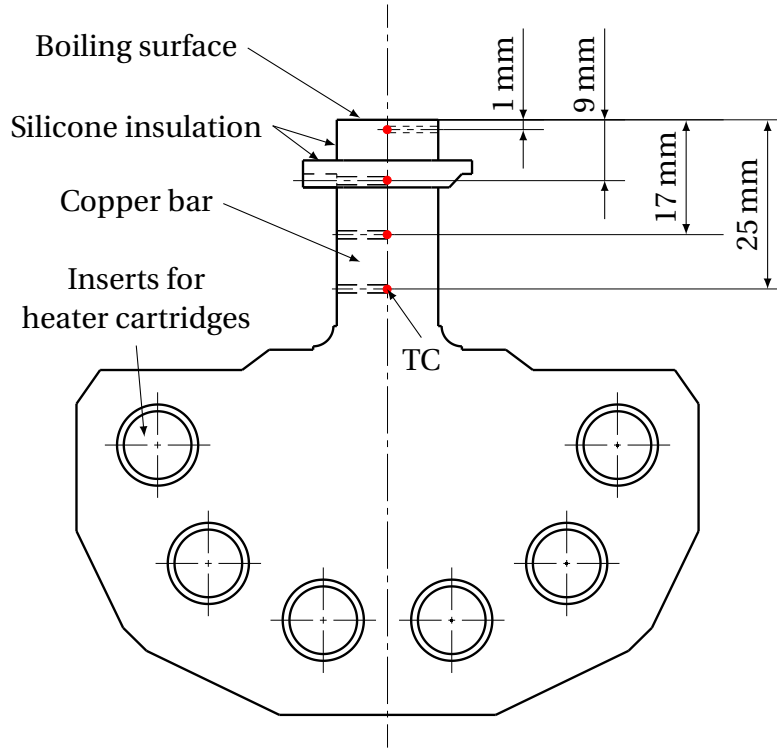
Figure 3.3: Schematic cut through the wall-mounted copper heater.

To measure heat flux and wall temperature, three rows of four thermocouples (TC) are mounted in the wall-mounted copper heater's plane of symmetry. The acquisition frequency for all temperature measurements in the test rig is 2 Hz. The thermocouple positions are schematically depicted in Fig. 3.4. Thermocouples of type T are used at $y = 1\,\text{mm}$ below the boiling surface and thermocouples of type K are used at $y = 9\,\text{mm}$, $y = 17\,\text{mm}$ and $y = 25\,\text{mm}$ below the boiling surface. Surface temperature is extrapolated quadratically using the temperature gradient between individual thermocouples of each thermocouple row (TCR). A numerical investigation of the heat transfer processes inside the heater during operation was conducted prior to this study. No substantial heat transfer in the direction of flow inside the copper heater was observed. As in [77, 171], heat flux is therefore calculated using Fourier's law for one-dimensional heat transfer according to Eq. (3.1).

$$\dot{q} = -\lambda_{\text{cu}}\frac{\Delta T}{\Delta y} - \rho_{\text{cu}}c_{\text{cu}}\Delta y\frac{\Delta T}{\Delta t} \tag{3.1}$$
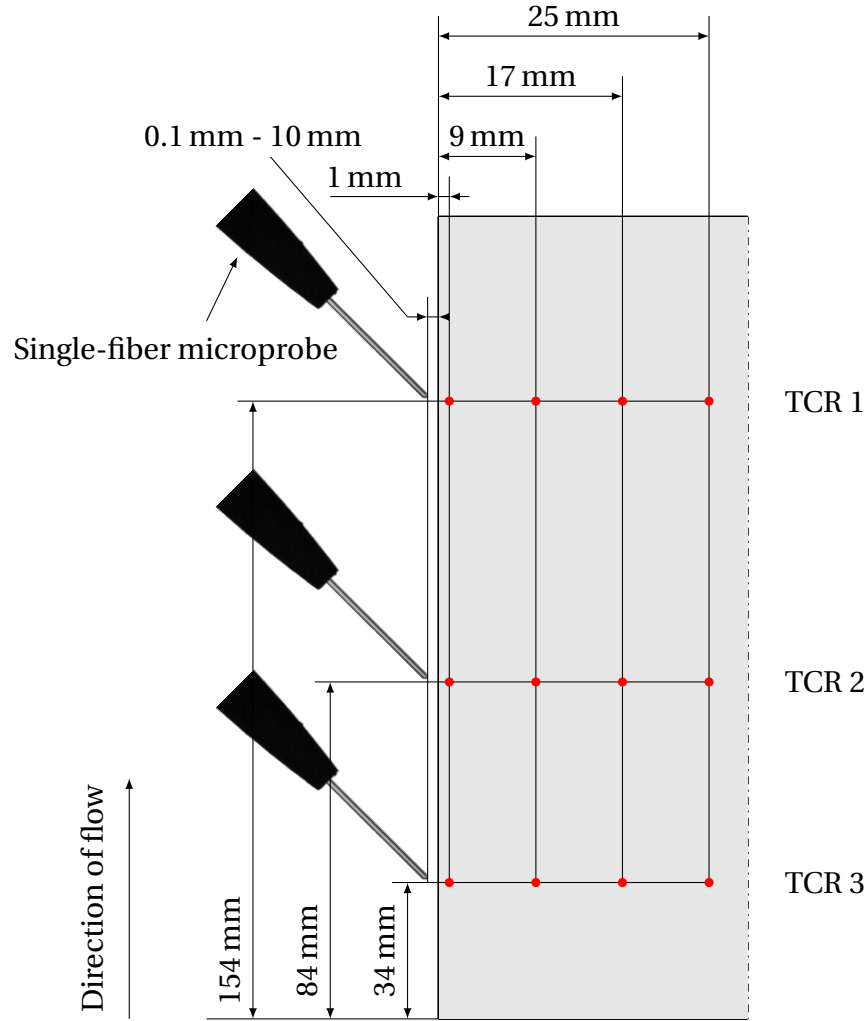
Figure 3.4: Schematic view of the positions of the fiber-optic microprobes (single-fiber microprobe configuration shown, not to scale) above the boiling surface and the thermocouples mounted inside the wall-mounted copper heater's plane of symmetry.

3.2.2 Single-Rod Copper-Coated Stainless Steel Heater

A schematic depiction of the single-rod copper-coated stainless steel heater inside the test section is shown in Fig. 3.5. The rod is placed in the axis of symmetry of the flow channel. It has a length of 585 mm and an outer diameter of 10 mm. The heated area is 200 mm long and begins 142 mm downstream of the inlet of the test section. Unheated areas at the upstream and downstream end of the heated area ensure a smooth development of the flow profile and eliminate the disturbance of the boiling process. The heater is electrically heated by a heating coil with a maximum power of 2.4 kW embedded

in Magnesium-oxide, which is encapsulated by a stainless steel tube with a wall thickness of 1 mm. The outside of the tube is copper-coated to eliminate differences in surface characteristics between the two heater configurations such as different nucleation site densities, wetting behavior and contact angles.
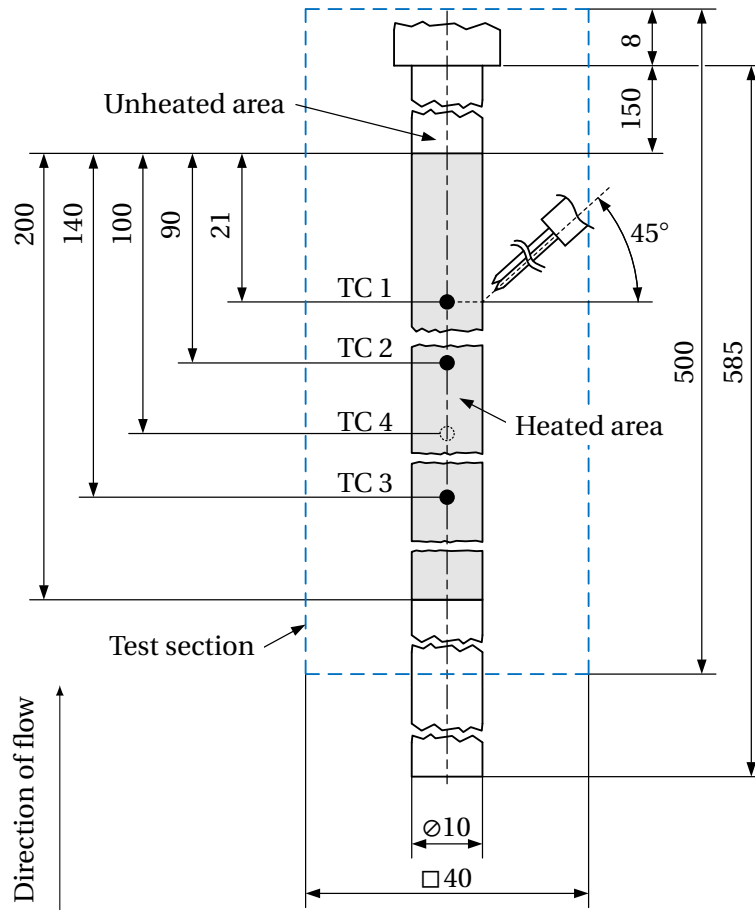
Figure 3.5: Schematic view of the positions of the fiber-optic microprobes (double-fiber microprobe configuration shown, not to scale) above the boiling surface and the micro-thermocouples fitted on the surface of the single-rod copper-coated stainless steel heater. All length specifications in mm.

Voltage and current measurements are used to calculate surface heat flux. To measure wall temperature and detect the occurrence of CHF, four thermocouples are used. Three micro-thermocouples (TC 1, TC 2, TC 3) of type T with a diameter of less than 0.25 mm are fitted on the heated surface. Additionally, a thermocouple of type J (TC 4) is fitted in the center of the heated area inside the heater in its axis of symmetry for CHF detection.

3.3 Fiber-Optic Microprobes

Fiber-optic microprobes were used for the acquisition of quantitative data about the void phase. Based on the law of Snellius [128], fiber-optic microprobes detect a change in refractive index for intermittent two-phase flow at the tip of the probe. Fiber-optic microprobes can be used to accurately measure interfacial phenomena very close to the surface of both thick and thin heaters. They therefore provide the only means to extract quantitative information about the interfacial evolution during the boiling process on technically relevant heaters [23]. This technique is widely used in the experimental analysis of two-phase flow, for example [3, 4, 10, 20, 23, 24, 77, 119, 159, 164, 165, 172]. Two types of fiber-optic microprobes were used in this study: Single-fiber microprobes and double-fiber microprobes. Single-fiber microprobes can be used to acquire quantitative data on void fraction and void frequency. Double-fiber microprobes allow for the additional measurement of void ligament velocity and void ligament length by cross-correlating the signals from the upstream and the downstream fiber.

3.3.1 Operating Principle

When a bubble touches the tip of the probe, light propagating within the fiber is reflected. When liquid is present at the tip, the light is transmitted into the flow channel. This results in a series of reflected light pulses for intermittent two-phase flow at the tip which can then be analyzed. Fig. 3.6a shows a schematic cut through an optical step-index fiber. The profile of the refractive index across the fiber is shown in Fig. 3.6b. The core is optically denser than the cladding. This means that the refractive index of the cladding n_2 is lower than the refractive index of the core n_1. Light propagates along the fiber by total reflection at the interface between the core and the cladding.

A beam emitted from a laser source is coupled into the fiber at its front face. The beam can be coupled into the fiber up to a maximum acceptance angle φ_0. Above this angle, the condition for a total reflection at the interface between core and cladding is not fulfilled anymore and the light intensity of the beam will be significantly attenuated while propagating along the fiber. The
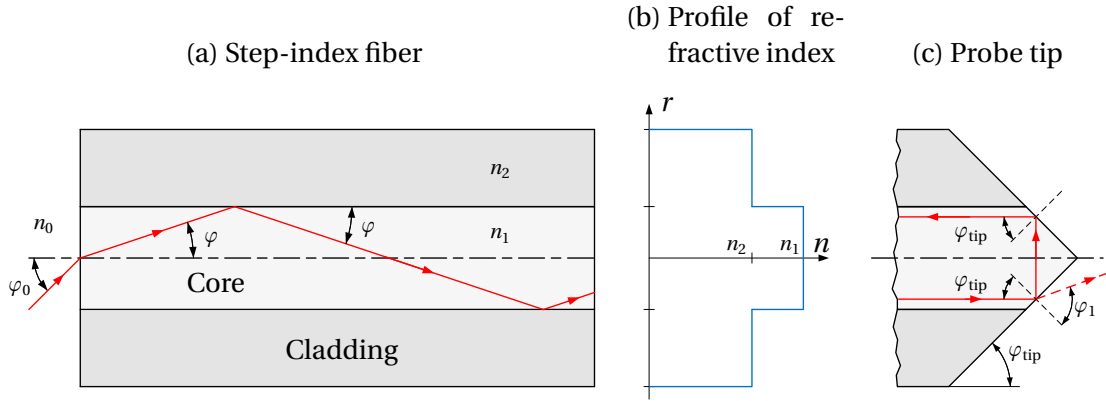
Figure 3.6: Beam propagation inside a step-index fiber and at the fiber microprobe tip for a tip angle of 45°.

maximum acceptance angle for a step-index fiber can be calculated based on Snell's law by using the maximum beam angle φ_{crit} for which a total reflection occurs at the interface between the core and the cladding. This angle is calculated according to Eq. (3.2).

$$\cos\varphi_{\mathrm{crit}} = \frac{n_2}{n_1} \tag{3.2}$$

If a beam hits the interface of the two materials at an angle $\varphi > \varphi_{\mathrm{crit}}$, the beam will propagate out of the core into the cladding. A dimensionless quantity called the numerical aperture NA, which specifies the acceptance angle, can be calculated according to Eq. (3.3) [173].

$$\mathrm{NA} = n_0\sin\varphi_0 = n_1\sin\varphi_{\mathrm{crit}} \tag{3.3}$$

All optical fibers used in this study have a value of $\mathrm{NA} = 0.22$. If a beam is coupled into the fiber with its front face subjected to air ($n_0 \approx 1$), the numerical aperture can be rewritten to

$$\mathrm{NA} = \sin\varphi_0 = n_1\sin\varphi_{\mathrm{crit}} = n_1\sqrt{1-\cos^2\varphi_{\mathrm{crit}}} = \cdots = \sqrt{n_1^2 - n_2^2}. \tag{3.4}$$

Depending on the angle of the probe tip as shown in Fig. 3.6c, a beam propagating within the fiber either will be coupled out of the fiber or it will be

reflected at the interface between the core of the fiber and the surrounding medium at the probe tip. For a conical probe tip and a laser beam propagating parallel to the axis of the fiber, the range of optimal probe tip angles for fluids with a liquid refractive index $n_l > 1.13$ and a vapor refractive index $n_g < 1.13$ is $43° \leq \varphi_{tip} \leq 51°$ [164]. The refractive indexes for Novec 649 are $n_l = 1.256$ and $n_g \approx 1$. Therefore, any probe tip angled within that range will allow the probe to distinguish between the liquid and the vapor phase. However, as a laser beam generally does not propagate purely parallel to the axis of the fiber, the angle of the probe has to be optimized to obtain an optimal signal-to-noise ratio. In this study, a probe tip with an angle of $\varphi_{tip} \approx 45°$ was found to yield the best results.

3.3.2 Measurement Setup

Fig. 3.7a and Fig. 3.7b show the two types of probes used in this study. The single-fiber microprobe can be used to measure void fraction and void frequency, whereas the double-fiber microprobe provides additional quantitative data on void ligament velocity and size. The probe tip consists of either one or two glass fibers with a core diameter of $50\,\mu m$ per fiber. Each fiber has a conical shape at an angle of approximately $45°$. The fibers are embedded in a steel ferrule for increased mechanical stability. For the double-fiber microprobes, the two individual glass fibers are glued together to ensure a fixed distance between the tips of each fiber. For both configurations, the measurement apparatus consists of the probe tip, a fiber-coupled laser source, a fiber coupler, a photodiode and an amplifier as well as an analog-to-digital converter running at $60\,kHz$ for each fiber. A closed and fully fiber-based beam path ensures a good signal-to-noise ratio and minimizes unwanted interference. The measurement apparatus for a single-fiber microprobe is shown in Fig. 3.8. The components used are summarized in Tab. 3.1.

Three fiber-optic microprobes were used simultaneously to measure void data at distances between $y \approx 50\,\mu m$ and $y \approx 10\,mm$ normal to the heater surface. A traversing mechanism with an accuracy of $\pm 5\,\mu m$ was used to position each probe relative to the heater surface. The position of each probe was optically verified with microscopic images for each measurement point before and after each experiment. Each probe was traversed individually to

(a) Single-fiber microprobe   (b) Double-fiber microprobe
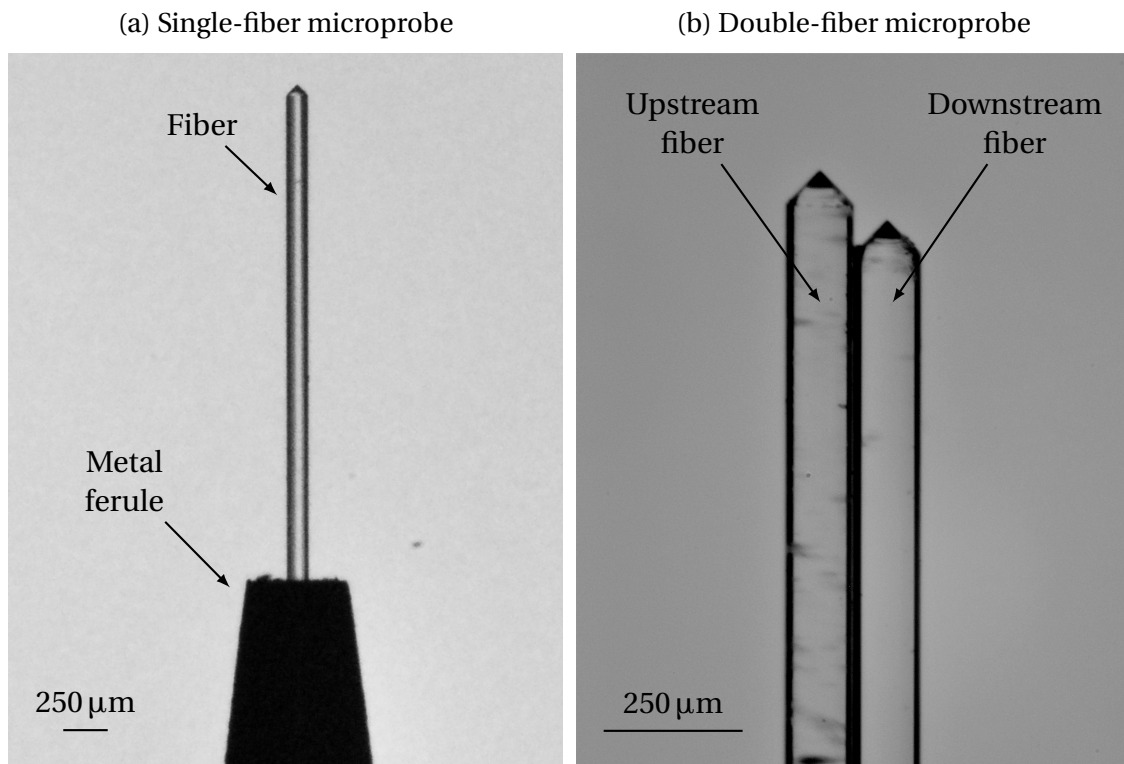
Figure 3.7: Microscopic images of the two types of fiber-optic microprobes used in this study.
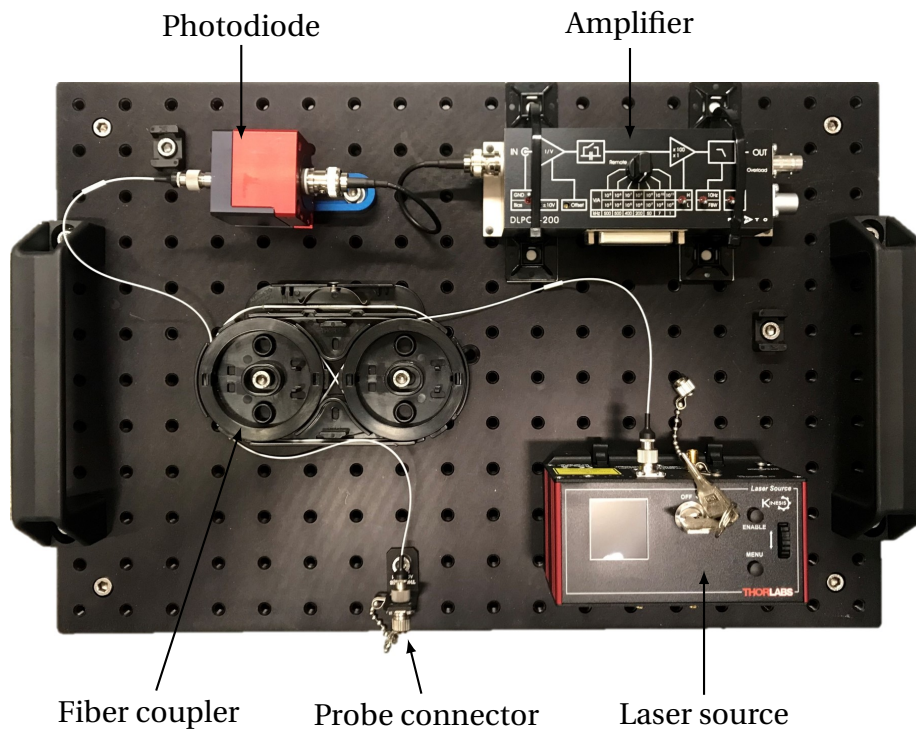
Figure 3.8: Measurement apparatus for a single-fiber microprobe.

Table 3.1: Components used for the measurement apparatus for a single-fiber microprobe.

Component	Name	Manufacturer
Optical fiber	Faserpigtail Easystrip FP5FC	all4fiber
Fiber coupler	FUSED-12-IRVIS-50/125-50/50-3S3S3S-1-1	OZ Optics
Photodiode	P-CUBE-20-FC	Laser Components
Amplifier	DLPCA-200	FEMTO Messtechnik
Converter	NI USB-6210	National Instruments
Laser source	TLS001-635	THORLABS

cover the entire distance range from $y \approx 50\,\mu m$ to $y \approx 10\,mm$. The fiber-optic microprobes are inserted into the flow channel at an angle of 45°. For the wall-mounted copper heater, one probe is placed above each thermocouple row. For the single-rod copper-coated stainless steel heater, the probes are placed above the micro-thermocouples. This allows for the locally coupled synchronous measurement of void and temperature data.

3.3.3 Post-Processing of Measurement Data

All void data is calculated based on a phase indicator function (PIF) according to Eq. (3.5). Fig. 3.9 shows a binarization sequence using Eq. (3.5). Based on the raw signal from bubbles touching the probe tip, a threshold voltage U_{th} is set above the noise floor in the raw signal. Using this voltage, the raw signal is binarized. A value of $PIF = 0$ corresponds to the liquid phase and a value of $PIF = 1$ to the void phase.

$$PIF = \begin{cases} 1 & \forall\, U > U_{\text{th}} \\ 0 & \forall\, U \leq U_{\text{th}} \end{cases} \tag{3.5}$$

This approach has been used similarly in other works, for example [10, 34, 174] as well as for the well-known experimental database by Garnier et al. [20]. A moving average approach was used to calculate mean values for a given time interval Δt_i containing a number of samples n. For the purpose of this study, $n = 30000$ was used, which for a sample rate of $sr = 60\,kHz$ results in
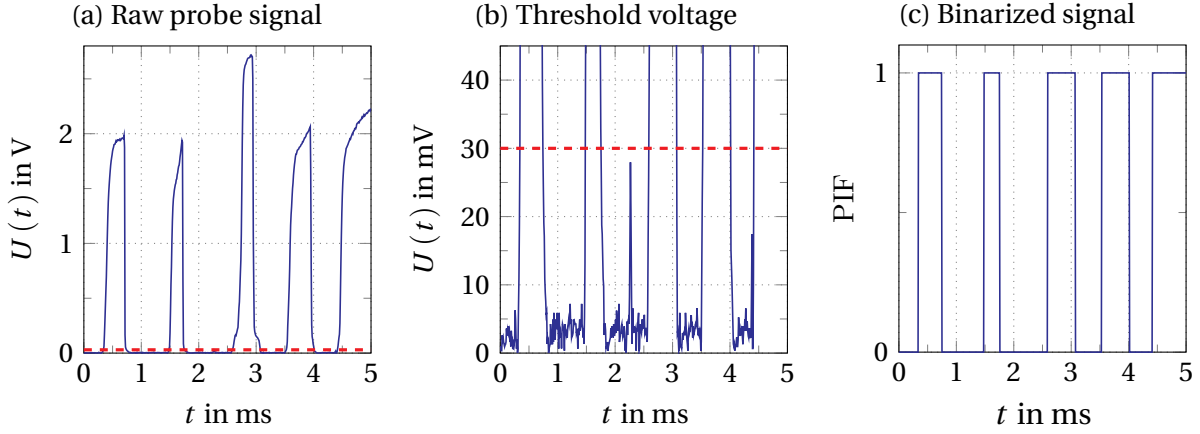
Figure 3.9: Binarization sequence from raw signal to the binary signal using a threshold voltage (red dashed line).

an averaging interval of $\Delta t_i = 0.5\,\text{s}$. This interval length was chosen to match the acquisition frequency of $2\,\text{Hz}$ for temperature data. The calculation of the void data in each interval was done as follows:

Void fraction: The local void fraction α was calculated according to Eqns. (3.5) and (3.6) for every time interval Δt_i. The ratio of the sum over each $PIF(j)$ to the total number of recorded samples n in the time interval is then equal to α during Δt_i. This approach has been used by other authors for the calculation of the void fraction from fiber-optic microprobes before, for example [77, 169].

$$\alpha(\Delta t_i) = \frac{1}{n}\sum_{j=1}^{n} PIF(j) \tag{3.6}$$

Void frequency: The void frequency f_{lig} is defined as the total number of detected void ligaments N_{lig} per time interval Δt_i according to Eq. (3.7).

$$f_{\text{lig}}(\Delta t_i) = \frac{N_{\text{lig}}}{\Delta t_i} \tag{3.7}$$

Contact time: For the calculation of void ligament velocity and size, the average contact time t_{lig} of ligaments per time interval is needed. The contact

time for a single ligament k is calculated by Eq. (3.8), where $n_{\text{lig}(k)}$ is the number of samples with a value of $PIF = 1$ for each ligament k. This is schematically shown in Fig. 3.10.

$$t_{\text{lig}(k)} = \frac{n_{\text{lig}(k)}}{sr} \tag{3.8}$$

The average contact time for each time interval is then calculated as

$$t_{\text{lig}}(\Delta t_i) = \frac{1}{N_{\text{lig}}} \sum_{k=1}^{N_{\text{lig}}} t_{\text{lig}(k)}. \tag{3.9}$$
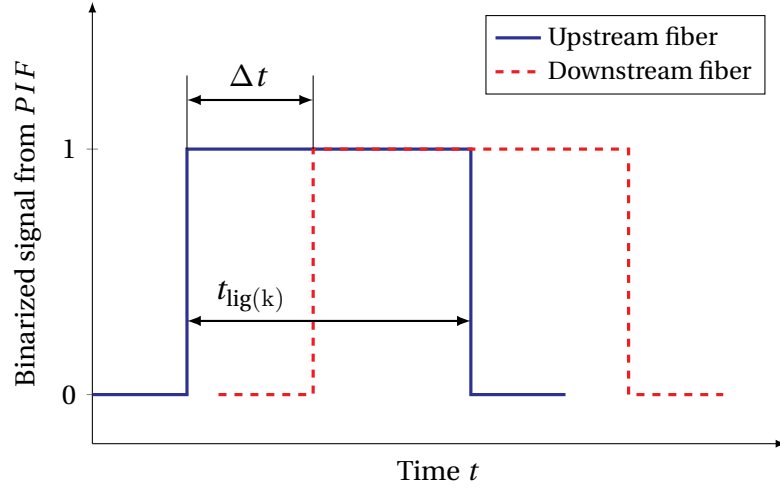
Figure 3.10: Schematic depiction of the time difference between the signals from the upstream and downstream fiber of a double-fiber microprobe, which is used for the calculation of void velocity.

Ligament velocity: The average ligament velocity u_{lig} is calculated using a time-of-flight method, similar to the approach used in [20]. The time Δt it takes a void interface to cover the distance l_{probe} between the upstream fiber and downstream fiber can be extracted from the data from the double-fiber microprobe setup. This is schematically shown for a generic binarized double-fiber microprobe signal in Fig. 3.10. By cross-correlating the signals of the two fibers for a given time interval, the mean time of flight $\overline{\Delta t}$ for all void ligaments in this interval is calculated. The vertical distance between the two fibers for all double-fiber microprobes used in this study was in the range of

$l_{\text{probe}} = 200\,\mu\text{m}$–$220\,\mu\text{m}$. This value is a compromise between the miniaturization of the probe tip and the distance needed to accurately measure the time of flight of the interface. The average ligament velocity of a given time interval is then calculated according to Eq. (3.10).

$$u_{\text{lig}}(\Delta t_i) = \frac{l_{\text{probe}}}{\overline{\Delta t}} \tag{3.10}$$

Ligament size: The mean ligament size l_{lig} for each interval is calculated by multiplying the mean velocity u_{lig} with the mean contact time t_{lig}.

$$l_{\text{lig}}(\Delta t_i) = t_{\text{lig}} \cdot u_{\text{lig}} \tag{3.11}$$

3.4 Uncertainty

Calibration experiments were conducted prior to this study. A deviation of approximately $0.2\,\text{K}$ was measured between any two thermocouples used in the test rig at ambient conditions. The position accuracy of the thermocouples inside the wall-mounted copper heater due to manufacturing inaccuracies is better than $0.1\,\text{mm}$. For the single-rod copper-coated stainless steel heater, current and voltage could be measured with uncertainties of $0.1\,\text{A}$ and $3\,\text{V}$ respectively. A Gaussian error propagation was calculated based on these values and yielded maximum absolute uncertainties of $\pm 10.7\,\text{kW}\,\text{m}^{-2}$ for surface heat flux and $\pm 0.9\,\text{K}$ for wall temperature. A maximum statistical fluctuation of $20\,\text{kg}\,\text{m}^{-2}\,\text{s}^{-1}$ for the mass flux was tolerated as a negligible influence on CHF and wall temperature was observed in reference experiments.

Videometric calibration experiments for the fiber-optic microprobes showed good agreement between the probe signals and the observed trajectories of bubbles. The typical uncertainty for void fraction measurements with fiber-optic microprobes commonly found in literature (e.g.: [162, 170]) was equaled. The same uncertainty applies to other quantities calculated from the binarized fiber-optic microprobe signals using the phase indicator function given in Eq. (3.5). At the closest distance to the wall of $y \approx 50\,\mu\text{m}$, the gap

between the tip of the fiber-optic microprobe and the heater surface is in the same order of magnitude as the core diameter of the probe itself. While fiber-optic microprobes with similar geometric properties have been used at even closer distances in pool boiling [24, 119], the influence of the probe tip on the boiling process is not negligible. At distances greater than or equal to $100\,\mu m$, the signal-to-noise ratio was typically as depicted in Fig. 3.9. It noticeably deteriorated at closer distances. Hence, the uncertainty for fiber-optic microprobe measurements at a wall distance of $y \approx 50\,\mu m$ is likely larger compared to the measurements obtained further away from the boiling surface.

Some additional uncertainty for fiber-optic microprobe measurements arises from partially pierced bubbles. There are three main sources of error [161, 165, 172]:

1. A drifting effect, where the trajectory of a bubble is altered by the probe tip, which leads to a smaller detected chord.

2. A blinding effect, where small bubbles are not detected due to incomplete dewetting of the probe tip.

3. A crawling effect, where bubbles are deformed and decelerated during the piercing of the liquid-vapor interface.

Mena et al. [167] discussed the influence of each effect on the accuracy of fiber-optic microprobe measurements. The blinding and drifting effects lead to an underestimation of the residence time of detected bubbles, while crawling leads to overestimation. As the piercing of bubbles by a fiber-optic microprobe is a random process in complex three-dimensional two-phase flow, it is difficult to quantify these uncertainties. However, at high signal-to-noise ratios, even partially pierced bubbles or bubbles brushing the probe tip usually result in usable signals. Quantities derived from Eq. (3.5) are therefore not particularly sensitive to the choice of U_{th} as long as it is set to a value high enough above the noise of the raw signal. This is shown in Fig. 3.11 for an experiment with a single-fiber microprobe. In this figure, the calculated void fraction is displayed over the threshold voltage normalized to the maximum voltage U_{max} of the recorded signal. There exists a broad range for U_{th}, for which the calculated void fraction does not change significantly.
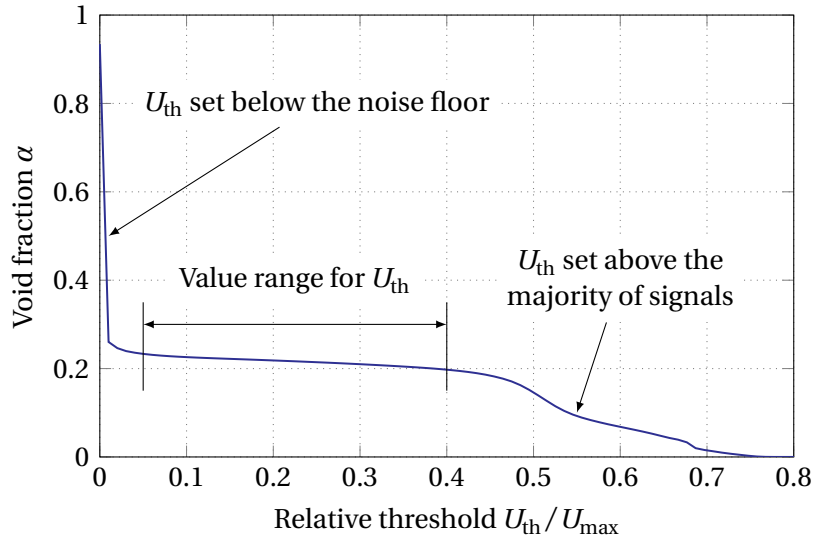
Figure 3.11: Change in calculated void fraction from fiber-optic microprobe data for a variation of the threshold voltage.

The velocity measurements from the double-fiber microprobes were compared to bubble velocities obtained by stereoscopic videometry for two-phase flow with single bubbles. A deviation of less than ±15 % was observed between the two measurement techniques. However, the only well-defined parameter in this context is the interface velocity of single bubbles. This quantity is not directly related to the actual void velocity [175]. As described by Garnier et al. [20], the true velocity of the void phase can only be related to the distance between the two fibers of a double-fiber microprobe if the velocity and size distributions are spatially uniform where the void is intercepted by the two fibers. The mean void velocity can then be derived from a double-fiber microprobe setup when being calculated over a sufficiently large number of void structures and assuming that void velocity does not depend on ligament diameter. This was verified in videometric reference experiments. In these experiments, mass flux was kept constant at $1000\,\mathrm{kg\,m^{-2}\,s^{-1}}$ and two different subcoolings were investigated. Velocity profiles from the double-fiber microprobe setup were compared to high-speed videometry measurements. The data from double-fiber microprobe experiments was evaluated for a time interval of $0.5\,\mathrm{s}$ to match the acquisition frequency of temperature data of $2\,\mathrm{Hz}$. The number of detected void ligaments during this interval was in the order of $N_{\mathrm{lig}} = 200 - 500$. The bulk flow velocity for these conditions is approximately $0.66\,\mathrm{m\,s^{-1}}$. Videometric measurements near the heater surface were not possible due to high vapor concentration. Measurements

with the double-fiber microprobes were inhibited in regions of low void fraction due to the small number of detected bubbles. The results are shown in Fig. 3.12. Both measurement techniques show good agreement in the region where they overlap with a maximum deviation of approximately 10 %. The more conservative uncertainty from the single-bubble experiments of ±15 % for the average ligament velocity is chosen for this study. The uncertainties of quantities presented in this dissertation are summarized in Table 3.2.
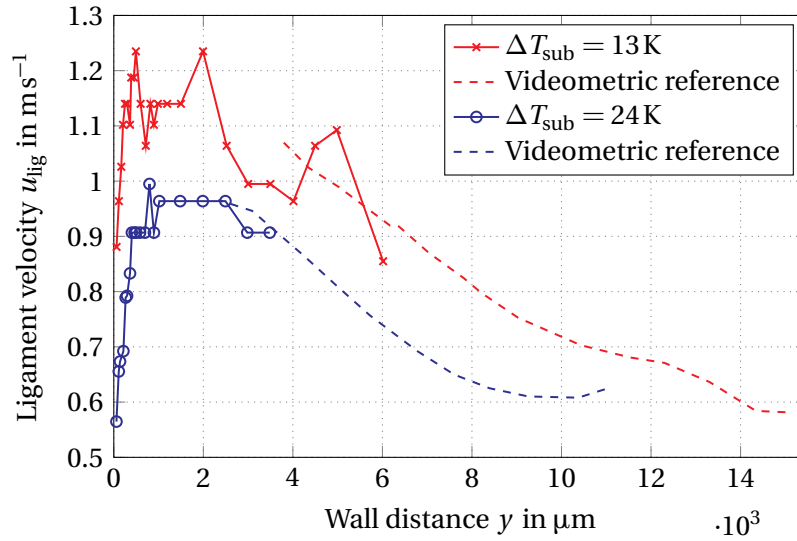
Figure 3.12: Comparison between the void velocity obtained through videometric reference experiments and the data from double-fiber microprobes for two subcoolings. Mass flux was kept constant at $G = 1000 \, \text{kg} \, \text{m}^{-2} \, \text{s}^{-1}$.

Table 3.2: Overview of uncertainties of measured quantities.

Quantity	Uncertainty	Unit
Void data from PIF	± 2.5	%
Ligament velocity/ size	± 15.0	%
Position of void probes	± 5	µm
Heat flux	± 10.7	$\text{kW} \, \text{m}^{-2}$
Wall temperature	± 0.9	K
Mass flux	± 20	$\text{kg} \, \text{m}^{-2} \, \text{s}^{-1}$
Subcooling	± 0.2	K

3.5 Measurement Procedure

To ensure consistent surface properties, the boiling surface of each heater configuration was cleaned and polished using a 2500-grit emery paper after each fourth experiment. The first run after this procedure was discarded to eliminate the effects of non-condensables. This way, a good repeatability of the experimental data was achieved [4]. It was previously shown in [8] that the wall-mounted copper heater behaves quasi-statically. Therefore, a full boiling curve from single-phase convection to fully-developed film boiling was recorded for each fiber-optic microprobe position and operating condition for the wall-mounted copper heater. The thermal stability limit of the fluid prohibited measurements beyond CHF for the single-rod copper-coated stainless steel heater because of the fast increase of the heater temperature at CHF due to its small thermal inertia. The experimental procedure for each experiment and heater configuration was as follows:

1. The heater is at or close to ambient conditions. Fluid is circulated through the system. No boiling activity is present on the heater surface.

2. The system is heated up to the chosen subcooling.

3. After reaching this subcooling, the fiber-optic microprobes are positioned at the target distance of $100\,\mu m$ above the boiling surface at the positions of the thermocouple rows and thermocouples respectively. The positioning accuracy of the traversing mechanism is verified optically before each experiment.

4. Measurement data is acquired for the two heater configurations as follows:

   - **Wall-mounted copper heater**: The transformer powering the heater cartridges is switched on simultaneously with the start of data acquisition. The power supplied to the heater cartridges was kept constant for all measurements. The system goes through one complete boiling cycle from single-phase convection to fully-developed film boiling. The transformer is switched off when the Leidenfrost point is reached and surface heat flux begins to increase again. Data acquisition is stopped.

- **Single-rod copper-coated stainless steel heater**: The transformer powering the heating coil is set to the desired operating point of the heater. The transformer is switched on. The data acquisition is started when a steady state is reached. Data is acquired for 60 s per operating point. The transformer is switched off and data acquisition is stopped when either 60 s have passed or one of the thermocouples fitted to the heater detects the occurrence of CHF as a fast increase in surface temperature.

5. The system is cooled down until the initial conditions are reached.

Chapter 4

Results and Discussion

In this chapter, the experimental results are presented and discussed. First, the experimental data from experiments with the wall-mounted copper heater are presented for one set of operating conditions. Second, the experimental data from experiments at the same operating conditions are presented for the single-rod copper-coated stainless steel heater. Third, the data is analyzed and discussed in detail. The analysis is split into two parts. First, the mechanistic models introduced in Sec. 2.4.2 and Sec. 2.4.4 are discussed with respect to the experimental data. Second, the data from the two heater configurations is compared with each other and analyzed in more detail. In this analysis, the governing parameters for the boiling process in the nucleate boiling regime are identified and a refined mechanism for the CHF process at the wall in flow boiling is proposed. The analysis is supported by additional experimental results from measurements at different operating conditions for both heater geometries. Concluding this chapter, a stability limit for the boiling process is identified based on the experimental data.

4.1 Wall-Mounted Copper Heater

In this section, average boiling curves, void data profiles and time-resolved void data in the immediate vicinity of the boiling surface are presented for the three measurement positions along the direction of flow. Data was obtained from experiments with a mass flux of $G = 1000\,\mathrm{kg\,m^{-2}\,s^{-1}}$, which corresponds to a superficial liquid flow velocity of $u_\mathrm{l} = 0.66\,\mathrm{m\,s^{-1}}$. Inlet subcooling was kept constant at $\Delta T_\mathrm{sub} = 13\,\mathrm{K}$. Void profiles are provided for three characteristic states along the boiling curve, which are fully-developed boiling (FDB), CHF and fully-developed film boiling (FDFB). The respective definitions as a function of wall superheat $\Delta T_\mathrm{sup} = T_\mathrm{w} - T_\mathrm{sat}$ are given in Tab. 4.1. A

wall superheat at FDB of $\Delta T_{\text{sup,FDB}} = 75\,\%\,\Delta T_{\text{sup,CHF}}$ was chosen based on experiments conducted prior to the present study. This value ensures that FDB lies in the fully-developed nucleate boiling regime as illustrated in Fig. 2.1. Corresponding to previous work [77], CHF is defined as the maximum surface heat flux observed in the experiments. For each experiment, the time of maximum heat flux is determined for each thermocouple row. Heat flux, wall temperature and void data at CHF are then extracted using the obtained time stamp. The values at FDB and FDFB are then obtained using the respective wall temperature and the corresponding time stamp relative to CHF. Boiling curves and void profiles for other operating conditions are documented in Appendix B and Appendix C.

Table 4.1: Definition of points along the boiling curve for which void data profiles are presented.

Point	Definition
FDB	$\Delta T_{\text{sup,FDB}} = 75\,\%\,\Delta T_{\text{sup,CHF}}$
CHF	$\Delta T_{\text{sup,CHF}} = \Delta T_{\text{sup}}$ at $\dot{q} = \dot{q}_{\text{max}}$
FDFB	$\dot{q} = \dot{q}_{\text{min}}$ at $\Delta T_{\text{sup,FDFB}} > \Delta T_{\text{sup,CHF}}$

4.1.1 Boiling Curves

Fig. 4.1 shows boiling curves averaged over all experiments for this set of operating conditions. The heat flux at CHF is highest for the upper measurement position at $\dot{q} = 269.6\,\text{kW}\,\text{m}^{-2}$ at a wall superheat of $\Delta T_{\text{sup,CHF}} = 38\,\text{K}$. CHF occurred at the same wall superheat at all measurement positions. The heat flux at CHF is marginally lower for the middle and lower measurement position at $259.3\,\text{kW}\,\text{m}^{-2}$ and $244.0\,\text{kW}\,\text{m}^{-2}$. To check whether the data from different measurement runs is consistent, confidence intervals for the measurement series were calculated according to Eq. (4.1). In this equation $\bar{x}$ is the average value, $u_{1-\frac{\epsilon}{2}}$ the expected value in the $1-\frac{\epsilon}{2}$ quantile, σ the standard deviation and n is the total number of measurements [176]. In this study, $\epsilon = 0.2$ was chosen and $n = 29$.

$$\left[\bar{x} - u_{1-\frac{\epsilon}{2}} \frac{\sigma}{\sqrt{n}} \, ; \bar{x} + u_{1-\frac{\epsilon}{2}} \frac{\sigma}{\sqrt{n}} \right] \tag{4.1}$$

Only little variance between individual experiments is observed for single-phase convection and the nucleate boiling regime up to CHF for all measurement positions along the direction of flow. During transition boiling after CHF, the confidence region widens significantly. At the Leidenfrost point, confidence intervals converge again. The variance between measurements at the upper position during the transition to film boiling is higher than for the middle and lower position. Visual observation of the CHF transient showed that the CHF mechanism occurred first between the lower and middle measurement position. For the operating conditions of $G = 1000 \, \mathrm{kg \, m^{-2} \, s^{-1}}$ and $\Delta T_{\mathrm{sub}} = 13 \, \mathrm{K}$, CHF was first detected predominantly at the lower position. This explains the greater variance for the upper measurement position as the forming vapor film did not propagate along the heater at a constant speed for each experiment. All points defined in Tab. 4.1 lie in regions with only very little variance.
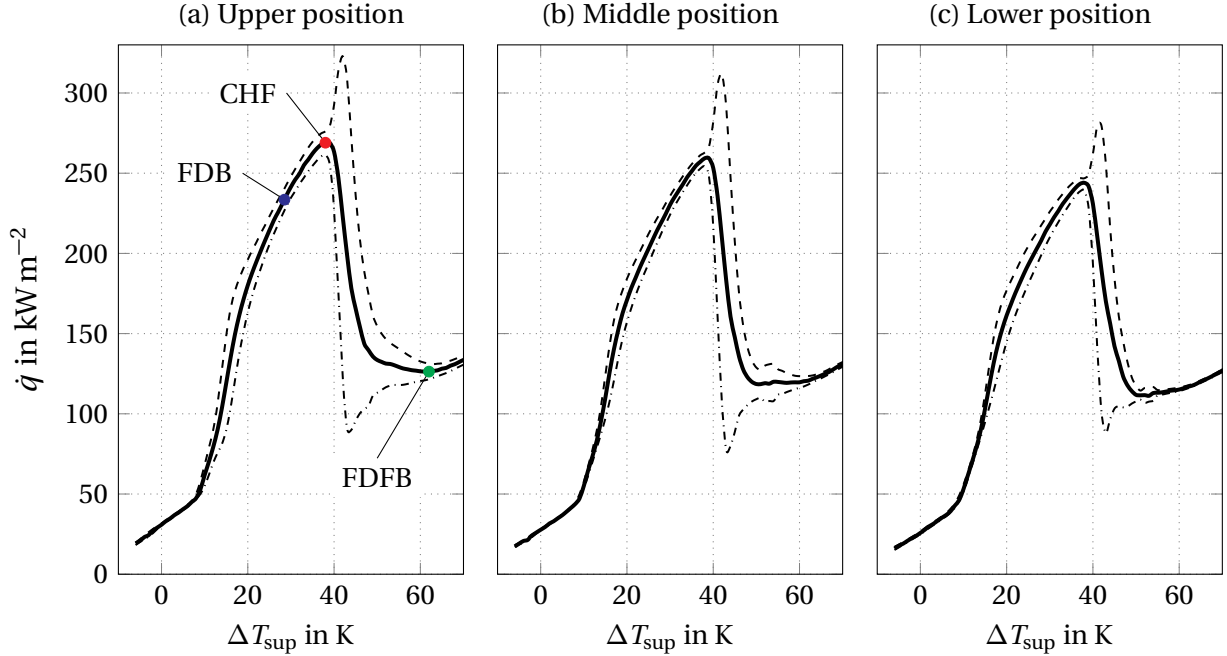
Figure 4.1: Average boiling curves at the upper, middle and lower measurement position for the wall-mounted copper heater. Dashed and dashed-dotted lines represent the upper and lower confidence intervals. Color-coded dots represent the points from Tab. 4.1 for which void profiles are provided.

4.1.2 Void Profiles

Fig. 4.2 and Fig. 4.3 show profiles for void fraction, void frequency, ligament velocity and ligament size for FDB, CHF and FDFB at the upper, middle and lower measurement position.

4.1.2.1 Void Fraction

General observations: The void fraction profiles for FDB and CHF match the behavior described by Drew and Lahey [177]. They report a peak in void fraction close to the wall followed by a reciprocal decline towards the center of the flow channel for adiabatic upward low-quality bubbly flow. Void fraction in this study slightly increases from its value closest to the wall until $y \approx 300\,\mu\text{m}$, before decreasing continuously towards the center of the flow channel. The peak in void fraction is most clearly seen at the lower measurement position. Peak values for α range between 66 % and 73 %. The highest absolute values were measured at the lowest position. Near-wall void in the layer $y \leq 1\,\text{mm}$ above the heater surface decreases slightly along the direction of flow. This could possibly be attributed to the presence of vapor-induced secondary flows, which facilitate the replenishment of the sublayer with fresh bulk liquid and increase recondensation rates at the upper measurement position. For FC-72, Jung et al. [25] report that approximately 90 % of heat transfer at critical heat flux can be attributed to the liquid phase present at the wall. This partly explains the higher values for critical heat flux at the upper measurement position where the lowest void fraction close to the wall was measured. The relative increase in critical heat flux from $\dot{q} = 244.0\,\text{kW}\,\text{m}^{-2}$ at the lower to $\dot{q} = 269.6\,\text{kW}\,\text{m}^{-2}$ at the upper measurement position is 10.6 %. The measured relative reduction of the maximum void fraction observed in the immediate vicinity of the heater surface between the lower and the upper measurement position is equal to the relative increase in critical heat flux.

From FDB to CHF: Between FDB and CHF, void fraction slightly increases close to the wall at the upper measurement position, whereas no significant increase in void was measured at the middle and lower position. For $y \geq 1\,\text{mm}$, no difference in void fraction between FDB and CHF was observed.

Upper position $z = 154\,\text{mm}$

Middle position $z = 84\,\text{mm}$

Lower position $z = 34\,\text{mm}$
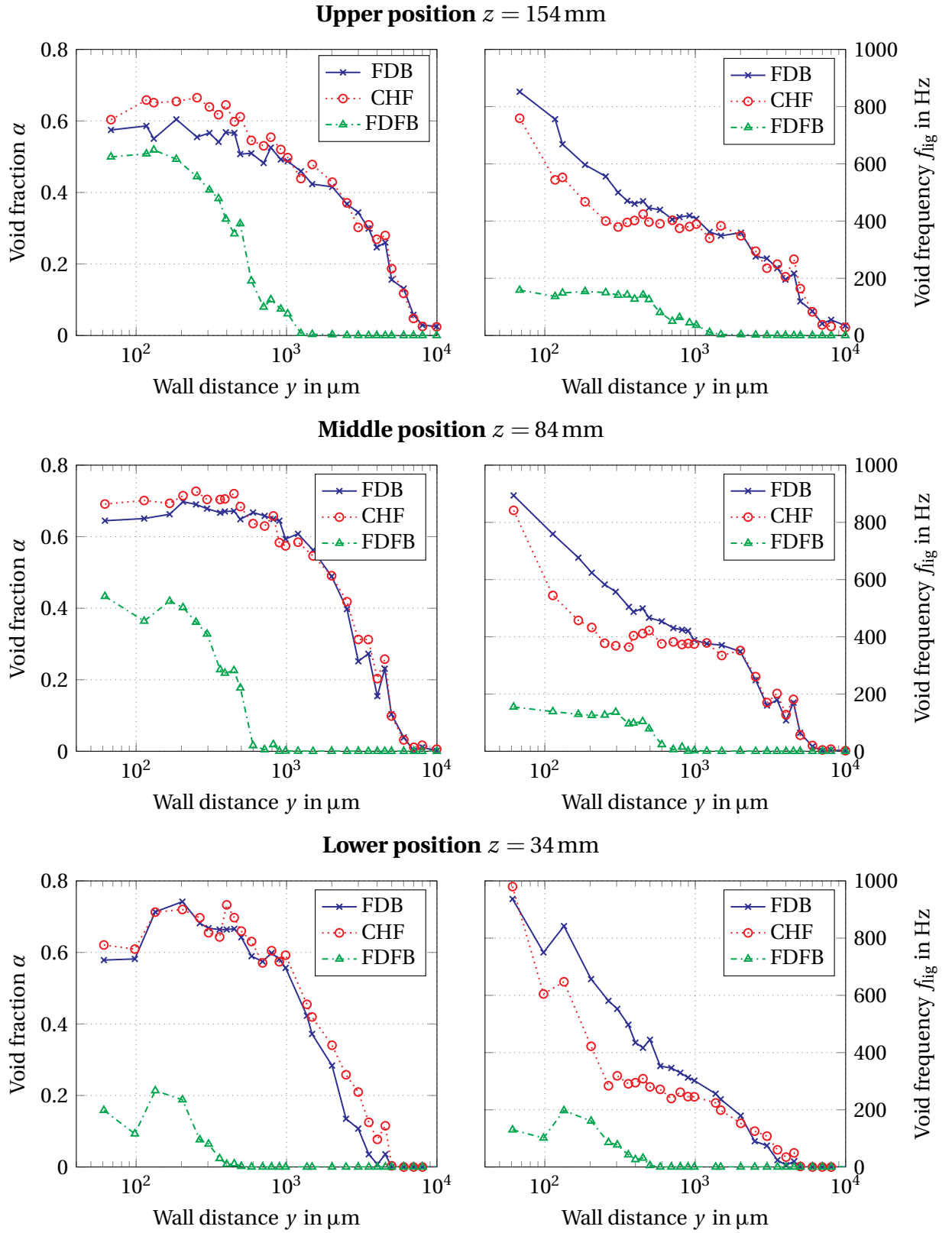
Figure 4.2: Lin-log plots of void fraction (left) and frequency (right) profiles at FDB, CHF and FDFB obtained from fiber-optic microprobe measurements at the upper, middle and lower measurement position.
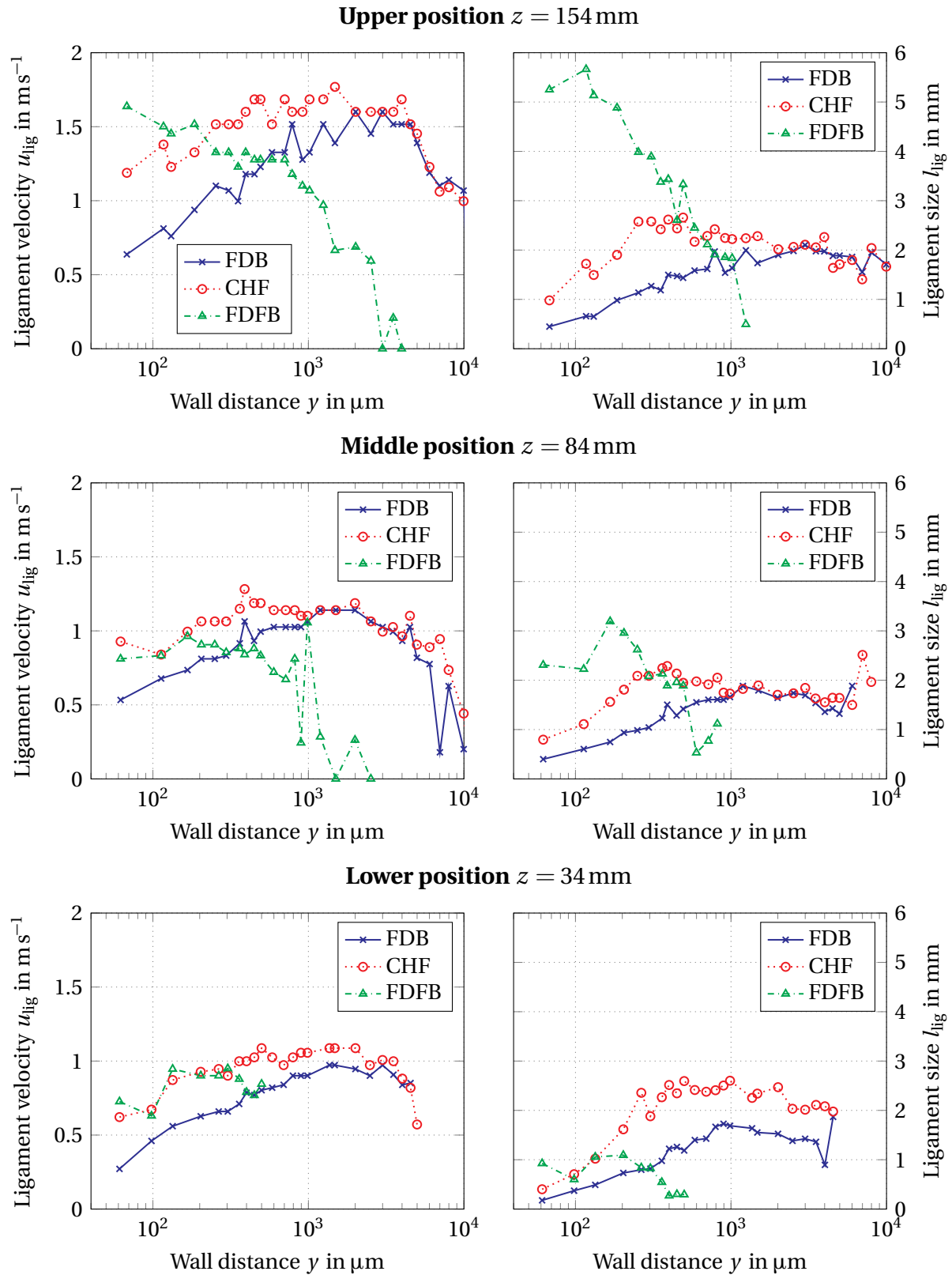
Figure 4.3: Lin-log plots of ligament velocity (left) and ligament size (right) profiles at FDB, CHF and FDFB obtained from fiber-optic microprobe measurements at the upper, middle and lower measurement position.

CHF predominantly occurred at some point between the lower and middle measurement position. Only a marginal change in void fraction between FDB and CHF was measured at these two positions. Based on this observation, two conclusions can be drawn. First, the amount of void present in the vicinity of the heater surface influences the maximum attainable value of surface heat flux by limiting the supply of fresh bulk liquid to the heater. Second however, absolute near-wall void is not the causative limiting factor of the boiling process at the wall. Theofanous et al. [26, 27] observed that the occurrence of CHF is independent of void fraction above the heater surface for pool boiling. The current results indicate that their findings may hold true for subcooled flow boiling.

At FDFB: At FDFB measured void fractions are significantly lower compared to CHF, even at a distance of $y = 50\,\mu$m from the heater surface. Values measured at FDFB at this distance increase along the direction of flow but do not exceed 50 % at the upper measurement position. Void fraction in the film is expected to be close to 100 %. Hence, this experiment indicates a film thickness of less than $50\,\mu$m.

4.1.2.2 Void Frequency

General observations: The void frequency f_{lig} continuously increases towards the heater wall for FDB and CHF at all three measurement positions. The highest frequencies were measured closest to the wall at $y = 50\,\mu$m with a peak frequency of up to $f_{\text{lig}} = 1000\,$Hz at the lower measurement position. For FDB, an exponential increase towards the wall is observed for a layer of $y \leq 2\,$mm above the heater surface. At CHF, the point of this increase of frequency shifts towards the wall to $y \approx 300\,\mu$m. This distance corresponds with the point of peak values of α in each void fraction profile at CHF. Above this distance f_{lig} remains almost constant until $y \approx 1\,$mm. These findings confirm the existence of a relevant bubbly sublayer as previously postulated in [10]. In this layer the frequency of detected void ligaments is a lot bigger compared to the bulk flow. For the thermal and hydraulic conditions of the data presented here, the relevant bubbly sublayer is approximately $300\,\mu$m thick.

From FDB to CHF: Void frequencies at CHF are generally lower compared to FDB. The boiling process becomes less intermittent approaching CHF. This suggests a deactivation mechanism from FDB to CHF induced by larger coalesced void structures on or close to the heater surface.

At FDFB: Once the transition to film boiling has completed, void frequencies close to the heater surface at FDFB are approximately one order of magnitude smaller compared to FDB and CHF.

4.1.2.3 Ligament Velocity

General observations: For both FDB and CHF, a steep velocity gradient is observed close to the wall. At FDB, the velocity profile flattens at $y \approx 1.1\,\text{mm}$ from the wall. At CHF, this point shifts towards the wall to a distance of $y \approx 500\,\mu\text{m}$.

From FDB to CHF: Between FDB and CHF, void ligaments are accelerated significantly in the region close to the wall. For all measurement positions along the direction of flow, a nearly twofold increase in velocity is observed in the immediate vicinity of the heater surface. The acceleration of void between FDB and CHF points at a fundamental change in flow topology close to the wall when approaching CHF. This effect can only be partly attributed to increased buoyancy as the relative increase of void fraction in this layer during the same period is much smaller. It is possible that a superposition of several phenomena is seen here. It was shown in previous studies that close to CHF large vapor plumes periodically propagate along the heater [8, 10]. By means of particle image velocimetry, it was observed that void in the wake of these plumes was pulled towards the heater with a relative increase in velocity of up to 33 %. Moreover, more vigorous boiling was observed close to CHF. Both of these effects could lead to higher average interface velocities in the vicinity of the heater. Jung et al. [25] measured the speed of the triple-phase contact line on a heater surface for pool boiling by means of high-speed infrared imaging. The authors report a decreasing contact line speed close to CHF. The current data suggests an opposite trend for flow boiling. As seen on

the right-hand side of Fig. 4.3, at $y = 50\,\mu$m data is obtained at a wall distance much smaller than the characteristic ligament size of $l_{\mathrm{lig}} \approx 0.4\,$mm. It is therefore assumed that the ligament velocity measured at $y = 50\,\mu$m in the present study is connected to the triple-phase contact line speed on the heater surface.

At FDFB: At FDFB, the velocity profile close to the wall is flatter compared to CHF and FDB at the lower and middle measurement position and it is inverted compared to FDB and CHF at the upper measurement position. In the nucleate boiling regime up to CHF there exists a shear lift force F facilitating the departure of bubbles from the heater surface, because of the velocity gradient present at the wall [178, 179]. From CHF to FDFB, this force gradually becomes weaker as the velocity gradient becomes smaller and eventually changes direction due to the acceleration of void structures close to the wall.

4.1.2.4 Ligament Size

General observations: For FDB and CHF, ligament sizes at the wall are small but they quickly grow in size with increasing wall distance. At CHF, ligament sizes peak near the relevant bubbly sublayer discussed above and slightly decrease beyond this distance. No significant difference regarding the size of void ligaments in the bulk flow at CHF was observed between the three measurement positions along the direction of flow.

From FDB to CHF: Ligament sizes show a twofold increase close to the wall between FDB and CHF for all three measurement positions along the direction of flow. Larger void structures cover the heater surface. In view of the noticeable decrease in void intermittency at CHF, the temporary deactivation of active nucleation sites seems probable. Both, the continuous deactivation by overlapping void from neighboring nucleation sites as well as the formation of residual dry-patches on the heater surface, as observed for example by Chu et al. [111] for pool boiling, appear viable.

At FDFB: At FDFB, the heater is fully covered by a gaseous film. Visual observation of the fully-developed vapor film showed wavy void structures propagating along the film in the direction of flow. According to the fiber-optic microprobe data, these void structures are significantly bigger in size compared to the void ligaments observed in the nucleate boiling regime. Similar observations were reported in other studies [96, 99].

4.1.3 Void Morphology Near the Boiling Surface

Fig. 4.4 shows time-resolved data obtained from a double-fiber microprobe experiment. One complete boiling cycle was recorded from single-phase convection to fully-developed film boiling. The probes were positioned at a distance of $y = 100\,\mu$m from the wall. This distance was chosen as a compromise between obtaining data in the immediate vicinity of the heated wall and reducing the possible influence of the double-fiber microprobes on the boiling process at closer distances. Data is displayed normalized to the time of the occurrence of CHF ($t_{\mathrm{CHF}} = 0\,$s) for each measurement position along the direction of flow. Effective heat transfer coefficients (HTC) h_{eff} were calculated according to Eq. (4.2), to see how overall heat transfer over the boiling surface changes over time.

$$h_{\mathrm{eff}} = \frac{\dot{q}}{T_{\mathrm{w}} - T_{\mathrm{sat}}} \tag{4.2}$$

4.1.3.1 The Nucleate Boiling Regime

The measured void fraction quickly increases as nucleation sites are activated on the heater surface at the onset of nucleate boiling at $t \approx -75\,$s. After the initial rise, the void fraction continues to grow approximately linearly. Void frequencies rapidly increase and show a distinct peak after which they begin to decline. The point of peak frequency coincides with the maximum of the effective HTC which henceforth declines. Ligament sizes at peak frequency are similar for all three measurement positions along the direction of flow at 0.37 mm, 0.34 mm and 0.40 mm. This suggests a maximum attainable size for
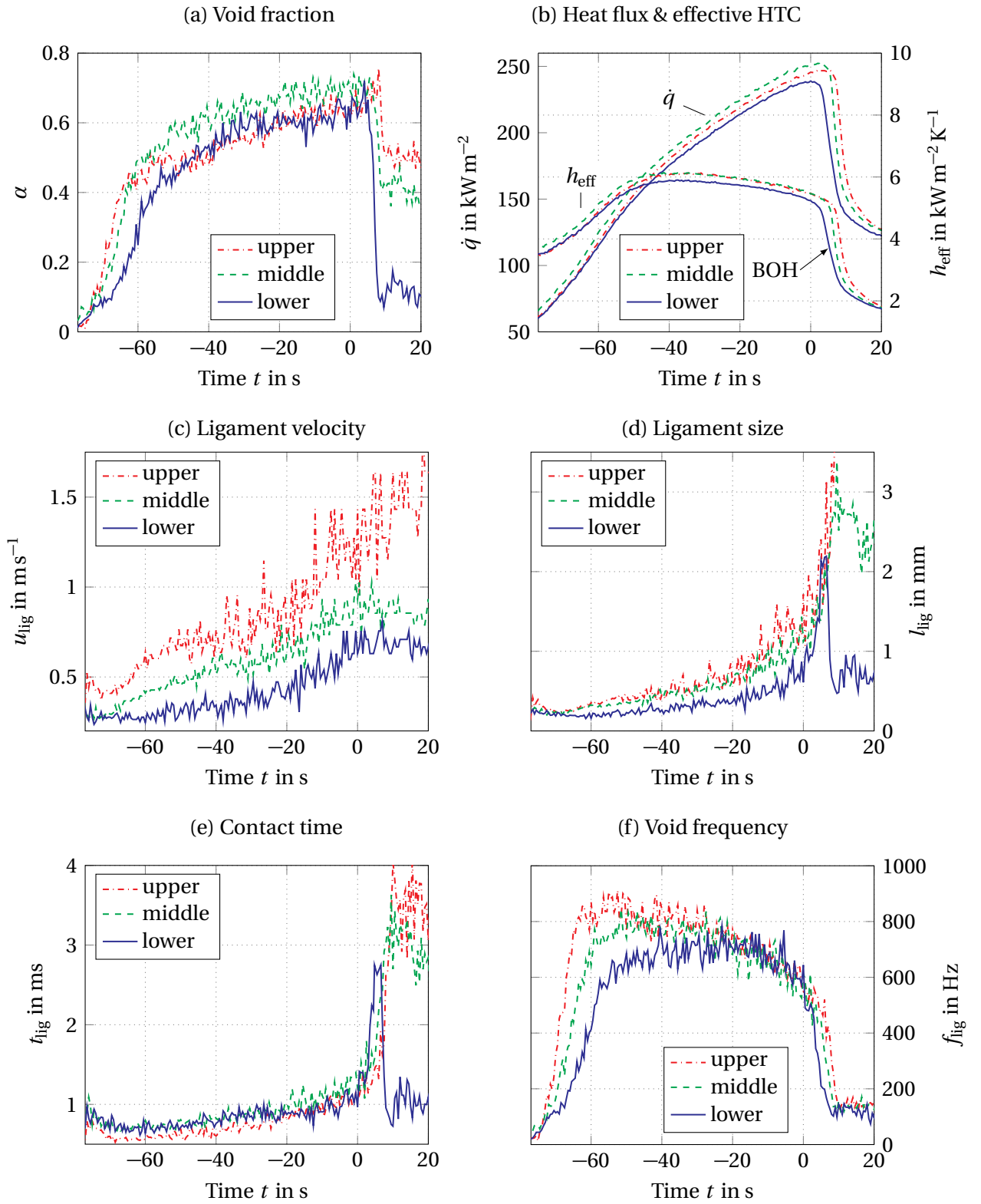
Figure 4.4: Time-resolved void data from a double-fiber microprobe experiment at a distance of $y = 100\,\mu m$ away from the heated surface of the wall-mounted copper heater. $t = 0\,s$ is the time of CHF at each measurement position.

void structures on the heater surface before neighboring nucleation sites are influenced by overlapping. The size of void structures increases with increasing heat flux. Void intermittency in the vicinity of the heater decreases, which results in lower heat transfer through the agitation of the single-phase liquid on the heater surface. Following the findings of Jung et al. [25], this reduces the effective HTC.

4.1.3.2   Approaching CHF

During the nucleate boiling regime before $t \approx -20\,$s, the ligament velocity, the ligament size and the contact time show a weak linear increase. At $t = -20\,$s the morphology of void begins to change. Void ligaments are accelerated and contact times begin to rise faster. Ligament sizes increase at the heater surface. From $t = -20\,$s to CHF, the average ligament size at all measurement positions increases by 200 %. Immediately before CHF at $t = 0\,$s, the onset of an exponential rise of contact time and consequently ligament size is seen. At the same time, void frequencies begin to decrease rapidly. A smaller number of bigger void structures gradually covers the heater surface. Despite their decrease, void frequencies remain high at over 600 Hz. Significant nucleation site activity persists during this phase. Absolute void fraction values continue to increase linearly. Within the margin of uncertainty, void frequencies and contact times at the wall are uniform along the direction of flow up to CHF. Contact times at this distance to the wall can be interpreted as the average local dry time of the heater surface per void structure.

4.1.3.3   The Transition to Film Boiling

After reaching a value of approximately $t_{\mathrm{lig}} = 1.2\,$ms, dry times and ligament sizes show a sudden exponential increase. Void frequencies drop. A distinct peak in void fraction after CHF is observed at all measurement positions along the direction of flow. The relative increase between the void fraction at CHF at $t = 0\,$s and the maximum void fraction value after CHF is up to 19 % at the lower measurement position. A similar relative increase in area-averaged wall void fraction has been reported for pool boiling in [29, 113]. Within 10 s after CHF, the effective HTC h_{eff} decreases to half of its value right before CHF.

The peak in void fraction and the highest values of ligament size and dry time coincide with the maximum rate of decrease of heat flux and effective HTC. In the following, this point is denoted as breakdown of heat transfer (BOH). These findings suggest that a maximum dry time exists, which can be sustained for this combination of fluid, surface and thermo-hydraulic operating parameters. Once this value has been reached, less heat is removed through the boiling process than is provided by the heater. The following temperature rise leads to rapidly growing void structures that spread over the heater surface, deactivating a large share of active nucleation sites. This feedback process eventually leads to the gradual breakdown of nucleate boiling and marks the beginning of transition boiling.

4.1.3.4 Acceleration of the Void Phase

Another aspect which appears to have gotten too little attention in the discussion of the CHF mechanism yet is the acceleration of the vapor phase in the sublayer close to the wall. As shown experimentally by Tomiyama et al. [178] and numerically by Bothe et al. [179], bubbles beyond a critical diameter in a shear flow are influenced by a lift force, which acts in the direction of the higher surrounding velocities. Up to CHF, the void phase is therefore pulled away from the wall, due to the steep velocity gradient of the void phase in the vicinity of the heater. This is evidenced in Fig. 4.3 for FDB and CHF for all measurement positions along the direction of flow. In the same figure, it can be seen that the velocity gradient and hence the shear lift force acting on the void structures has inverted at FDFB.

Fig. 4.5 shows the ligament velocity for two different distances from the wall at the middle measurement position. Approaching CHF, the void phase at $y = 62\,\mu$m away from the wall is accelerated much faster compared to $y = 362\,\mu$m. At $t \approx 4\,$s, the velocities at both distances are equal. The lift force normal to the heater surface gradually becomes weaker as CHF is approached and disappears at BOH. Arguing that this lift force plays an important role, bubble departure will be increasingly inhibited by the gradient reversal. Assuming that the reverting shear lift force on the void phase close to the wall is one of the driving factors for the transition to film boiling, BOH resembles

the »point of no return« between CHF and FDFB where the formation of a film can no longer be avoided.
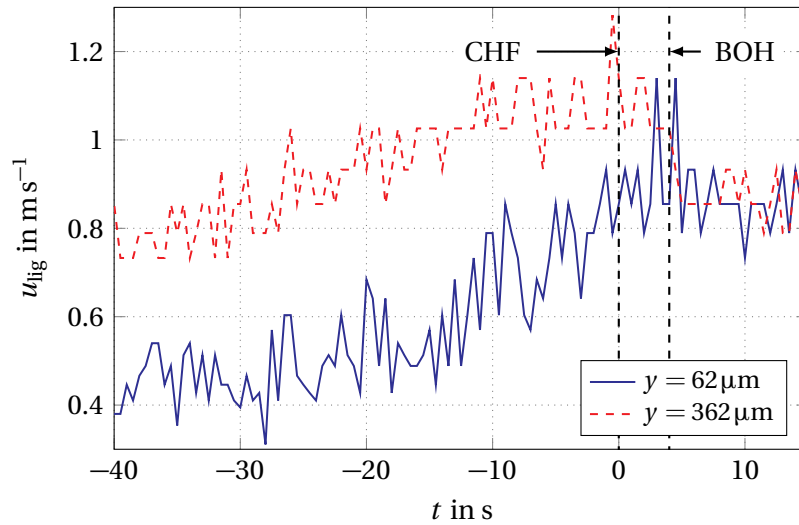
Figure 4.5: Evolution of ligament velocity during the CHF transient at two different distances from the wall at the middle measurement position of the wall-mounted copper heater.

4.2   Single-Rod Copper-Coated Stainless Steel Heater

In this section, data of surface heat flux and wall temperature, void profiles, void data along the boiling curve and time-resolved void data in the immediate vicinity of the boiling surface during the CHF transient are presented for the single-rod copper-coated stainless steel heater. Corresponding to the data of the wall-mounted copper heater, mass flux was $G = 1000\,\mathrm{kg\,m^{-2}\,s^{-1}}$ and subcooling was $\Delta T_{\mathrm{sub}} = 13\,\mathrm{K}$.

4.2.1   Boiling Curve

Fig. 4.6 shows the average surface heat flux of the singe-rod copper-coated stainless steel heater plotted over the wall superheat measured at the middle thermocouple. As for the wall-mounted copper heater, CHF occurred first at the upstream end of the heater between thermocouple positions TC 2 and

TC 3 and was first detected primarily at the middle measurement position TC 2. A possible reason for this behavior are heat losses at the upstream and downstream end of the heated area, which could not be avoided. Due to the rapid local increase of heater temperature of over $150\,\mathrm{K\,s^{-1}}$ at CHF, the power supply to the heater was switched off before the vapor film was able to cover the entire heated surface. This was done to protect the heater from excessive temperatures and to stay below the thermal stability limit of the fluid. Therefore, all subsequent data for this configuration is shown with respect to the wall superheat at the middle measurement position. The measured critical heat flux of $148.1\,\mathrm{kW\,m^{-2}}$ at a wall superheat of $26.7\,\mathrm{K}$ is significantly lower compared to the wall-mounted copper heater.
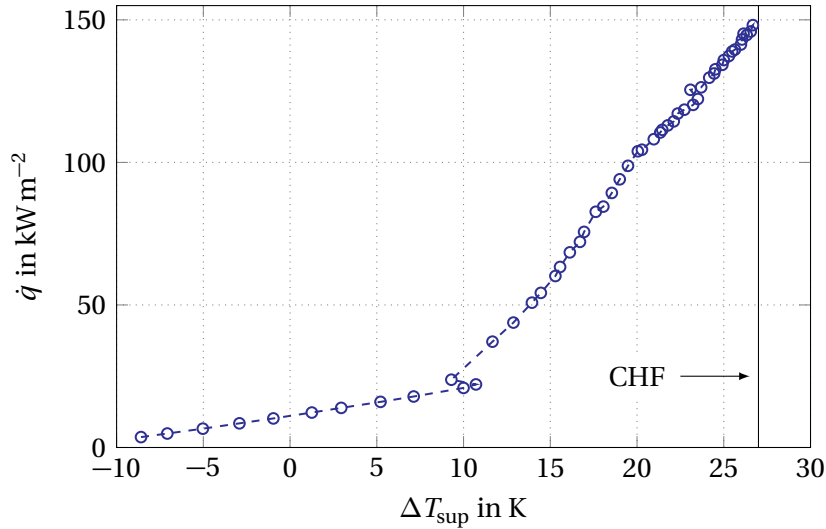
Figure 4.6: Boiling curve of the single-rod copper-coated stainless steel heater for a mass flux of $G = 1000\,\mathrm{kg\,m^{-2}\,s^{-1}}$ and a subcooling $\Delta T_{\mathrm{sub}} = 13\,\mathrm{K}$.

4.2.2 Void Profiles

For the single-rod copper-coated stainless steel heater, profiles for void fraction, void frequency, void ligament velocity and void ligament size were obtained above the middle measurement position for FDB and CHF. They are shown in Fig. 4.7. Measurements at fully-developed film boiling were not possible, due to the rapid increase in heater temperature beyond CHF.

Void fraction: Void fraction shows a distinct peak close to the wall at approximately $y = 150\,\mu$m. Between this peak and the measurement position closest to the boiling surface, void fraction decreases by 6 % - 11 %. Void fraction in the entire cross section increases between FDB and CHF. The relative increase is much larger compared to the wall-mounted copper heater. At CHF, the values of void fraction close to the wall are approximately of the same magnitude between the two heater configurations.
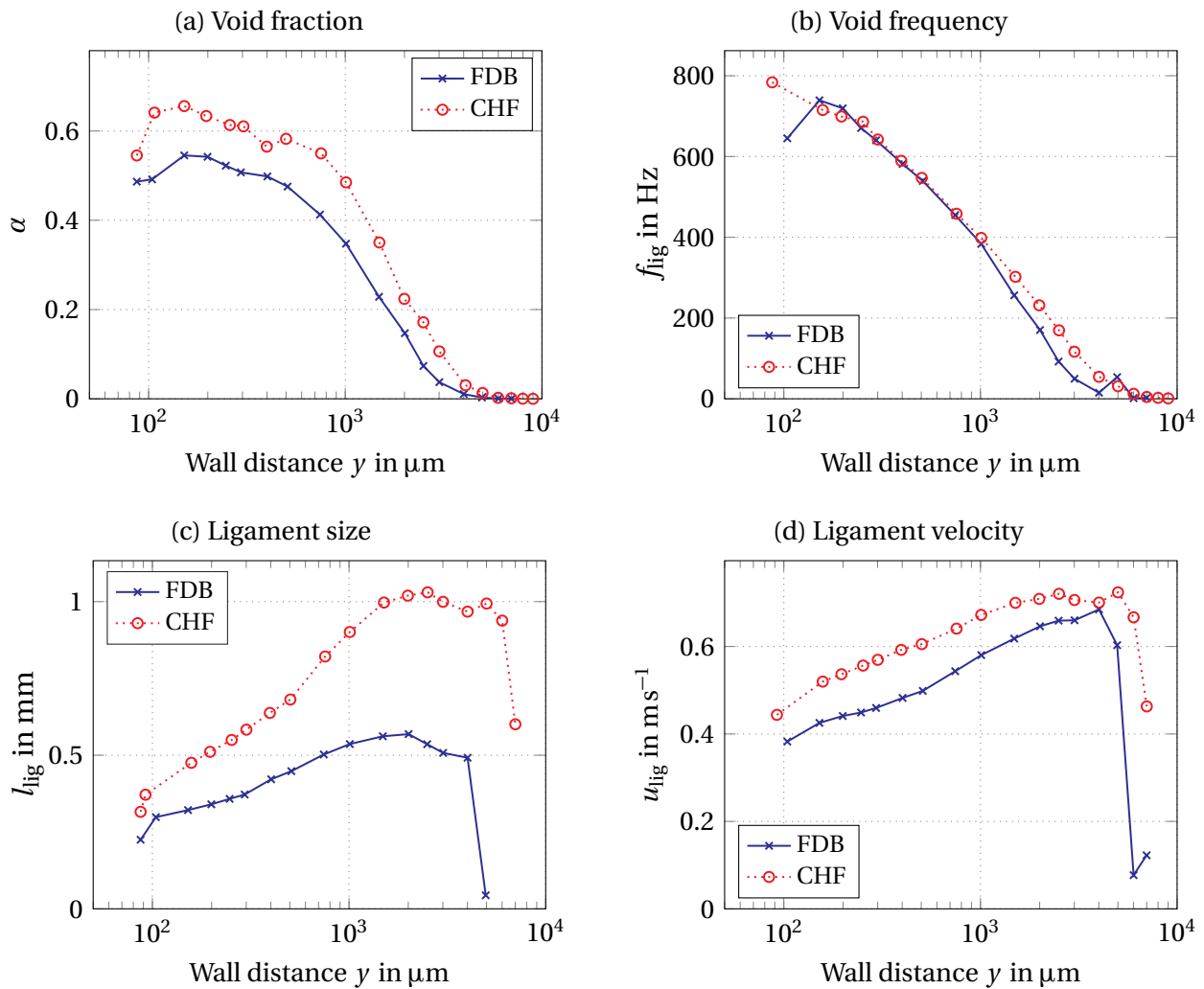
Figure 4.7: Void profiles at the middle measurement position of the single-rod copper-coated stainless steel heater for $G = 1000\,\mathrm{kg\,m^{-2}\,s^{-1}}$ and $\Delta T_{\mathrm{sub}} = 13\,\mathrm{K}$.

Void frequency: The void frequency only marginally increases between FDB and CHF in the bulk flow. In contrast to the observations with the wall-

mounted copper heater, an increase in void frequency between FDB and CHF occurs at the measurement position closest to the boiling surface. At a wall distance of 50 μm, the absolute value of void frequencies of approximately 800 Hz at CHF is similar for the two heater configurations. In a layer of $y \approx 100\,\mu m - 300\,\mu m$ above the heater surface, void frequencies at CHF are approximately the same. This homogeneous layer above the heater surface is much smaller compared to the wall-mounted copper heater. Below 100 μm, the void frequency increases towards the wall. This increase is significantly less distinct compared to the wall-mounted copper heater.

Ligament size: Void ligament sizes are smallest closest to the boiling surface. They quickly increase in size towards the flow channel. The size of void structures for the single-rod copper-coated stainless steel heater does not exceed 1 mm, which is significantly lower compared to the wall-mounted copper heater. Between FDB and CHF, void ligaments show a twofold increase in size for all measurement distances in wall-normal direction. This relative increase between FDB and CHF was also observed for the wall-mounted copper heater.

Ligament velocity: The velocity of void ligaments increases along the entire cross section between FDB and CHF. Absolute velocities are significantly lower compared to the wall-mounted copper heater. For both FDB and CHF, the velocity profile flattens at $y \approx 1.5\,mm$ and reaches its maximum at approximately $y = 4\,mm$.

4.2.3 Void Morphology Near the Boiling Surface

4.2.3.1 Behavior Along the Boiling Curve

Fig. 4.8 shows the void data along the boiling curve obtained by double-fiber microprobe measurements at a wall distance of 100 μm at the middle measurement position. At the onset of boiling, the void fraction quickly increases. Similar to the wall-mounted copper heater, void frequency quickly increases as more nucleation sites are activated with increasing wall superheat. Like for

the wall-mounted copper heater, the void frequency exhibits a distinct maximum in the fully-developed boiling regime at a wall superheat of $\Delta T_{\text{sup}} \approx$ 20 K. After reaching this maximum, void frequencies decline continuously towards critical heat flux with increasing wall superheat. Void ligament sizes increase with increasing wall superheat. At the maximum void frequency, an average void ligament size of approximately 0.3 mm was measured. This value is only marginally lower compared to the value at peak frequency of the wall-mounted copper heater and supports the idea of a maximum attainable bubble diameter before individual void structures from neighboring nucleation sites begin to influence each other. Ligament velocity increases continuously towards CHF.
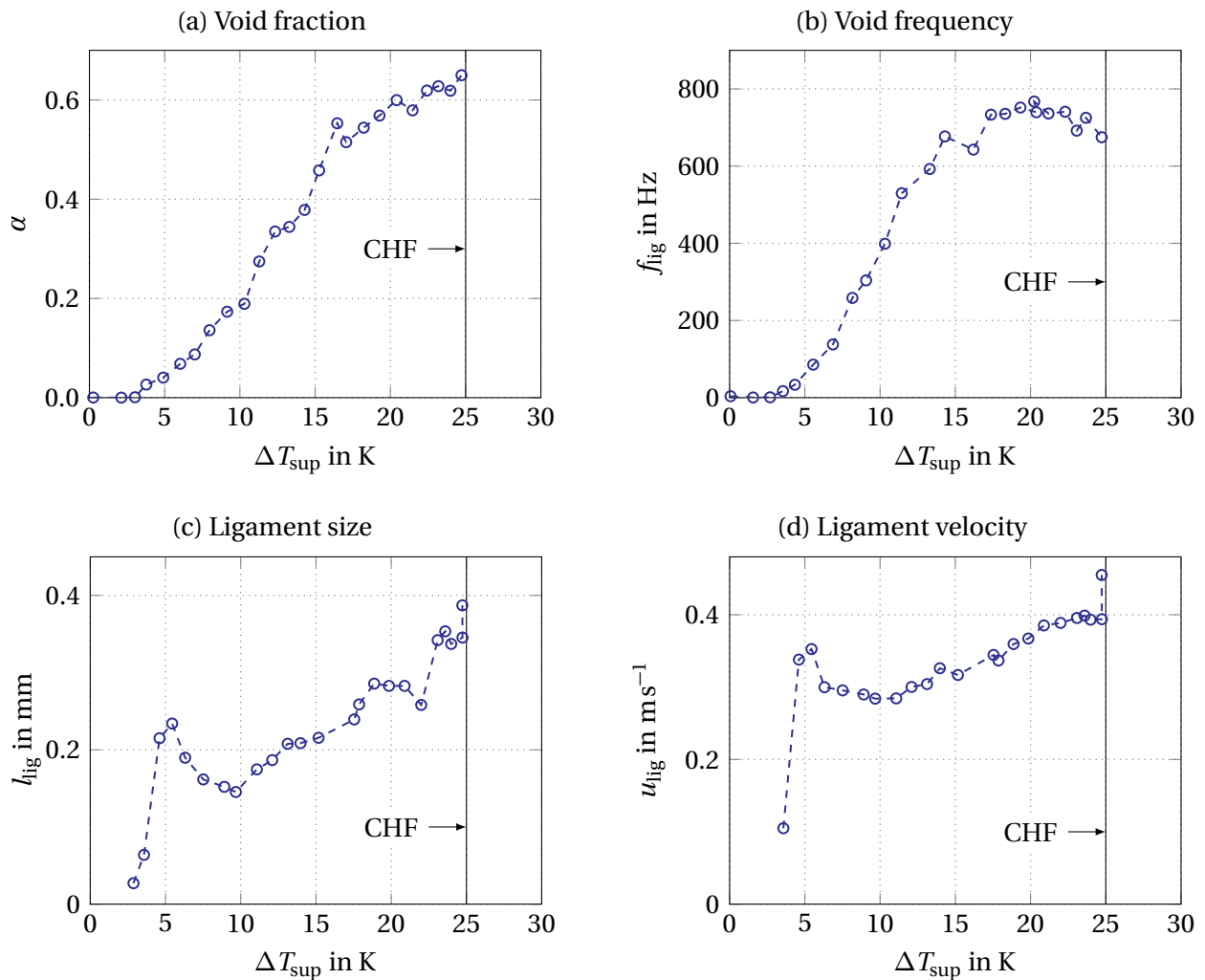
Figure 4.8: Behavior of the void phase along the boiling at the single-rod copper-coated stainless steel heater at $y = 100\,\mu\text{m}$ at the middle measurement position.

The evolution of the void frequency along the boiling curve shown in Fig. 4.8b illustrates why the void frequency remains almost constant between FDB and CHF for the single-rod copper-coated stainless steel heater in Fig. 4.7. Because CHF occurs at a much lower wall superheat compared to the wall-mounted copper heater, the wall superheat at FDB for this heater configuration is $\Delta T_{\text{sup,FDB}} \approx 19\,\text{K}$ compared to $\Delta T_{\text{sup,FDB}} \approx 29\,\text{K}$ for the wall-mounted copper heater. Although the qualitative behavior of the void frequency is similar between the two heater configurations, measurements at FDB capture the evolution of the void frequency at different states along the boiling curve.

4.2.3.2 Behavior During the Critical Heat Flux Transient

Fig. 4.9 shows the time-resolved behavior of the void phase during the CHF transient at three different measurement positions above to the boiling surface. For the data presented in Fig. 4.9, the system was operated at a steady state just below CHF at CHF(-). A marginal increase in heater power then triggered the occurrence of CHF at $t = 0\,\text{s}$. At this time, a temperature excursion of $\Delta T \geq 1\,\text{K}$ relative to the mean temperature at steady-state conditions was first noted.

Void fraction: Before the occurrence of CHF at $t = 0\,\text{s}$ in Fig. 4.9a, void fraction is approximately 10 % lower at the measurement position closest to the heater surface compared to the measurement positions further away from the heater surface. At $t = 0\,\text{s}$, void fraction shows a distinct increase for all measurement positions in wall-normal direction. This was equally observed for the wall-mounted copper heater. After reaching a peak void fraction of approximately 75 % at $t = 4\,\text{s}$, void fraction abruptly decreases at all three distances from the wall and the void fraction gradient close to the wall reverts.

Void frequency: At the onset of the temperature excursion at CHF at $t = 0\,\text{s}$, the void frequency at $y = 87\,\mu\text{m}$ increases and reaches a maximum of 930 Hz at the point of peak void fraction at $t = 4\,\text{s}$. The relative increase of void frequency between these two points in time at $y = 87\,\mu\text{m}$ is approximately 16 %. After reaching its maximum, the void frequency declines rapidly at all three measurement positions as the vapor film is formed.

Ligament size: Before CHF, ligament size increases with increasing wall distance. This profile of ligament sizes in wall normal direction remains unchanged until several seconds after the first detection of CHF, when the ligament size at a wall distance of 87 μm begins to grow rapidly. This growth continues until the maximum void fraction is reached at $t = 4$ s. At this time, void ligaments at the measurement position closest to the heater surface have quadrupled in size and the gradient of void ligament size normal to the wall is inverted.
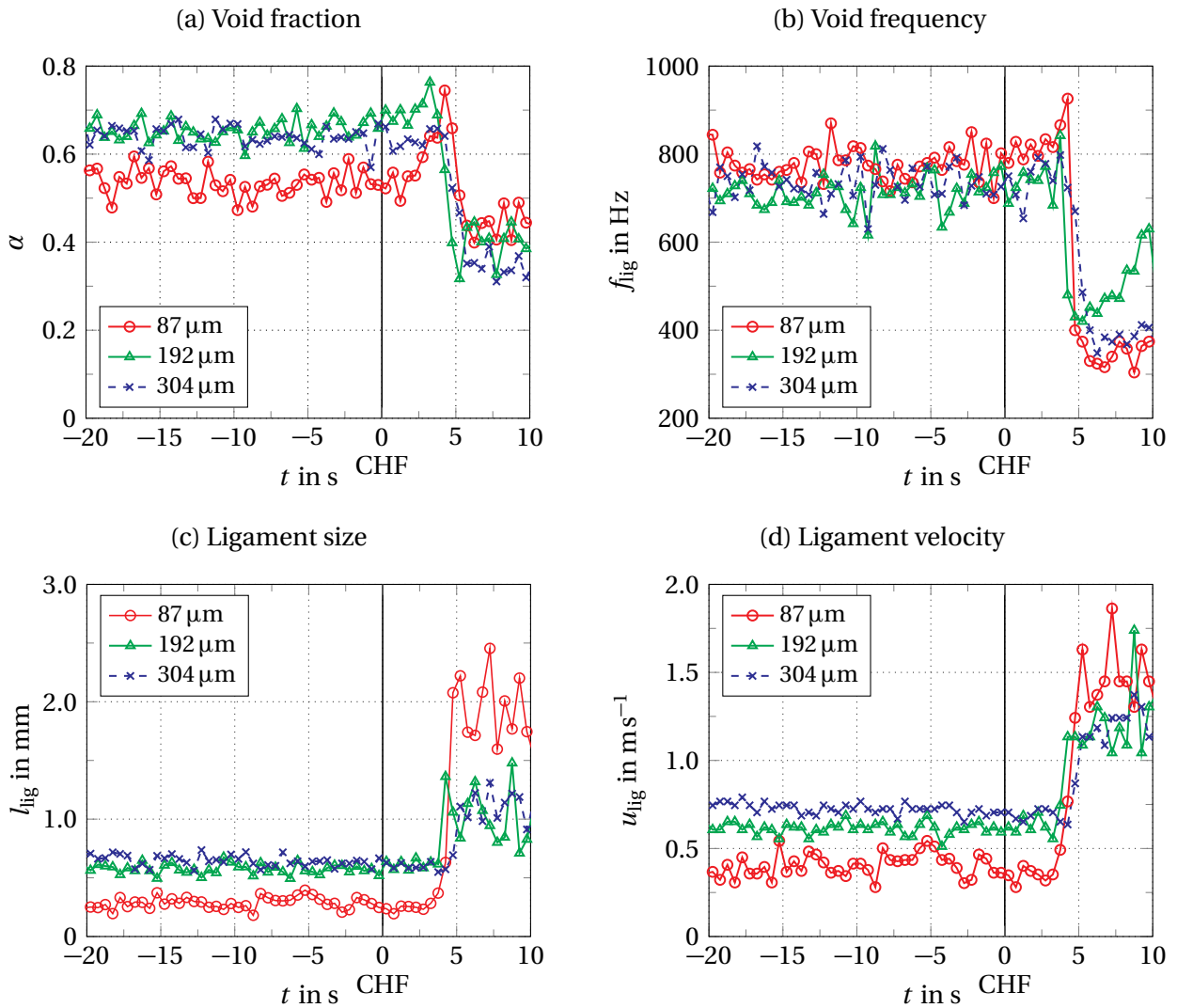
Figure 4.9: Behavior of the void phase during the CHF transient at the single-rod copper-coated stainless steel heater at three different distances from the heater surface at the middle measurement position.

Ligament velocity: The void phase exhibits a steep velocity gradient in the vicinity of the heater surface. The velocity of void structures increases with increasing wall distance before CHF. At the breakdown of heat transfer after CHF, the void phase close to the wall is accelerated. Within 2 s, void structures at 87 µm are accelerated from a velocity of approximately $0.7\,\mathrm{m\,s^{-1}}$ at CHF to more than $1.5\,\mathrm{m\,s^{-1}}$. The void structures closer to the wall are accelerated faster compared to distances further away from the heated surface, which eventually leads to a reversion of the velocity gradient after the formation of the vapor film at $t = 4\,\mathrm{s}$. This has equally been observed for the wall-mounted copper heater.

4.3   Analysis

In this section, the analysis of the results is presented. First, the mechanistic boiling models introduced in Sec. 2.4.2 and Sec. 2.4.4 are assessed with respect to the experimental data. Their predictive capabilities were tested on own experimental critical heat flux data for those models, which have been published in form of a full mathematical formulation. This was the case for the bubble crowding model, the sublayer dry-out model and the interfacial lift-off model. Following the assessment of the mechanistic models, a detailed comparison of the experimental data from both heater configurations is conducted. Based on this comparison, a refined mechanism for the CHF process at the wall is proposed and a common stability limit of the boiling process at CHF is identified.

4.3.1   Evaluation of Mechanistic Critical Heat Flux Models

In the following, the CHF trigger mechanisms and core assumptions of the CHF models discussed in Sec. 2.4.2 and Sec. 2.4.4 are evaluated with respect to the experimental results presented before.

In addition, the performance of the bubble crowding model [180], the sublayer dry-out model [74] and the interfacial lift-off model [15] was tested with critical heat flux data obtained with the wall-mounted copper heater to assess their universal prediction accuracy. For this, the models were implemented

numerically in Matlab. To ensure that each model was implemented correctly, the implementations' accuracy predicting the data sets used for validating the models in the respective source publication was assessed. After successful validation, the models were then tested on 135 critical heat flux data points obtained with the experimental setup of this study. This critical heat flux data was obtained at subcoolings ranging from $1\,\mathrm{K}$ to $33\,\mathrm{K}$ and at mass fluxes between $500\,\mathrm{kg\,m^{-2}\,s^{-1}}$ and $2000\,\mathrm{kg\,m^{-2}\,s^{-1}}$.

Concluding the evaluation of the mechanistic critical heat flux models in this subsection, a short summary and conclusion is drawn.

4.3.1.1 Bubble Crowding Model

Comparison of the implementation with the original model: The implementation of the bubble crowding model was evaluated based on a data set of critical heat flux values for water by Griffel and Bonilla [181]. This data was used to assess the prediction accuracy of the model in the original publication. A parity plot of the calculated surface heat flux at CHF versus the experimentally obtained critical heat flux is shown in Fig. 4.10.
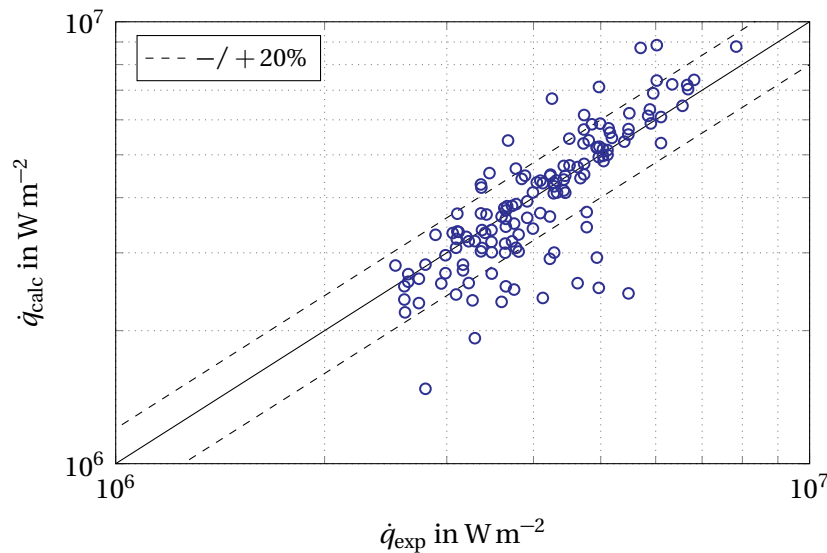
Figure 4.10: Validation of the implementation of the bubble crowding model with critical heat flux data for water of Griffel and Bonilla [181].

The implementation of the model is able to predict the data set with similar accuracy compared to the reported accuracy in the original publication. With

the exception of a few data points, all calculated data lies within a 20 % error range with a standard deviation of the ratio between calculated and measured critical heat flux of $\sigma_{\dot{q}_{\mathrm{calc}}/\dot{q}_{\mathrm{exp}}} = 0.091$. This value is similar to the reported standard deviation in the original publication of $\sigma_{\dot{q}_{\mathrm{calc}}/\dot{q}_{\mathrm{exp}}} = 0.099$.

The correct implementation of the model was further checked with high pressure critical heat flux data for water flowing in a uniformly heated annulus as published by Kwon and Chang [180]. Fig. 4.11 shows the calculated critical heat flux compared to the experimental data for several mass fluxes and subcoolings. The model implementation accurately reproduces the experimental data.
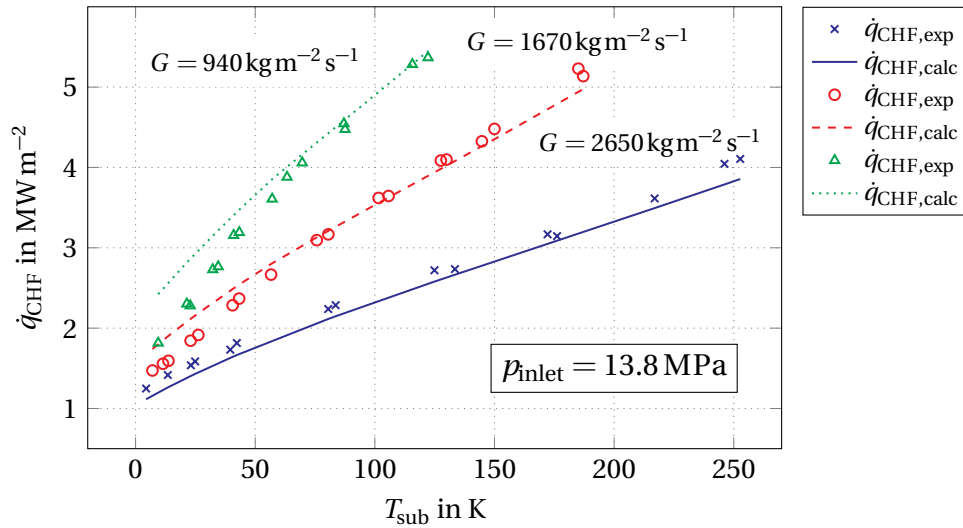
Figure 4.11: Validation of the implementation of the bubble crowding model with critical heat flux data from [180].

Application to data from the wall-mounted copper heater: Fig. 4.12a shows the CHF values predicted by the bubble crowding model for the measured CHF data obtained with the wall-mounted copper heater. The model is not able to predict critical heat flux with reasonable accuracy. While the model's predictions become more accurate for high subcooling, its performance deteriorates at low subcooling. As seen in Fig. 4.12b, the accuracy of the model is strongly dependent on mass flux. It improves for higher mass fluxes and deteriorates for lower mass fluxes.
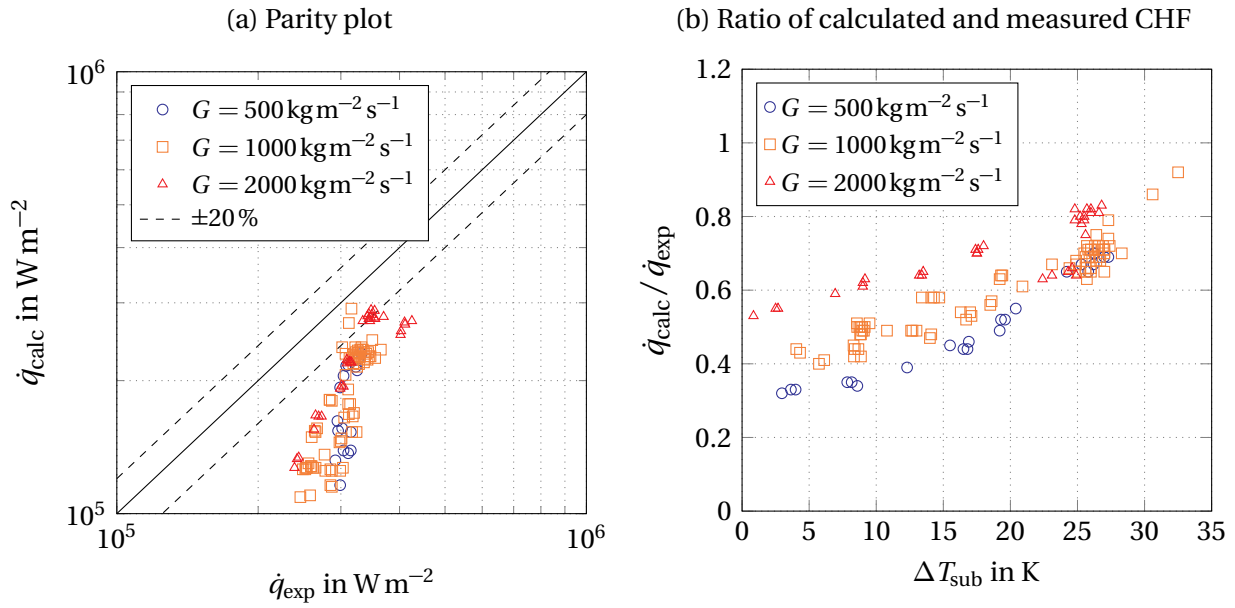
Figure 4.12: Prediction accuracy of the bubble crowding model for critical heat flux data obtained with the wall-mounted copper heater.

Comparison of core assumptions with experimental data: The postulated general flow topology at CHF in the bubble crowding model appears reasonable based on the fiber-optic microprobe data. Fig. 4.4 and Fig. 4.8 support the claim that a bubbly flow is present in the immediate vicinity of the heater surface at CHF. Furthermore, peaks in void fraction after CHF were detected for both the wall-mounted copper heater (Fig. 4.4a) and the single-rod copper-coated stainless steel heater (Fig. 4.9a). This supports the notion of a crowding mechanism in the immediate vicinity of the heater surface around CHF. However, as the increase of vapor was detected several seconds after the occurrence of CHF, it is likely not the cause for CHF.

In the bubble crowding model, turbulent interchange between the core flow and a so-called bubbly layer closer to the heater surface is assumed to be the limiting mechanism leading to CHF once a critical vapor layer thickness with a constant critical void fraction is reached. It has been previously argued by the author in [10] that the boiling process is not critically limited by the blockage of liquid from the bulk flow due to increasing void layer thickness near the wall. In [10], no critical vapor layer thickness was found based on high-speed videometry measurements. Instead, the existence of a small relevant sublayer, which is not significantly influenced by bulk flow turbulence

was postulated. The void profiles in Fig. 4.2 and in Appendix C support both claims. First, the increased accumulation of void near the wall is likely not critically limiting the boiling process as only a small increase of void fraction between the point of fully-developed boiling and CHF was measured near the wall for a multitude of operating conditions. Second, the data of the present study supports the hypothesis that there is a layer, which is largely unaffected by bulk flow turbulence and in which the general flow topology is fundamentally different from the core flow. This was confirmed by a steep increase in void frequencies at a wall distance of approximately 300 μm for all operating conditions.

The existence of a critical void fraction of 82 % in the layer close to the boiling surface at CHF can be refuted. Fig. 4.13 shows void fraction measurements at a wall distance of approximately 100 μm at CHF for both the wall-mounted copper heater as well as the single-rod copper-coated stainless steel heater for various subcoolings and mass fluxes. Inlet subcooling strongly influences the void fraction at CHF. Close to saturation conditions, the measured void fraction is close to the postulated value of 82 %. However, there is a difference of up to 50 % between measurements taken close to saturation conditions and those taken at the highest subcooling. The constant critical void fraction used in the model is therefore not accurate. This has been previously noted equally in other works [14, 74, 182] and is quantitatively proven in this work.
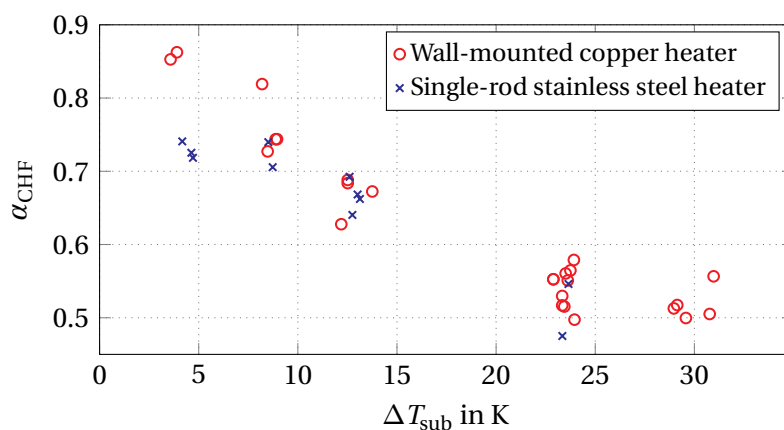
Figure 4.13: Measured void fraction at critical heat flux for a wide range of subcooling and mass flux from experiments with the wall-mounted copper heater and the single-rod copper-coated stainless steel heater. The fiber-optic microprobes were positioned at a wall distance of approximately 100 μm.

4.3.1.2   Sublayer Dry-out Model

Comparison of the implementation with the original model: To validate
the implementation of the sublayer dry-out model, the reference data of the
original publication was reproduced. Fig. 4.14 shows the calculated critical
heat flux in comparison to the original experimental data and the prediction
accuracy of the model as reported in the original publication. The implemen-
tation of the model accurately reproduces the original data for a wide range of
mass fluxes. Additionally, a detailed parameter study was conducted to verify
that the behavior of each parameter of the model is accurately reproduced.
Fig. 4.15 shows the calculated values of the model parameters in compari-
son to the values reported in the original publication. The behavior of each
parameter of the model is reproduced correctly.
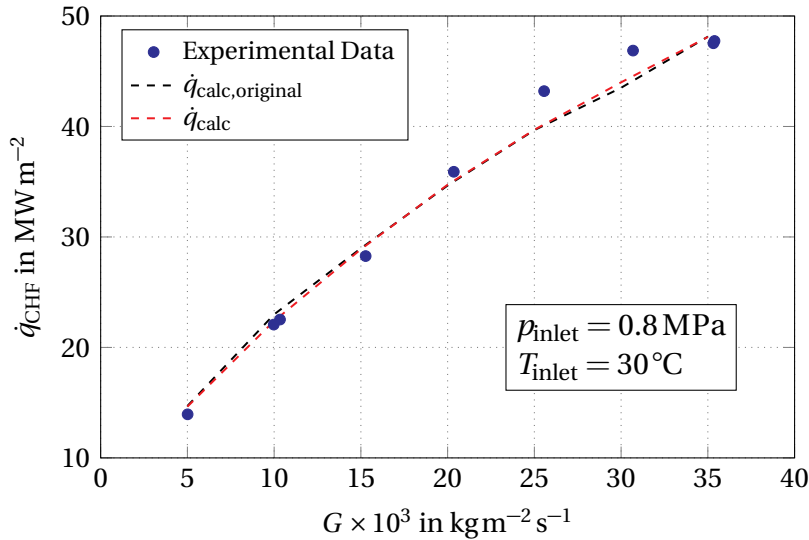
Figure 4.14: Comparison of calculated critical heat flux with experimental data and original
model prediction for the sublayer dry-out model.

Application to data from the wall-mounted copper heater: Fig. 4.16 shows
the performance of the implementation of the sublayer dry-out model for the
CHF data of the wall-mounted copper heater. The sublayer dry-out model is
not able to predict the measured critical heat flux data with reasonable ac-
curacy. Similar to the bubble crowding model, the prediction accuracy im-
proves for higher subcoolings. However, the model fails to produce reason-
able results for data obtained at low subcoolings. As shown in Fig. 4.16b, the
predicted critical heat flux approaches zero for saturation conditions.
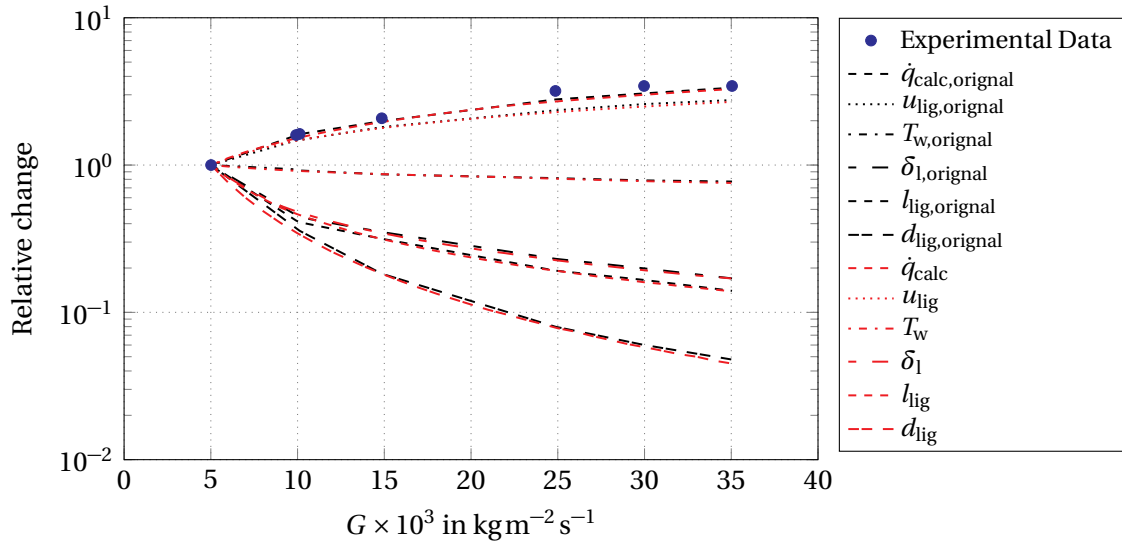
**Figure 4.15:** Change of model parameters of the sublayer dry-out model for different mass fluxes.
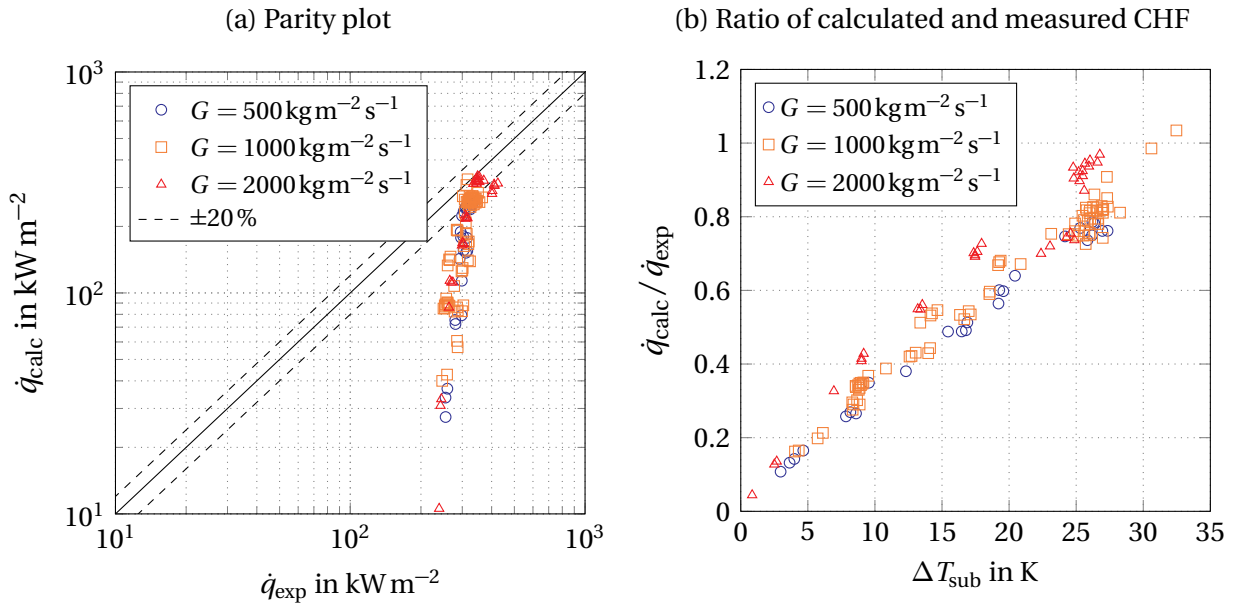
Figure 4.16: Prediction accuracy of the sublayer dry-out model for critical heat flux data obtained with the wall-mounted copper heater.

Tab. 4.2 shows the parameter range of the model as stated in the original publication. The experimental data of this study lies partly at the boundary of the model's validity range. The cause for the model's poor performance at this boundary is the submodel for the calculation of the thickness of the liquid sublayer δ_l beneath the void ligaments. Fig. 4.17 shows the calculated values

of δ_1 for the CHF data obtained with the wall-mounted copper heater. δ_1 approaches zero for saturation conditions, which according to Eq. (2.7) linearly influences the calculated critical heat flux.

Table 4.2: Model parameter range of the sublayer dry-out model in comparison to the data of this study.

Model parameter range	Data of this study within range
$1\,\text{bar} \le p \le 84\,\text{bar}$	Yes
$0.3\,\text{mm} \le d \le 25.4\,\text{mm}$	No
$1 \times 10^3\,\text{kg}\,\text{m}^{-2}\,\text{s}^{-1} \le G \le 9 \times 10^4\,\text{kg}\,\text{m}^{-2}\,\text{s}^{-1}$	Partially
$0.0025\,\text{m} \le l \le 0.61\,\text{m}$	Yes
$25\,\text{K} \le \Delta T_{\text{sub}} \le 255\,\text{K}$	Partially
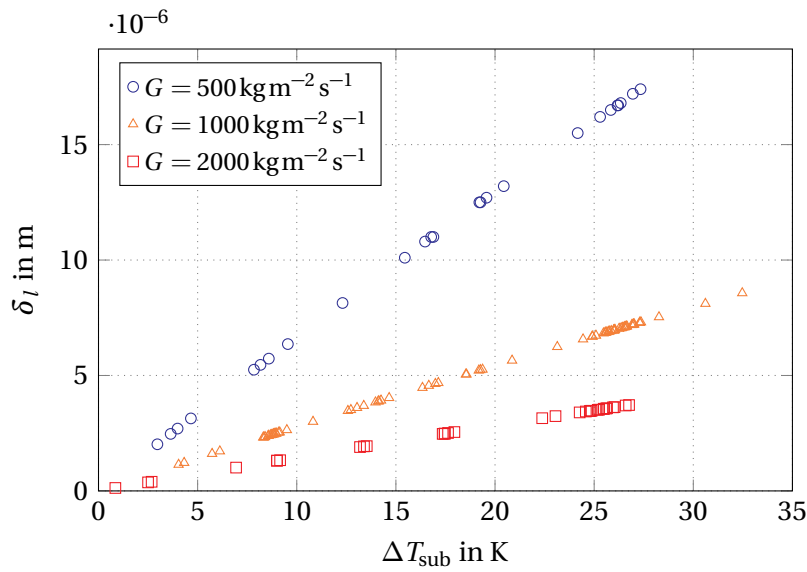
Figure 4.17: Calculated thickness of the liquid sublayer in the sublayer dry-out model for critical heat flux data of the wall-mounted copper heater.

Comparison of core assumptions with experimental data: As noted in other publications [10, 16], the main modeling parameters of the sublayer dry-out model are generally difficult to access experimentally. However, the fiber-optic microprobe data presented in Sec. 4.1.2 and Sec. 4.2.2 can be used to partly assess the validity of some of the model parameters.

The blanket length l_{lig} is postulated to be equal to the critical Helmholtz wavelength and is calculated according to Eq. (2.8). For a mass flux of $G = 1000\,\text{kg}\,\text{m}^{-2}\,\text{s}^{-1}$ and a subcooling of $\Delta T_{\text{sub}} = 13\,\text{K}$, the predicted blanket length is $l_{\text{lig}} \approx 4\,\text{mm}$. This value is approximately four times higher than the void ligament length for the same thermo-hydraulic operating conditions measured at a distance of $100\,\mu\text{m}$ and approximately two times higher than the largest ligament length measured in the core flow as illustrated in Fig. 4.2 and Fig. 4.4.

As shown in Fig. 4.17, the model predicts sublayer thicknesses of several μm for the thermo-hydraulic operating conditions of this study. If a purely liquid sublayer were to be present, a clear decline of void fraction towards the heater wall at all measurement positions along the direction of flow would be expected. While for some operating conditions void fraction was observed to decline at very small distances away from the heated surface (e.g. at the lower measurement position in Fig. 4.2, Fig. C.3a and Fig. C.5a and at the upper measurement position in Fig. C.2a), the majority of measurements provided no evidence for a distinct liquid sublayer at the wall. Instead of the presence of a liquid sublayer, the time-resolved measurements of the void morphology during the CHF transient presented in Fig. 4.4 and Fig. 4.9 provide leverage to the assumption of a well-mixed bubbly two-phase flow in the immediate vicinity of the heater surface at CHF.

4.3.1.3   Interfacial Lift-off Model

Comparison of the implementation with the original model: Fig. 4.18 shows the comparison between the calculated critical heat flux values and the measurement data as well as the calculated critical heat flux values from the original publication for different bulk flow velocities. While the implementation of the interfacial lift-off model reproduces the general trend of the experimental data well, it deviates slightly from the predictions reported in the original publication.

To verify the correct implementation, a detailed comparison of calculated parameters was conducted for each submodel. Fig. 4.19 shows the calculated wavelength of wetting fronts in comparison to the experimental data and the calculated values of the original publication. With the exception of data from
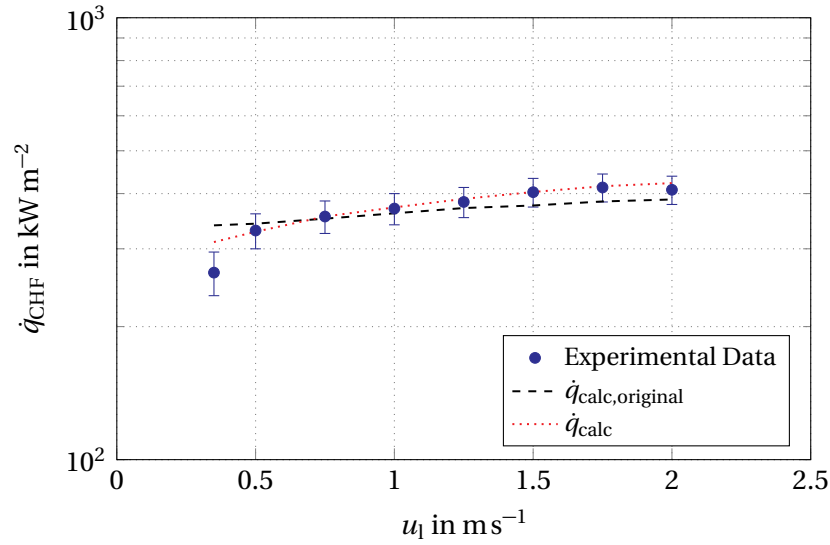
Figure 4.18: Comparison of calculated critical heat flux with experimental data and original model prediction for the interfacial lift-off model.

very low flow velocities, the spacing of consecutive wetting fronts as documented in the source publication is accurately reproduced. Fig. 4.20 shows two parameters of the separated flow model of the interfacial lift-off model. For both, the total pressure drop along the test section and the drift flux, the implementation of this study matches the behavior of the model as documented in the original publication.
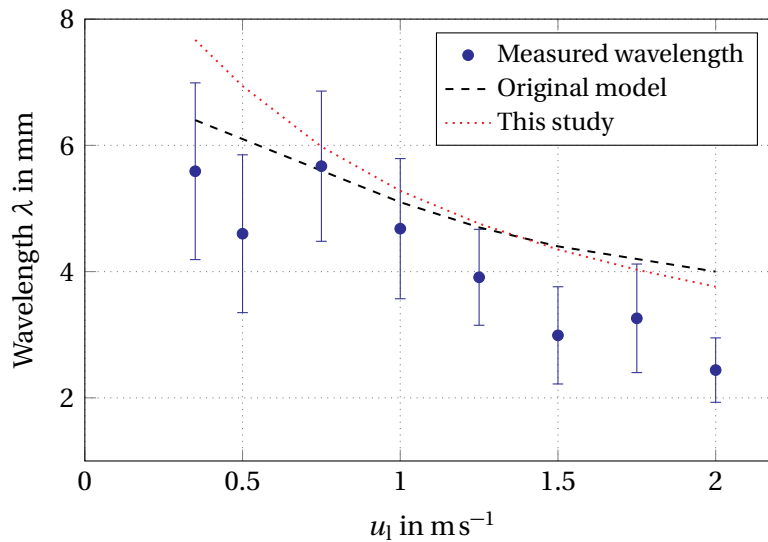
Figure 4.19: Comparison of the wavelength between consecutive wetting-fronts calculated by the implementation of the interfacial lift-off model of this study and the measurement data as well as the calculation of the original publication.

(a) Drift flux (b) Total pressure drop
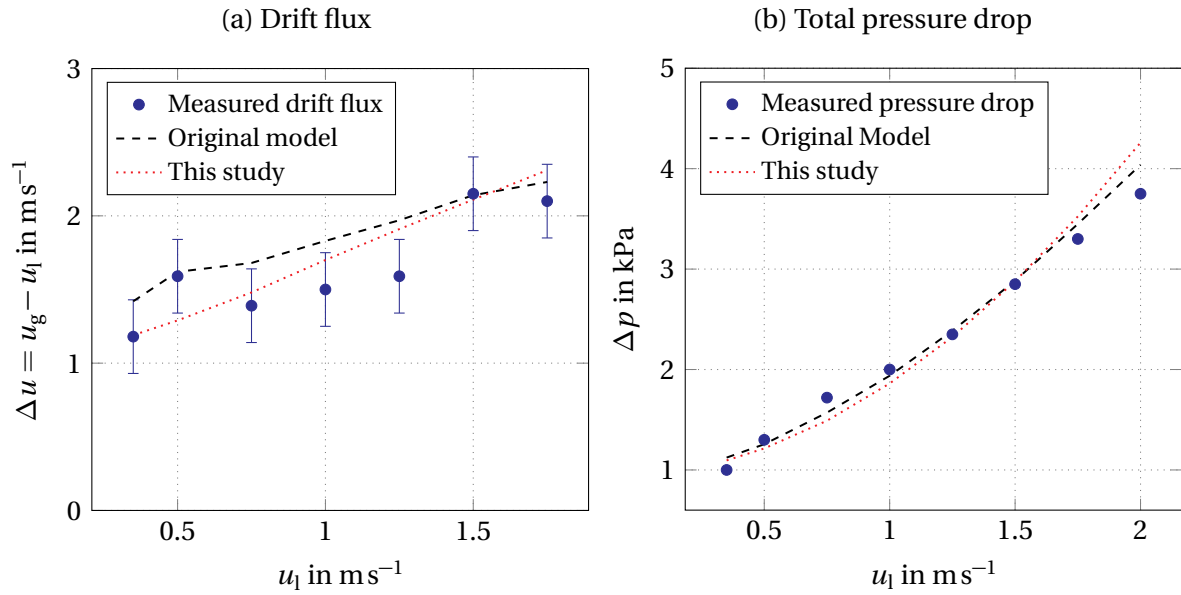
Figure 4.20: Comparison of selected parameters of the separated flow model of the interfacial lift-off model between the implementation of this study and the original publication.

Application to data from the wall-mounted copper heater: As shown in Fig. 4.21, the interfacial lift-off model too fails to predict CHF for the wall-mounted copper heater with reasonable accuracy. However, in contrast to the bubble crowding model and the sublayer dry-out model, the model performs consistently for varying subcooling and mass flux. As seen in Fig. 4.21b, the calculated CHF values are offset by a constant factor of approximately 0.5 compared to the measured value. The model was developed based on experiments with refrigerant FC-87 boiling on a copper heater mounted flush in a rectangular flow channel [96]. This could explain the model's consistent performance for different subcoolings and mass fluxes compared to the bubble-crowding model and the sublayer dry-out model as these models were developed on water-based data sets from experiments with different heater substrates.

Comparison of core assumptions with experimental data: In the formulation of the interfacial lift-off model, heat is only transferred from the boiling surface to the flow through wetting fronts touching the heater surface. However, the fiber-optic microprobe data of the present study suggests a well-
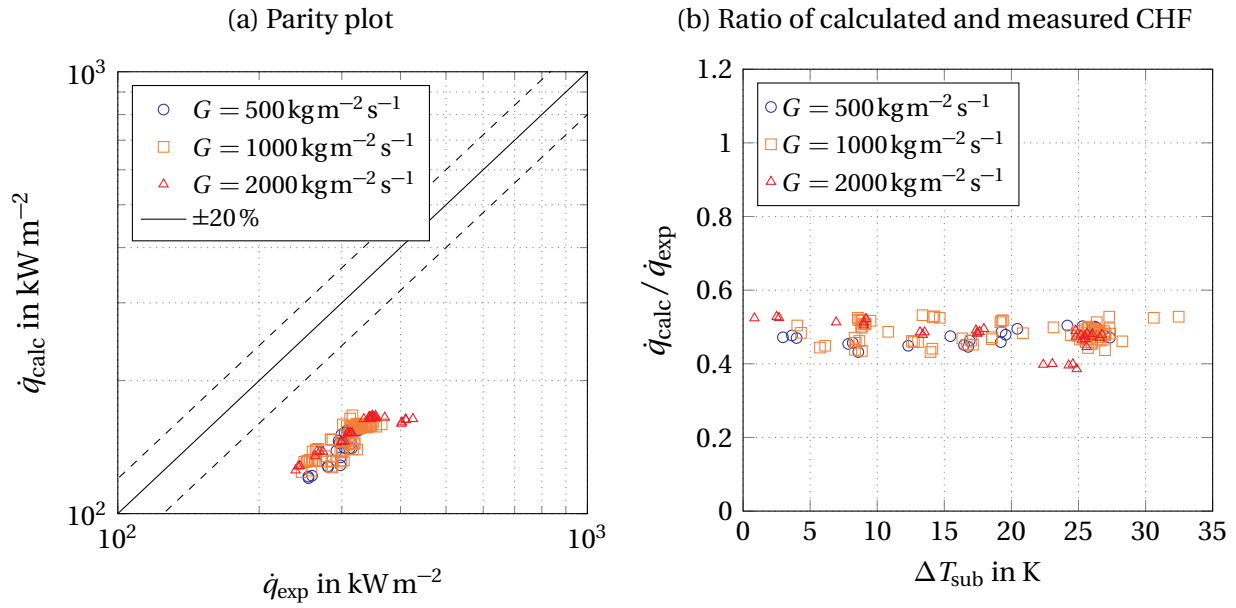
Figure 4.21: Prediction accuracy of the interfacial lift-off model for critical heat flux data obtained with the wall-mounted copper heater.

mixed bubbly flow in the immediate vicinity of the heater surface. This could lead to a systematic under-prediction of critical heat flux for heaters and flow channels larger than those on which the model is based on.

As described in [9, 10], the general flow topology above the heater surface close to CHF qualitatively matches the flow structure postulated by the interfacial lift-off model. In experiments with different subcoolings and mass fluxes, larger vapor agglomerations were observed, which periodically propagated along the heater in the direction of flow. Their wavelength and wetting front spacing matched the model assumptions well [10]. Further providing leverage to the assumption that wetting fronts play a significant part in the heat transfer process, it was observed with particle image velocimetry that subcooled bulk fluid is transported towards the boiling surface in the wake of larger vapor agglomerations [8]. However, the assumption of a wavy vapor layer consisting of purely vapor is not convincing. Fig. 4.4 and Fig. 4.9 illustrate that there is no clear boundary between vapor and liquid at a wall distance of approximately 100 μm above the boiling surface. This contradicts the core assumption of the model. The model is based on experiments with a very narrow flow channel. The depth of the flow channel was 6.4 mm [96] and

5 mm in later publications [101, 182]. The observations from this experiment likely cannot be transferred to larger geometries without modification [16].

Despite this discrepancy, it was investigated whether the observed periodic structures reach the immediate vicinity of the boiling surface. Extending the work by Bloch et al. [16], steady-state experiments were conducted at operating point CHF(-) using a fiber-optic microprobe positioned at wall distances of 1000 μm, 600 μm and 300 μm above the heater surface. Fig. 4.22 shows a FFT analysis of the raw fiber-optic microprobe data from these experiments. At distances up to 600 μm, a slight peak in the frequency spectrum at approximately 50 Hz can be observed. This peak has vanished at a distance of 300 μm, which suggests that the relevant bubbly sublayer postulated in [10] is unaffected by any observed periodic behavior of the void phase further away from the boiling surface.
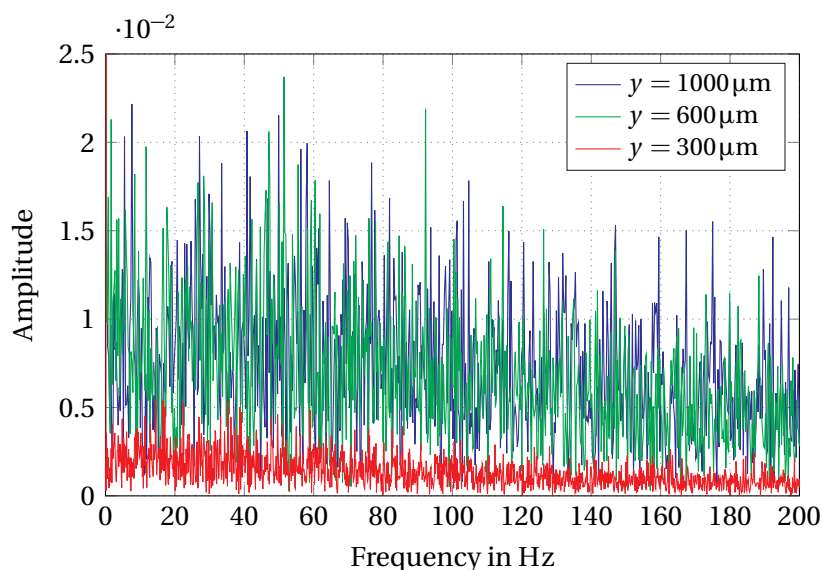
Figure 4.22: FFT analysis of raw fiber-optic microprobe data from experiments with the wall-mounted copper heater right before critical heat flux.

Furthermore, the model assumes a constant wave propagation velocity [15] and does not account for buoyancy-induced acceleration. The change of the void velocity close to the wall at CHF as illustrated in Fig. 4.4 for the wall-mounted copper heater and in Fig. 4.9 for the single-rod copper-coated stainless steel heater is therefore disregarded in the model.

4.3.1.4 Prediction of Critical Heat Flux Initiation in Pool and Flow Boiling by Ding et al. [19]

No set of equations, which would allow for the reprogramming of the model, has been published by Ding et al. yet. The prediction accuracy of the model for the CHF data of the present study could therefore not be assessed personally by the author of the present study. However, Ding et al. have been provided with the same CHF data, which was used to asses the prediction accuracy of the bubble crowding model, the sublayer dry-out model and the interfacial lift-off model in the present study. They subsequently used this data to asses the prediction accuracy of their model [183]. Ding et al. kindly provided the author of the present work with the predicted critical heat flux values. Fig. 4.23a shows the critical heat flux predicted by the model compared with the measured critical heat flux. While the model fails to predict critical heat flux with reasonable accuracy for the experimental data obtained at a mass flux of $G = 500\,\mathrm{kg\,m^{-2}\,s^{-1}}$, its accuracy improves at higher mass flux. As seen in Fig. 4.12b, the model becomes more accurate for data obtained at $G = 1000\,\mathrm{kg\,m^{-2}\,s^{-1}}$ for a wide range of subcoolings.
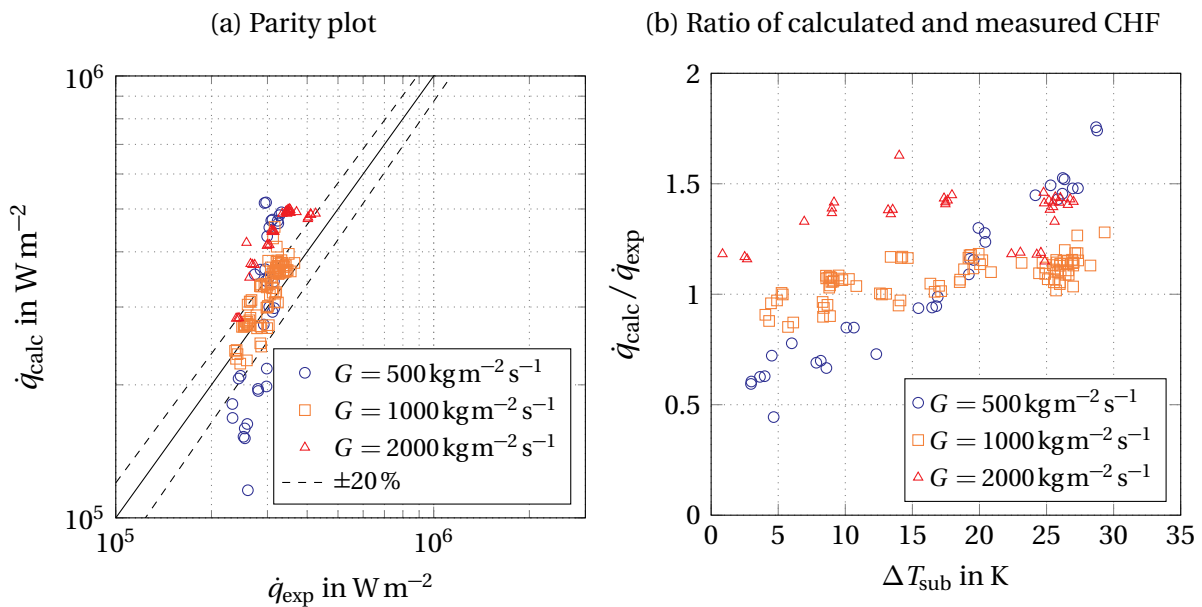
Figure 4.23: Prediction accuracy of the model for the prediction of critical heat flux initiation in pool and flow boiling by Ding et al. [19] for critical heat flux data obtained with the wall-mounted copper heater.

Unfortunately, no explanation for the inconsistent prediction accuracy for different mass fluxes can be given in the present work. However, the mechanism for the initiation of CHF as described in Sec. 2.4.4 poses an interesting basis for experimental validation using the fiber-optic microprobes and is investigated in more detail in the following. The new concept for the initiation of CHF is based on the analysis of the time scales of bubble formation on the heater surface. The time scales of bubble formation can be divided into two parts: First, the time of the presence of vapor on the heater surface. Second, the waiting time between the departure and the subsequent reformation of a bubble during which liquid is present on the heater surface. This data can be accessed via fiber-optic microprobes placed in the immediate vicinity of the heater surface, which measure the mean bubble period $1/f_{\text{lig}}$ and the mean void ligament contact time t_{lig}. Fig. 4.24 shows the mean waiting time $t_{\text{w}} = (1/f_{\text{lig}}) - t_{\text{lig}}$ between the detection of two consecutive void ligaments, the void ligament contact time t_{lig} and the recovery time t_{r} of the thermal boundary layer according to Eq. (2.20). t_{r} was calculated with measured temperature and heat flux data. All data was obtained at a wall distance of $100\,\mu\text{m}$ with the wall-mounted copper heater at $G = 1000\,\text{kg}\,\text{m}^{-2}\,\text{s}^{-1}$ and $\Delta T_{\text{sub}} = 13\,\text{K}$. The data is plotted against the normalized wall superheat $\Delta T_{\text{sup}}/\Delta T_{\text{sup,CHF}}$.
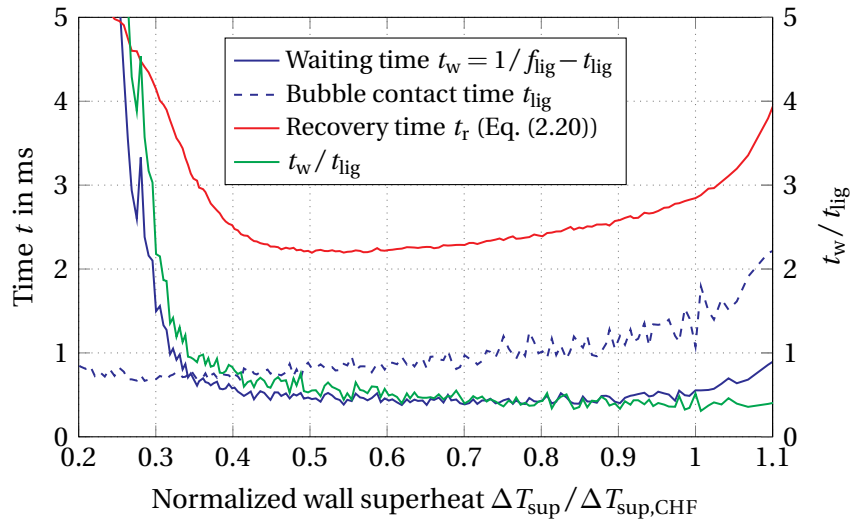
Figure 4.24: Evolution of the mean waiting time, the calculated recovery time of the thermal boundary layer and the mean void ligament contact time.

The qualitative evolution of the measured waiting time t_{w} is matched reasonably well by the calculated recovery time of the thermal boundary layer t_{r}

according to Eq. (2.20). However, the measured waiting time t_w between the detection of consecutive void ligaments is approximately four times smaller than the calculated recovery time t_r. According to Ding et al. [19], Eq. (2.20) stems from the work of Zhao et al. [107], who developed a microlayer-based boiling model for pool boiling. As forced convection is not considered in Eq. (2.20), its applicability is likely limited to pool boiling or flow boiling under very low mass flux conditions. However, the evolution of t_w and t_{lig} along the boiling curve provides leverage to the idea that the time scales of bubble adhesion and liquid presence on the heater surface are key to the initiation of CHF. As illustrated on the right ordinate of Fig. 4.24, the ratio of t_w / t_{lig} becomes continuously smaller as CHF is approached and is minimal around CHF. This suggests that the boiling process becomes unstable once a certain ratio of t_w / t_{lig} is reached. This behavior was confirmed by additional experiments with the wall-mounted copper heater. Fig. 4.25 shows data from fiber-optic microprobe experiments at six different operating conditions at a wall distance of $100\,\mu$m. A similar evolution along the boiling curve up to CHF is observed for all operating conditions. At the same subcooling, the ratio of t_w / t_{lig} converges to a similar value at CHF for a wide range of mass fluxes. For a subcooling of $\Delta T_{sub} = 24\,$K, t_w / t_{lig} has a value of approximately 0.75. This value decreases to approximately 0.3 for a subcooling of $\Delta T_{sub} = 13\,$K.

4.3.1.5 Prediction of Critical Heat Flux in Multi-Phase Computational Fluid Dynamics by Baglietto et al. [18, 120]

No set of equations, which would allow for the reprogramming of the model, has been made public by Baglietto et al. yet. Hence, the performance of the proposed modeling approach could not be assessed. However, its core innovation as summarized in Sec. 2.4.4.2 and described in more detail in [18, 120, 125] poses an interesting basis for experimental validation. The idea that the temporary deactivation and subsequent saturation of available nucleation sites on the heater surface is the key to the limitation of transferable heat is assessed in the following.

In the nucleate boiling regime before CHF, overall heat transfer is strongly governed by the number of nucleated void structures on the heater surface. As postulated by Baglietto et al., these structures will begin to interact with
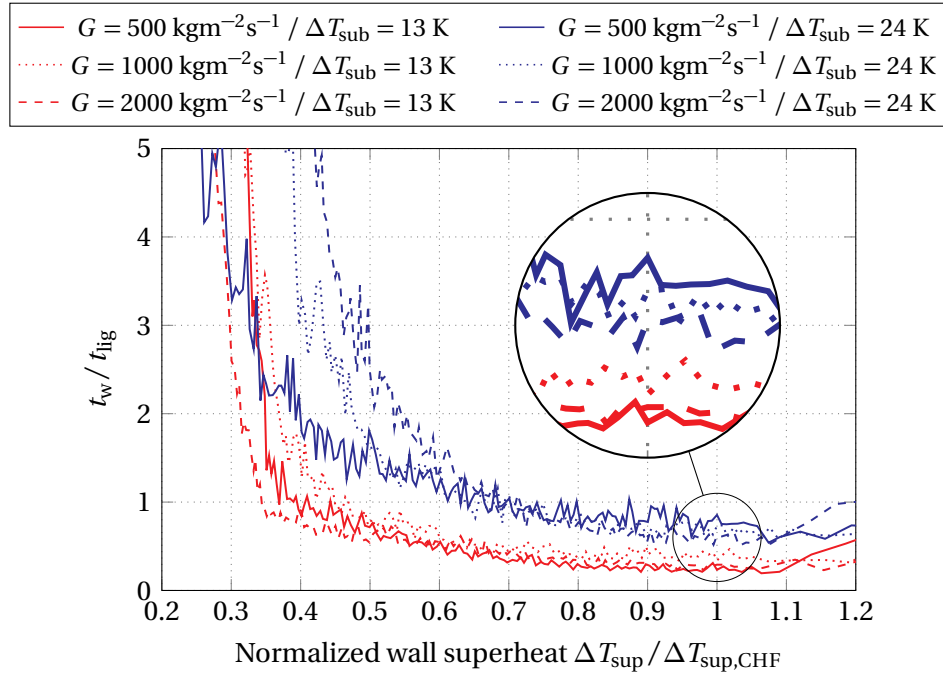
Figure 4.25: Evolution of the ratio between waiting time and void ligament contact time obtained with fiber-optic microprobes positioned at a wall distance of $100\,\mu m$ at the middle measurement position of the wall-mounted copper heater for different operating conditions.

each other at higher wall superheat and temporarily deactivate neighboring nucleation sites. This decreases the rate of increase of boiling heat transfer. If such a mechanism exists, a decrease in void frequency at a characteristic void ligament size would be expected very close to the wall. This has been observed for both the wall-mounted copper heater and the single-rod copper-coated stainless steel heater. As the surface properties of both heater configurations are the same, similar nucleation site behavior and therefore similar behavior regarding the temporary deactivation of nucleation sites would be expected. As shown in Fig. 4.4 and Fig. 4.8, a void ligament size of approximately $0.3\,mm$ - $0.4\,mm$ is observed at the point of maximum void frequency for both heater configurations. The operating conditions of $G = 1000\,kgm^{-2}s^{-1}$ and $\Delta T_{sub} = 13\,K$ were the same for both experiments. In both cases, the point of maximum void frequency occurred at a wall superheat of approximately $20\,K$. As evidenced in Fig. 4.4, this wall superheat marks the onset of a continuous decline in effective heat transfer coefficient providing leverage to the supposition by Baglietto et al. that the limitation

of active nucleation sites is a governing parameter for the limitation of heat transfer at higher wall superheat.

If the temporary deactivation of nucleation sites is a universal phenomenon, this effect should equally occur at any operating condition. To test this, additional experiments with different mass fluxes and subcoolings were performed with the wall-mounted copper heater. Fig. 4.26 shows data from double-fiber microprobe experiments at a wall distance of $100\,\mu$m at the middle measurement position along the direction of flow for four operating conditions plotted over the wall superheat normalized to the wall superheat at CHF for each experiment.
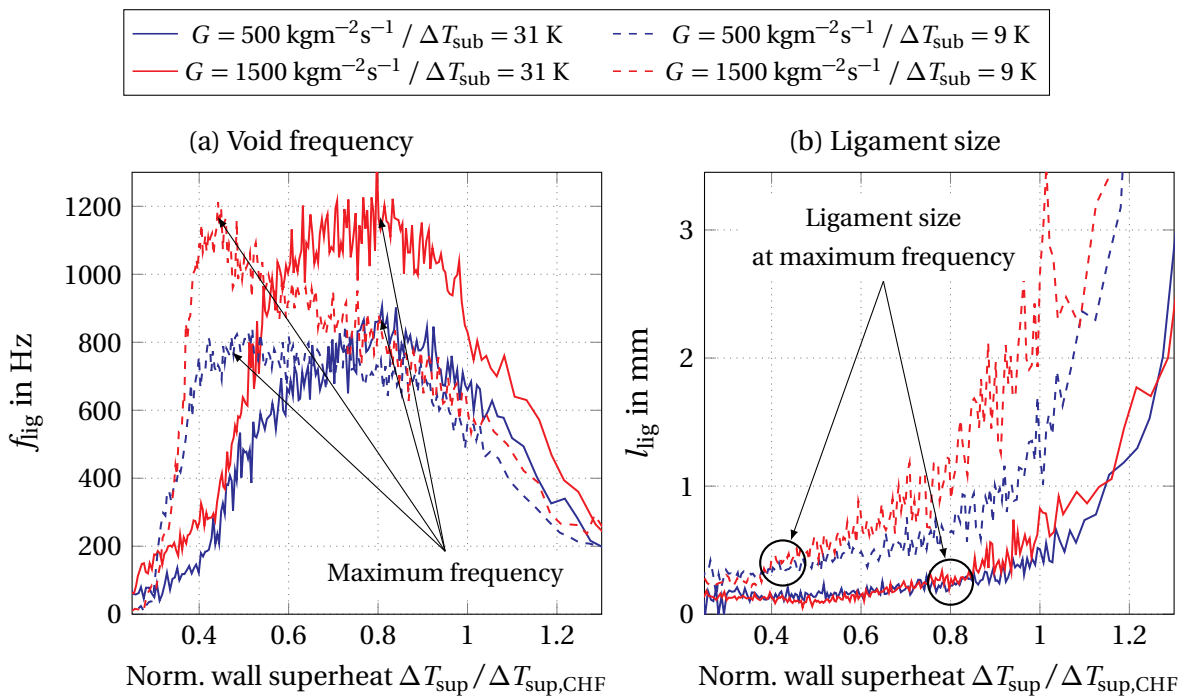
Figure 4.26: Evolution of void ligament size and void frequency for four operating conditions at a wall distance of $y = 100\,\mu$m at the middle measurement position of the wall-mounted copper heater.

As seen in Fig 4.26a, a maximum void frequency exists for all operating conditions. The maximum frequency becomes higher for higher mass flux. For the same mass flux at different subcoolings, approximately the same maximum frequency was measured. However, the maximum frequency occurs at a lower wall superheat for lower subcooling. For a subcooling of 31 K, the peak frequency occurs at $\Delta T_{\text{sup}}/\Delta T_{\text{sup,CHF}} \approx 0.8$. For a subcooling of 9 K this value shifts to approximately 0.45. Fig. 4.26b shows void ligament sizes from

the same measurements. The ligament size at maximum frequency is similar between all operating conditions. Ligament sizes of approximately 0.3 mm were observed for a subcooling of 31 K, while ligament sizes at a subcooling of 9 K are marginally bigger at approximately 0.4 mm. This difference is in the order of magnitude of the measurement uncertainty of the size of void ligaments according to Tab. 3.2. However, the observed trend of slightly bigger ligament sizes at the maximum void frequency for lower subcooling is reasonable and agrees with the theory of Baglietto et al.: As illustrated in Fig. 2.8, less nucleation sites are active at lower wall superheat. The mean distance between active nucleation sites is larger at low wall superheat compared to high wall superheat. Therefore, a larger characteristic size of void structures before a deactivation of neighboring nucleation sites occurs is expected at lower wall superheat. The experimental data hence confirms the limitation of transferable heat by the temporary deactivation of available nucleation sites due to overlapping according to Eq. (2.24).

4.3.1.6 Summary and Conclusion

The three classic mechanistic models - the bubble crowding model, the sublayer dry-out model and the interfacial lift-off model - are widely recognized and have been validated with numerous experimental data in the original publications. However, despite their mechanistic nature, the models are not universal. As shown in this study, they lack predictive capabilities when subjected to data from experimental setups, which differ from the original validation experiments. Based on the data presented above and as discussed in [10], some parts of the underlying physical mechanisms of these models appear reasonable, while some assumptions regarding the flow topology at CHF are not supported by the experimental data. All three models postulate a hydrodynamic limitation of the boiling process in the so-called macrolayer [108] above the heater surface. A purely hydrodynamic limitation makes it difficult to explain the influence of surface properties, like surface roughness and wettability as well as the influence of the heater substrate on critical heat flux. As illustrated by Fig. 4.4b and Fig. 4.6, the substrate material of the heater greatly influences both the wall superheat at CHF and the critical heat flux value. Furthermore, the occurrence of CHF is treated as an independent phenomenon in these models. No sudden change in flow topology near the heater surface

can be seen close to CHF in for example Fig. 4.4. As CHF marks the upper limit of the nucleate boiling regime, it is reasonable to assume that the governing parameters of CHF develop continuously along the boiling curve and interact in a way which eventually causes CHF.

The next-generation models, while not established yet, build on recent experimental advancements and model the boiling process in the microlayer region between individual void structures and the boiling surface. Some of their core assumptions are supported by the experimental data of this study:

- In the case of the new model for the quantitative prediction of critical heat flux initiation in pool and flow boiling by Ding et al. [19], the experimental data supports the claim that the time scales of the intermittent wetting and dewetting process in the immediate vicinity of the wall are key to the limitation of the nucleate boiling process.

- In the case of the new modeling approach for the prediction of CHF in multi-phase CFD by Baglietto et al. [18, 120], the core assumption that an overlapping mechanism between neighboring bubbles induces a natural limitation to the boiling process was validated by void frequency and void ligament size measurements very close to the boiling surface. In contrast to the classic mechanistic models, CHF is not treated as an independent phenomenon in the approach by Baglietto et al. Instead, the boiling process is modeled continuously along the boiling curve. Therefore this approach in particular appears conceptually superior to the macrolayer models.

Both concepts consider the thermal response of the heater substrate to the formation of bubbles and their interaction on the heater surface. This phenomenon has been identified by Kharangate and Mudawar [11] as key to a successful simulation of nucleate boiling heat transfer at high heat fluxes. The present study provides experimental data of critical heat flux and wall temperature for two different heater configurations with the same surface characteristics but made of two different heater substrate materials with technically relevant thickness. In addition, the present study further provides detailed information about the morphology and the dynamics of void structures in the immediate vicinity of the boiling surface of both heater configurations by means of fiber-optic microprobes. Experiments on heaters with

technically relevant thickness can be considered crucial in the advancement of current and future boiling models, as lateral heat conduction plays a key role in all boiling scenarios [11] and especially close to CHF [34]. Therefore, a more detailed comparison of the experimental data presented in Sec. 4.1 and Sec. 4.2 is conducted in the following. Common characteristics are identified between the two heater configurations to shed further light on the heat transfer process along the boiling curve and on the governing parameters of the limiting mechanism at CHF. To the knowledge of the author, no study has provided comprehensive data on the void dynamics in the immediate vicinity of the boiling surface for two different heater substrates with technically relevant thickness for subcooled flow boiling yet. The following analysis of the data of the present study therefore aims to contribute to the understanding of the processes leading to the occurrence of critical heat flux for subcooled flow boiling.

4.3.2 Analysis of the Experimental Results

For both heater configurations and the majority of all cases, the transition to CHF originated from a position on the heater surface close to the middle measurement position, i.e. at TCR 2 and TC 2 for the respective heater configurations. All subsequent data of this study is therefore presented for the middle measurement positions as depicted in Fig. 3.4 and Fig. 3.5.

4.3.2.1 Boiling Curves

Fig. 4.27 shows heat flux data from both heater configurations from experiments at $G = 1000\,\mathrm{kg\,m^{-2}\,s^{-1}}$ and $\Delta T_{\mathrm{sub}} = 13\,\mathrm{K}$. The boiling curves of the two heater configurations differ significantly.

Single-phase convective heat transfer: The single-phase convective heat transfer for the wall-mounted copper heater is much higher than that of the single-rod copper-coated stainless steel heater. The single-phase heat transfer for the given thermo-hydraulic operating conditions was calculated for a fully-developed flow based on the Nusselt correlation in Eq. (4.3) [184].
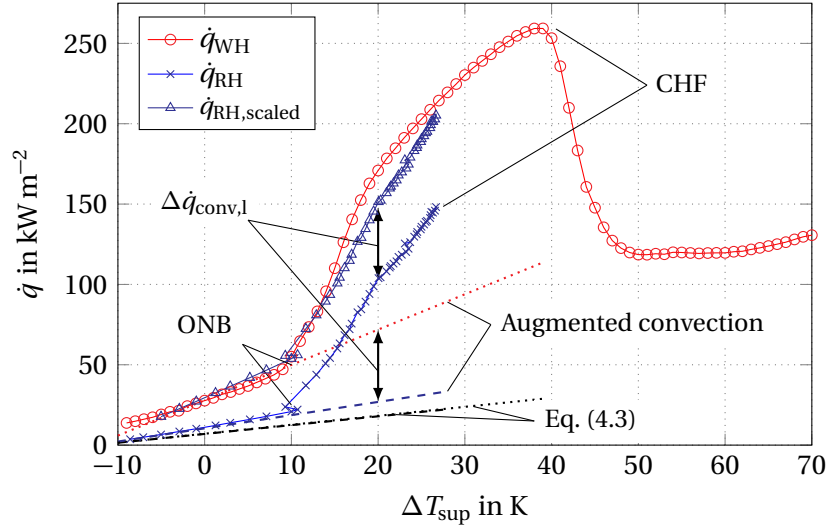
Figure 4.27: Comparison of boiling curves between the two heater configurations for operating conditions of $G = 1000\,\mathrm{kg\,m^{-2}\,s^{-1}}$ and $\Delta T_{\mathrm{sub}} = 13\,\mathrm{K}$.

$$\mathrm{Nu}_\infty = 0.0296\,\mathrm{Re}^{4/5}\mathrm{Pr}^{1/3} \tag{4.3}$$

As seen in Fig. 4.27, both heater configurations show an augmentation of liquid convective heat transfer with respect to the fully-developed case. The augmentation of single-phase convective heat transfer was calculated for both configurations according to Kays and Crawford [185], Eq. (13-18) and Eq. (13-23), as follows. At a ratio of $l_{\mathrm{TCR2}}/d_{\mathrm{hyd}} = 5.85$ for the wall-mounted copper heater and $l_{\mathrm{TC2}}/d_{\mathrm{hyd}} = 11.5$ for single-rod copper-coated stainless steel heater, the flow is not fully-developed in either case. This leads to higher local Nusselt numbers Nu compared to a fully-developed flow according to Eq. (4.4).

$$\frac{\mathrm{Nu}}{\mathrm{Nu}_\infty} = 1 + \frac{7}{l/d_{\mathrm{hyd}}} \tag{4.4}$$

In the case of the wall-mounted copper heater, the peripheral heat flux profile is non-uniform. This causes additional heat transfer augmentation. The heater material and the surrounding wall of the flow channel can be expected to smooth out temperature variations because of their thermal conductivity [185]. The profile of peripheral heat flux was therefore approximated by a cosine function according to Eq. (4.5).

$$\dot{q}(\varphi) = \dot{q}(1 + \cos(\varphi)) \tag{4.5}$$

The augmentation of the local peripheral Nusselt number $\mathrm{Nu}(\varphi)$ due to the non-uniform peripheral heat flux profile is then calculated according to Eq. (4.6).

$$\mathrm{Nu}(\varphi) = \frac{1 + \cos(\varphi)}{1/\mathrm{Nu} + f(\mathrm{Re}, \mathrm{Pr})\cos(\varphi)} \tag{4.6}$$

The value of the circumferential heat flux function $f(\mathrm{Re}, \mathrm{Pr})$ becomes very small for the Prandtl and Reynolds numbers of this study and can therefore be neglected [185] in a first approximation. For the wall-mounted copper heater, the augmentation factor is approximately 4.2 and for the single-rod copper-coated stainless steel heater it is 1.6. The calculated augmented single-phase liquid convection is plotted in Fig. 4.27 and closely matches the experimental data.

The nucleate boiling regime: To compare the influence of nucleate boiling heat transfer on the boiling curve, the difference in single-phase convective heat transfer between the two heater configurations has to be eliminated. Hence, the difference in heat flux from single-phase liquid convection $\Delta\dot{q}_{\mathrm{l,conv}}$ as illustrated in Fig. 4.27 was calculated up to CHF and was then added to the boiling curve of the single-rod copper-coated stainless steel heater. This is illustrated in Fig. 4.27. The scaled boiling curve of the single-rod copper-coated stainless steel heater closely matches the boiling curve of the wall-mounted copper heater. Additionally, the onset of nucleate boiling (ONB) occurs at approximately the same wall superheat of $\Delta T_{\mathrm{sup}} = 10\,\mathrm{K}$. This confirms that the surface characteristics of the two heater configurations are nearly identical. Despite close resemblance between the measured boiling curve of the wall-mounted copper heater and the scaled boiling curve of the single-rod copper-coated stainless steel heater, the heat flux for a given wall superheat is systematically higher for the wall-mounted copper heater in the nucleate boiling regime. It is suspected that heat transfer from the wall-mounted copper heater during boiling is augmented by the presence of secondary convective effects above the surface. A qualitative numerical study of the flow processes

above the heater surface was conducted in OpenFOAM using a volume-of-fluid approach to investigate this further [5]. Fig. 4.28 shows the flow morphology above the wall-mounted copper heater during vapor production at the wall. The surface contour for a constant void fraction of $\alpha = 0.5$ is illustrated. In the middle of the heated surface there is a region with significantly lower void accumulation. This confirms the existence of vapor-induced secondary flows above the surface during boiling. They facilitate the replenishment of the heater surface with fresh liquid from the bulk flow which in turn enhances heat transfer.
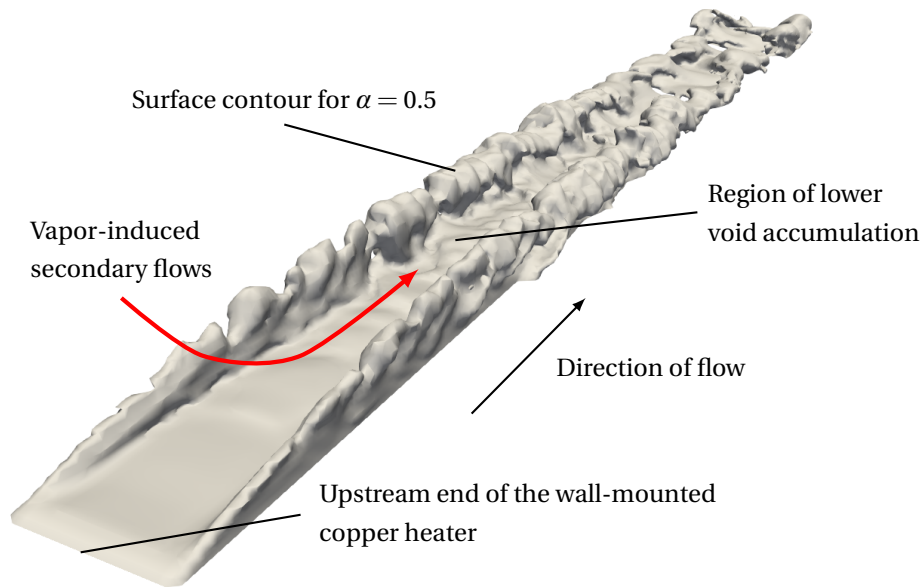
Figure 4.28: Simulation of the three-dimensional flow morphology during vapor production at the wall of the wall-mounted copper heater. Picture rotated clockwise by 45°.

The measured critical heat flux of $\dot{q}_{\text{CHF}} = 259\,\text{kW}\,\text{m}^{-2}$ at $\Delta T_{\text{sup}} = 38\,\text{K}$ for the wall-mounted copper heater is significantly higher compared to the single-rod copper-coated stainless steel heater with $\dot{q}_{\text{CHF}} = 148\,\text{kW}\,\text{m}^{-2}$ at $\Delta T_{\text{sup}} = 27\,\text{K}$. A more detailed look into the void morphology above the surface of each heater is needed to explain this deviation.

4.3.2.2 Void Morphology

Fig. 4.29 shows data of void fraction, void frequency and ligament size for both heater configurations from experiments at $G = 1000\,\text{kg}\,\text{m}^{-2}\,\text{s}^{-1}$ and $\Delta T_{\text{sub}} = 13\,\text{K}$. The fiber-optic microprobes were placed at a wall distance of $y = 100\,\mu\text{m}$.
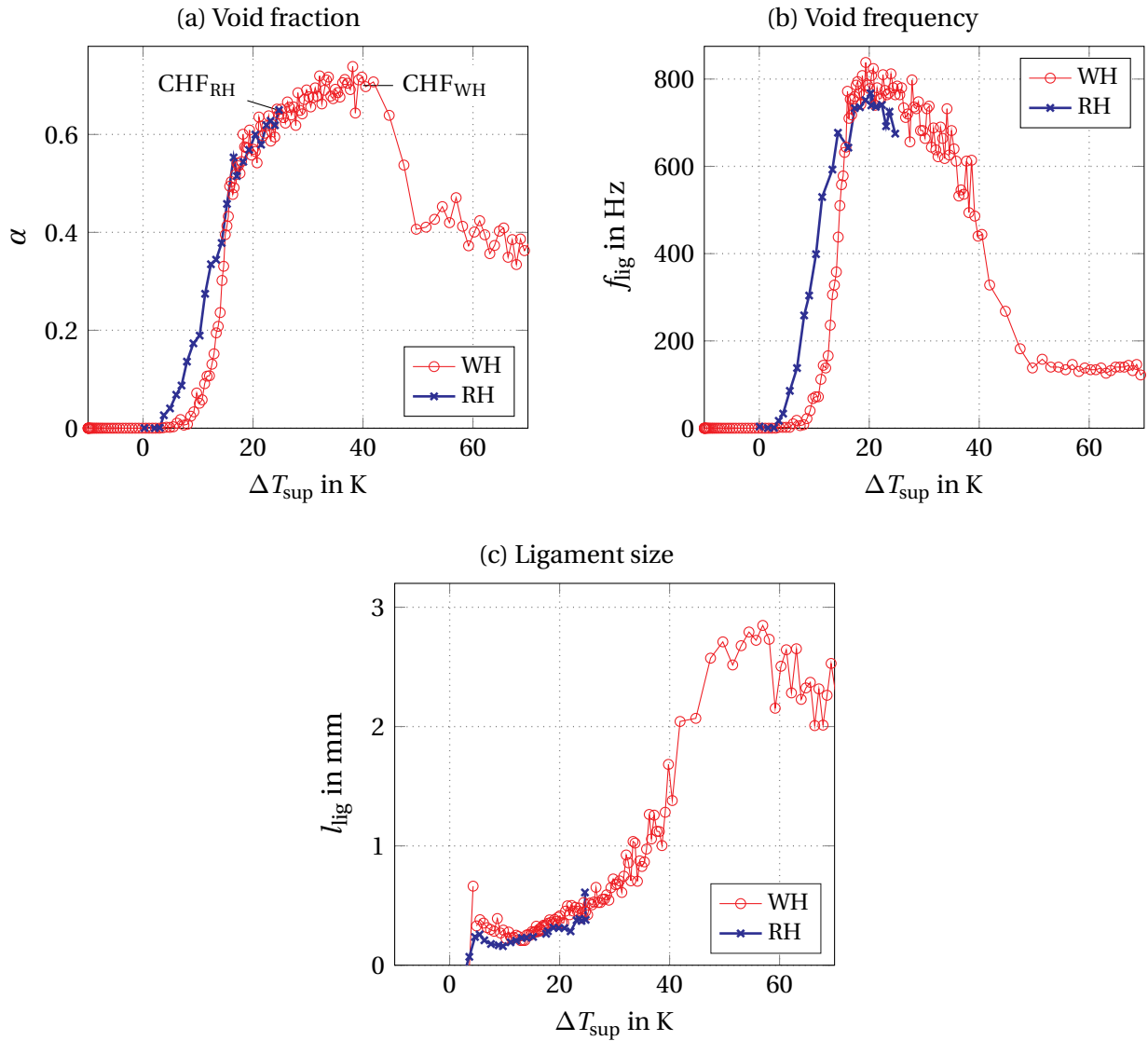
Figure 4.29: Comparison between the two heater configurations of void data obtained by fiber-optic microprobes placed at a wall distance of 100 μm at the middle measurement position for $G = 1000\,\text{kg}\,\text{m}^{-2}\,\text{s}^{-1}$ and $\Delta T_\text{sub} = 13\,\text{K}$.

For both heaters, void fraction increases quickly with rising wall superheat at ONB. A linear increase from the point of fully-developed boiling at $\Delta T_\text{sup} \approx 20\,\text{K}$ until the occurrence of CHF was observed. Equally, void frequencies show a steep increase beyond ONB as more nucleation sites are activated with rising wall superheat. Following the initial rise at ONB, a distinct peak in void frequency of approximately 850 Hz for the wall-mounted copper heater and 750 Hz for the single-rod copper-coated stainless steel heater is observed. After this peak, void frequencies start to decrease continuously until CHF

occurs. Ligament sizes grow steadily with increasing wall superheat. At the point of peak frequency, both heater configurations exhibit a ligament size of approximately 0.35 mm. After reaching a peak frequency at approximately $\Delta T_{\text{sup}} = 20\,\text{K}$, void ligaments continue to grow with increasing wall temperature. The intermittency of the void structures in the immediate vicinity of the heater surface steadily decreases towards CHF. This leads to less stirring of single-phase liquid at the heater surface by departing bubbles and reduces the effective heat transfer coefficient. This is evidenced by a change in slope for both boiling curves at a wall superheat of approximately 20 K in Fig. 4.27. The values at CHF of all measured quantities for both heater configurations and their relative differences are summarized in Tab. 4.3. At the point of CHF, the morphology of the two-phase mixture close to the wall is different for each respective heater configuration. Void fraction and ligament sizes at CHF are significantly higher but the void frequency at CHF is considerably lower for the wall-mounted copper heater in comparison to the single-rod copper-coated stainless steel heater.

Table 4.3: Measured quantities at CHF for the wall-mounted copper heater (WH) and the single-rod copper-coated stainless steel heater (RH).

Quantity	WH	RH	Relative change
$\dot{q}$	$259.3\,\text{kW}\,\text{m}^{-2}$	$148.1\,\text{kW}\,\text{m}^{-2}$	$+75.1\,\%$
ΔT_{sup}	$38\,\text{K}$	$27\,\text{K}$	$+40.7\,\%$
α	$71.2\,\%$	$64.9\,\%$	$+9.7\,\%$
f_{lig}	$515\,\text{Hz}$	$674\,\text{Hz}$	$-23.6\,\%$
l_{lig}	$1.22\,\text{mm}$	$0.61\,\text{mm}$	$+100\,\%$

For the wall-mounted copper heater, the transition to fully-developed film boiling could be recorded. At CHF, ligament sizes grow exponentially until a maximum ligament size of approximately 2.5 mm is reached. The measured void fraction and void frequency rapidly decrease as the boiling activity breaks down and the vapor film forms. In the film, values of α are expected to be close to 100 %. This indicates that even at 100 μm away from the wall, the fiber-optic microprobe is located outside of the vapor film.

Remarkably, the measured data of the void phase for a given wall superheat along the boiling curve up to CHF is nearly identical between the two heater configurations. The boiling process in the immediate vicinity of a heated surface appears to follow a universal evolution governed by wall temperature independently of the thermal properties of the heater substrate, if surface properties are kept identical. Despite the common evolution of the void morphology along the boiling curve, the wall-mounted copper heater exhibits a significantly higher stability limit of the boiling process. In the following, the data is therefore discussed with regard to two questions:

1. If the boiling process follows a universal evolution during stable boiling in the nucleate boiling regime, is there a set of universal governing parameters, which can be used to accurately correlate the entire boiling curve?

2. Are there similarities between the observed void behavior during the critical heat flux transient and literature and is there a common criterion at the stability limit of the boiling process, for which the breakdown of heat transfer is triggered?

4.3.3 Stable Boiling in the Nucleate Boiling Regime

For a unifying heat transfer model, the main modeling parameters must be the same for both pool boiling and flow boiling. If the experimental validation is considered an essential part of model development, experimentally accessible parameters have to be modeled. For pool boiling, experiments have shown that total heat flux is governed by both microlayer evaporation at the triple-phase contact line as well as single-phase liquid conduction [25]. Microlayer evaporation has been shown to be experimentally accessible through the void frequency measured by fiber-optic microprobes [23, 159]. It has been postulated by Lüttich et al. [30, 34] and Auracher et al. [30, 34] that the contact line density at the heater surface might be a sufficient measure for the contribution of the boiling activity on overall heat transfer along the entire boiling curve. This hypothesis is validated for subcooled flow boiling in the following.

4.3.3.1 Fiber-Optic Microprobe Data Measured Close to a Boiling Surface

Lüttich et al. [23, 159] showed that the density of the triple-phase contact line L_i on a heater surface can be directly measured by fiber-optic microprobes. In [23], Lüttich et al. used multi-phase flow averaging theory to show that boiling is an ergodic process. The ergodicity assumption links a geometric view of the two-phase flow to experimental probing techniques: Observing a sufficient number of void structures at a specific point at or very close to the surface over a certain period of time will not differ from observing a representative number of void structures distributed across the same surface. The time-averaging inherent to locally obtained experimental data can therefore be considered equal to space-averaged experimental data. With this, the authors found that the triple-phase contact line density L_i can be expressed using the void frequency f_{lig} measured by fiber-optic microprobes according to Eq. (4.7)

$$L_i = C_1 \frac{N_{\text{lig}}}{\Delta t} = C_1 f_{\text{lig}} \tag{4.7}$$

In this equation N_{lig} is the number of void ligaments detected during time interval Δt and C_1 is a characteristic constant with unit $\text{s}\,\text{m}^{-1}$ relating the time time and length scales of the process. Lüttich et al. [23, 159] proposed a new boiling heat transfer correlation for pool boiling according to Eq. (4.8).

$$\dot{q}_{\text{evap}} = C_2 \Delta T_{\text{sup}} f_{\text{lig}} \tag{4.8}$$

In this equation, C_2 is a constant with unit $\text{J}\,\text{m}^{-2}\,\text{K}^{-1}$ and $\Delta T_{\text{sup}} = T_w - T_{\text{sat}}$ implicitly introduces a dependency on the Jacob number Ja to the correlation.

$$\text{Ja} = \frac{\rho_l c_{\text{p,l}} \Delta T_{\text{sup}}}{\rho_g \Delta h_{\text{evap}}} \tag{4.9}$$

By fitting C_2 to experimental data, Lüttich et al. were able to correlate their measured boiling curve with high accuracy. Eq. (4.8), as derived and described in more detail in [23], suggests that the void frequencies measured close to the heated surface using a fiber-optic microprobe are directly related

to the contribution of the boiling process to overall heat transfer along the entire boiling curve. The applicability of this concept to subcooled flow boiling will be shown in the following.

4.3.3.2 Correlation of Measured Heat Flux with the Triple-Phase Contact Line Density in Subcooled Flow Boiling

For subcooled flow boiling overall heat flux is the superposition of many individual heat transfer phenomena [18]. In a simple approximation, only the heat transfer due to forced liquid convection and the evaporation heat flux have to be considered [186]. In the following, the overall heat flux was correlated with experimental data according to Eq. (4.10). For the nucleate boiling regime, $\dot{q}_{\mathrm{conv,l}}$ was extrapolated according to Sec. 4.3.2.1 from the measured heat flux due to single-phase convection and $\dot{q}_{\mathrm{evap}}$ was calculated based on measurement data from the fiber-optic microprobes according to Eq. (4.8).

$$\dot{q} = \dot{q}_{\mathrm{conv,l}} + \dot{q}_{\mathrm{evap}} = \dot{q}_{\mathrm{conv,l}} + C_2 \Delta T_{\mathrm{sup}} f_{\mathrm{lig}} \tag{4.10}$$

The applicability of Eq. (4.10) to flow boiling data was tested with the heat flux and void data presented in Fig. 4.27 and Fig. 4.29. For both heater configurations the entire boiling curve up to CHF can be correlated with remarkable accuracy, as shown in Fig. 4.30.

The correlation coefficient R for the correlated boiling curve up to CHF is $R_{\mathrm{WH}} = 0.9952$ and $R_{\mathrm{RH}} = 0.9915$, respectively. This indicates a nearly direct correlation for both geometries. The maximum deviation of the correlated heat flux from the measured heat flux up to CHF is $\Delta \dot{q}_{\mathrm{WH}} = 28.8\,\mathrm{kW\,m^{-2}}$ and $\Delta \dot{q}_{\mathrm{RH}} = 9.7\,\mathrm{kW\,m^{-2}}$, which is very small considering that each respective boiling curve was fitted with a single parameter. The approach is limited to single-phase convection and the nucleate boiling regime. After the vapor film formation, fiber-optic microprobes positioned at $y = 100\,\mu\mathrm{m}$ are located outside of the vapor film for a wide range of mass fluxes and subcoolings as seen in [4] and the void profiles presented in Appendix C. Hence, using the fiber-optic microprobe data from this experimental setup to correlate film boiling heat flux is not possible.
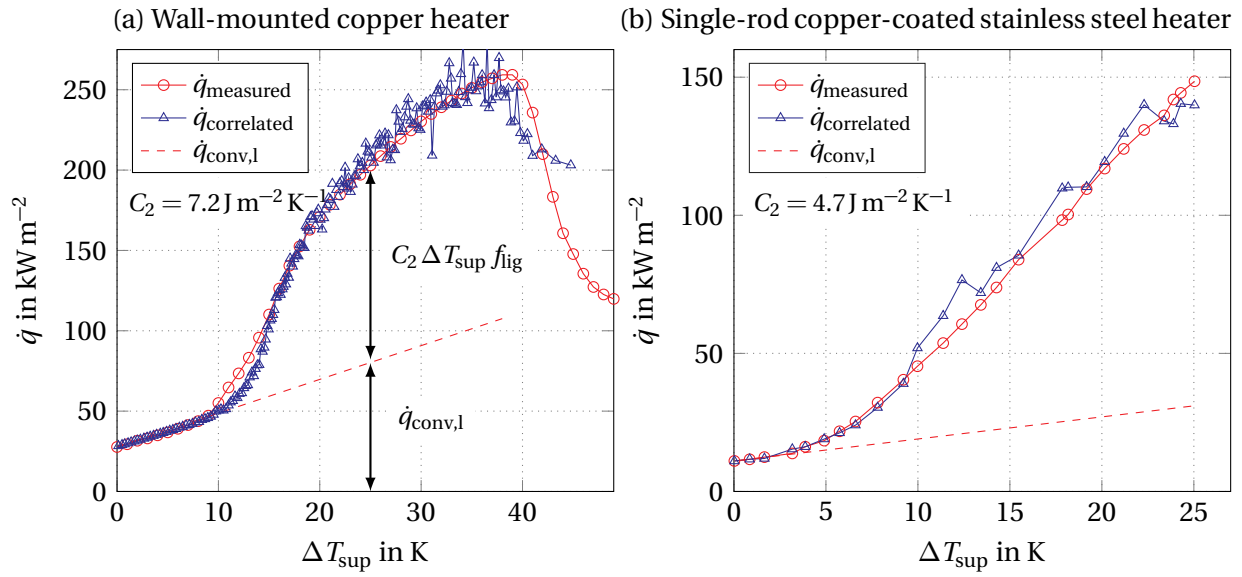
Figure 4.30: Comparison between correlated and measured boiling curves for both heater configurations for $G = 1000\,\mathrm{kg\,m^{-2}\,s^{-1}}$ and $\Delta T_{\mathrm{sub}} = 13\,\mathrm{K}$.

To check the universal applicability of the concept, further experiments were conducted for other mass fluxes and subcoolings for both heater configurations. Fig. 4.31 shows the data from these experiments displayed on the left ordinate plotted over the wall superheat normalized to the wall superheat at CHF. It can be seen that for a wide range of mass fluxes and subcoolings the correlated boiling curves match the measured boiling curves very well. Values for the fitting parameter C_2 were in the range of $1.3\,\mathrm{J\,m^{-2}\,K^{-1}}$ - $7.2\,\mathrm{J\,m^{-2}\,K^{-1}}$ with an average value of $4.8\,\mathrm{J\,m^{-2}\,K^{-1}}$. It can be seen in the data in [4] and in the void profiles in Appendix C that void frequencies measured close to the heater surface show a steep gradient towards the wall. Seemingly minor variations in the position of the fiber-optic microprobes relative to the heater surface between individual experiments can result in a large difference in detected void ligaments per second and therefore strongly influence the value of C_2. Additionally, the observed fluctuation might also occur because second order effects are consolidated in C_2. Future experiments with even better positioning accuracy of the fiber-optic microprobes are needed to provide more insight into the nature of C_2.

Obviously, the approach by Lüttich et al. [23, 159], which has been shown here to be applicable to subcooled flow boiling, does not allow for the predic-
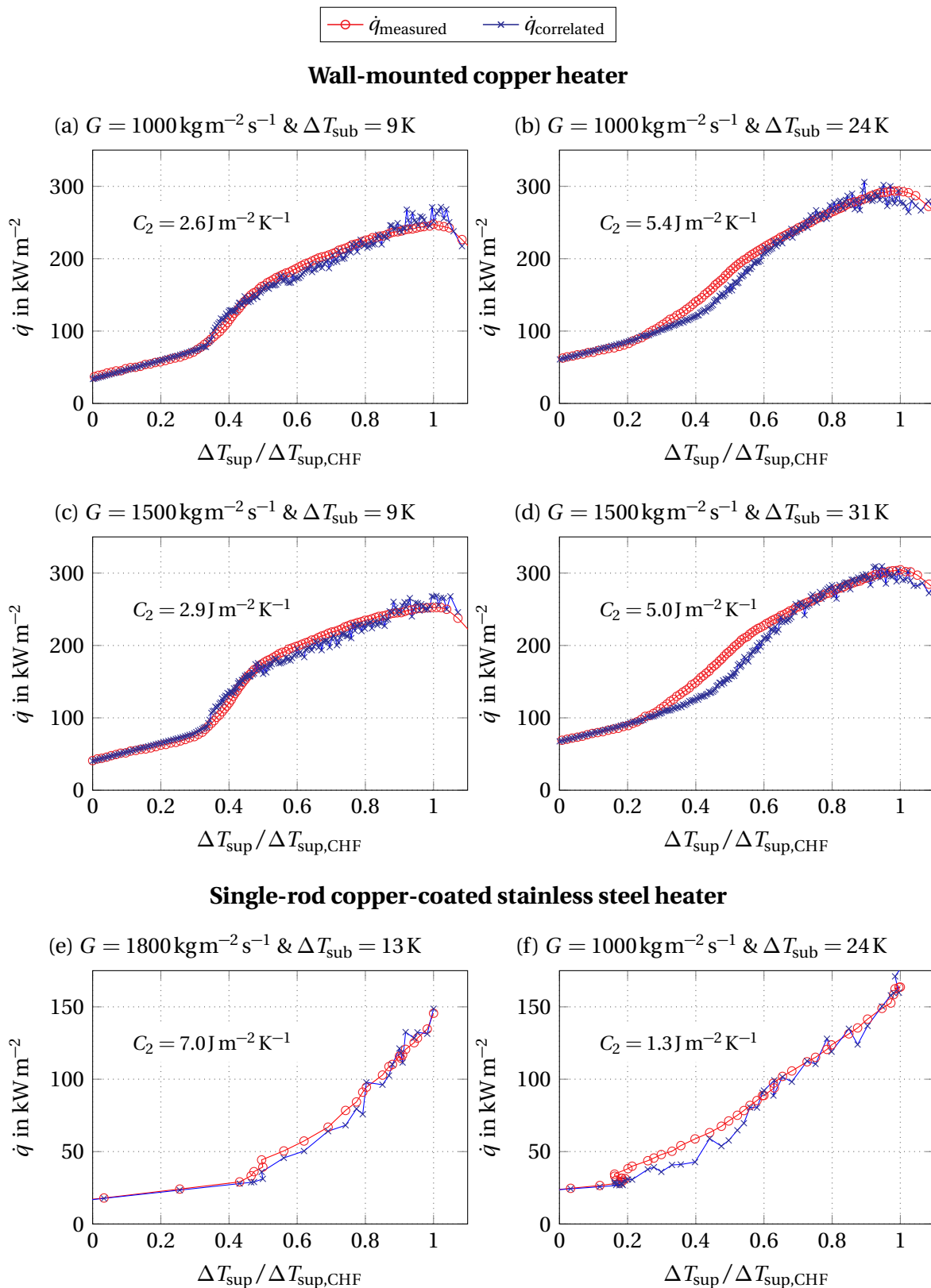
Figure 4.31: Comparison between measured and correlated boiling curves for both heater configurations for different mass fluxes and subcoolings.

tion of the entire boiling curve. It merely correlates experimentally obtained two-phase flow parameters with heat flux. These parameters are the result of the complex interaction between the two-phase mixture, the heater substrate and its surface properties during boiling. By using existing experimental data, the boiling curves for two independent heater configurations with different geometries and made of different substrates were found to correlate very well with the extrapolated heat flux from single-phase convection and the interfacial contact line density. This supports the hypothesis of Lüttich et al. [23] that models based on the triple-phase contact line density L_i will likely be superior to models employing other two-phase flow parameters such as void fraction on the heater surface.

This arguably is the case for both the model for quantitative prediction of critical heat flux initiation in pool and flow boiling by Ding et al. [19] and the new modeling approach for the prediction of CHF in multi-phase CFD by Baglietto et al. [18, 120]. Both concepts are based on the description of void structures on or very close to the heater surface. They are therefore implicitly dependent on L_i, which provides further leverage to their conceptual superiority compared to the macrolayer approaches in the classic mechanistic models.

4.3.4 Critical Heat Flux Transient

Concluding this chapter, the occurrence of critical heat flux and the associated breakdown of heat transfer will be investigated in more detail. In the following, the feasibility of a dry-spot CHF mechanism for subcooled flow boiling is assessed and a stability limit for the boiling process based on the experimental data is identified.

4.3.4.1 Previously Developed Phenomenological Concept for the Critical Heat Flux Process in Flow Boiling

The author of this work has previously co-developed a phenomenological concept for the CHF process in flow boiling [10], which was subsequently refined by Bloch [16]. The concept was based on the assessment of the valid-

ity of the CHF trigger mechanisms of the bubble crowding model, the sublayer dry-out model and the interfacial lift-off model. The trigger mechanisms of these models were compared with data from own experiments close to CHF using a complementary measurement approach consisting of high-speed videometry, shadowgraphy, particle image velocimetry, digital holographic interferometry and fiber-optic probes. Based on these experiments, the phenomenological mechanism depicted in Fig. 4.32 was proposed.

At CHF, the coalesced layer contracts into the bubbly sublayer, exceeding a critical void fraction and further increasing bubble sizes and velocities. This finally results in the blockage of liquid access to the heater surface, causing the transition to film boiling.

The relevant bubbly sublayer moves at higher velocities compared to the coalesced layer due to higher void fractions. Due to this velocity gradient, vapor tends to coalesce into this layer, further increasing void fraction and velocity.

A relevant bubbly sublayer is present in the immediate vicinity of the heater surface beneath highly coalesced vapor clots. It is only marginally influenced by bulk flow turbulence and contains the actual CHF trigger mechanism.

A coalesced layer forms above the heater surface.

Void fraction increases steadily towards the heater surface. Ligament velocity increases towards the heater surface, due to buouyancy.

Figure 4.32: Previously developed phenomenological concept of the CHF process for vertical subcooled flow boiling. Adapted from [10].

By means of shadowgraphy, digital holographic interferometry and particle image velocimetry, it was shown that significant transport of subcooled liquid towards the heater occurs in the wake of bigger void agglomerations. The thickness of the dense vapor layer above the heater surface was investigated with high-speed videometry. Through experiments at different subcoolings and with artificially induced turbulence, it was shown that a relative reduction of the thickness of this vapor layer resulted in approximately the same relative increase of CHF. It was argued that the actual trigger mechanism of CHF occurs in a sublayer close to the wall, which is largely unaffected by the bulk flow morphology. This was supported by preliminary measurements with a fiber-optic probe placed above the heater surface at its downstream end. A contraction of the void layer in the bulk flow observed by fiber-optic probes positioned at distances of 2 mm - 6 mm from the heater wall substantiated this supposition. The fiber-optic probes had a core diameter of 200 μm. This inhibited accurate measurements in the immediate vicinity of the heated wall, due to the sixteen-times-larger projected detection area compared to the fiber-optic microprobes used in the present study. By extrapolating the velocity profile of the void phase measured in the bulk flow by shadowgraphy image velocimetry and particle image velocimetry, void structures at the heater surface at CHF were estimated to be approximately 4.8 mm in size. A strong velocity gradient of the void phase towards the heater wall up to a wall distance of approximately 3 mm - 4 mm was observed. It was argued that this is an important part of the CHF process as it leads to the transport of bulk void into the layer closer to the wall according to Tomiyama et al. [178].

4.3.4.2   Dry-Spot Dynamics in Pool Boiling

Large consensus has been reached on dry-spot re-wettability being the limiting condition for heat transfer in pool boiling. Based on the literature presented in Sec. 2.4.3, the general behavior of dry-spots on the heater surface close to CHF for pool boiling can be summarized as follows:

- Below CHF there exist quenchable residual void structures from previous nucleation events on the heater surface. These structures increase in size as heat flux increases.

- Close to CHF, dry-spots form due to (a) a local temperature increase above the Leidenfrost temperature or (b) the hydrodynamic limitation of liquid supply by increased nucleation events close to the triple-phase contact line.

- The dry-spot lifetime increases as CHF is approached. After exceeding a certain lifetime during which the dry-spots are not quenched, they expand rapidly over the heater surface. CHF is triggered. Area-averaged void increases. Nucleation site activity remains high in wetted regions.

4.3.4.3 Refined Concept for the Critical Heat Flux Process at the Wall in Flow Boiling

The findings of Bloch et al. [10, 16] are partly confuted and partly complemented by the data of this study. No evidence of the existence of a critical void fraction in the region close to the wall due to a contraction of the postulated coalesced layer above the heater surface was found. Instead, the small increase in void fraction from FDB to CHF at the lower and middle measurement positions as shown in Fig. 4.2 suggest that void fraction close to the boiling surface does not significantly contribute to the occurrence of CHF. As seen in Fig. 4.3 and postulated in [10], a high drift flux with a peak at approximately $y = 1\,\mathrm{mm}$ is present above the heater surface. A steep velocity gradient was observed in the layer close to wall. The velocity of the void phase decreases towards the wall below a certain wall distance. This complements the observed increase of void velocity from the bulk flow towards the heater wall as shown in [10, 16]. No significant increase in void fraction close to the wall was observed between FDB and CHF for the majority of all experiments. The data of this study therefore confutes the blockage of liquid at the boundary between the coalesced layer and the relevant sublayer, which was postulated by Bloch [16]. However, the data presented in Fig. 4.2 provides leverage to the existence of a relevant bubbly sublayer. Between a wall distance of $y = 200\,\mu\mathrm{m}$ and $y = 1000\,\mu\mathrm{m}$, the void frequency at CHF is homogeneous. At a distance of $y \leq 200\,\mu\mathrm{m}$, void frequencies at CHF begin to increase rapidly towards the wall. The same qualitative behavior was observed for multitude of operating conditions as illustrated in Appendix C. This suggests that there exists a layer

in the immediate vicinity of the boiling surface in which the void morphology at CHF is fundamentally different from the bulk flow.

Additionally, the data of the wall-mounted copper heater presented in Fig. 4.4 and the data of the single-rod copper-coated stainless steel heater presented in Fig. 4.8 and Fig. 4.9 correspond rather well with the reported dry-spot behavior at CHF in pool boiling. As heat flux increases, a large increase in the size of void structures can be observed in the immediate vicinity of the boiling surface. A consistently high void frequency at CHF provides leverage to a possible hydrodynamic limitation of the liquid supply to larger residual void structures by increased nucleation at their triple-phase contact line. Moreover, the contact time of void structures increases by 300 % between the onset of boiling and CHF. After reaching a contact time of approximately 1.5 ms, the average void ligament size increases exponentially. At the same time, void fraction shows a distinct peak at all measurement positions along the direction of flow shortly after CHF before rapidly decreasing as the film is formed and the heat transfer breaks down. Based on these similarities, a dry-spot mechanism at CHF appears viable for flow boiling on heaters with technically relevant thickness.

To investigate whether this behavior can be considered universal, additional experiments at different mass fluxes and subcoolings were conducted with fiber-optic microprobes positioned at approximately 100 µm above the surface of the wall-mounted copper heater. For each of these experiments, a full boiling curve from single-phase convection to fully-developed film boiling was recorded. The data from these experiments is shown in Fig. 4.33 plotted over the normalized wall superheat $\Delta T_{\mathrm{sup}} / \Delta T_{\mathrm{sup,CHF}}$. The observed behavior is consistent with the previous measurements:

- For all operating conditions, void fraction shows a distinct peak after CHF before rapidly decreasing as the vapor film is formed.

- A decrease in effective heat transfer coefficient is evidenced by a change in slope for each boiling curve after the onset of boiling. This point occurs close to the maxima of the measured void frequency for all operating conditions.

- Ligament velocity increases continuously towards CHF. At CHF, the velocity of the void phase quickly increases.

- Ligament sizes slowly increase after the onset of nucleate boiling. They begin to grow at increasing rates once the point of peak frequency has been reached. CHF marks the onset of an exponential growth of void structures.

- Contact times show a large increase between the onset of nucleate boiling and CHF for all operating conditions. At CHF, contact times increase exponentially as surface heat flux decreases.

- There exists a distinct maximum in void frequency, which is observed for all operating conditions. Ligament sizes at peak frequency are marginally bigger at lower subcooling. After reaching the maximum frequency, the void frequency steadily declines until CHF.

Combining the findings of Bloch et al. [10, 16], the reported dry-spot dynamics in pool boiling and the data of this study, the following extended and refined phenomenological concept of the CHF process in vertical subcooled flow boiling can be formulated. Fig. 4.34 shows a graphical representation of the proposed mechanism.

Onset of boiling: At the onset of boiling, the heater quickly becomes covered with discrete bubbles forming on active nucleation sites. Bubble frequencies rise until a maximum attainable bubble size is reached. After this, void frequency gradually declines as void structures increase in size and temporarily deactivate neighboring nucleation sites. This can equally be seen in Fig. 4.4d and Fig. 4.4f for the wall-mounted copper heater and in Fig. 4.8 for the single-rod copper-coated stainless steel heater.

FDB: Void fraction profiles with a peak close to the wall develop above the heater surface. This can be seen in Fig. 4.2 and the figures in Appendix C for all measurement positions along the direction of flow for the wall-mounted copper heater. There exists a shear lift force due to the steep velocity gradient close to the wall seen in Fig. 4.3 and Fig. 4.7, which facilitates bubble departure. Void ligament size increases and subsequently the intermittency at the heater surface decreases (Fig. 4.4d and Fig. 4.4f as well as Fig. 4.8). The effective heat transfer coefficient decreases due to less stirring of the liquid on the surface by departing bubbles. This effect occurs first at $t \approx -50\,\text{s}$ in Fig. 4.4b
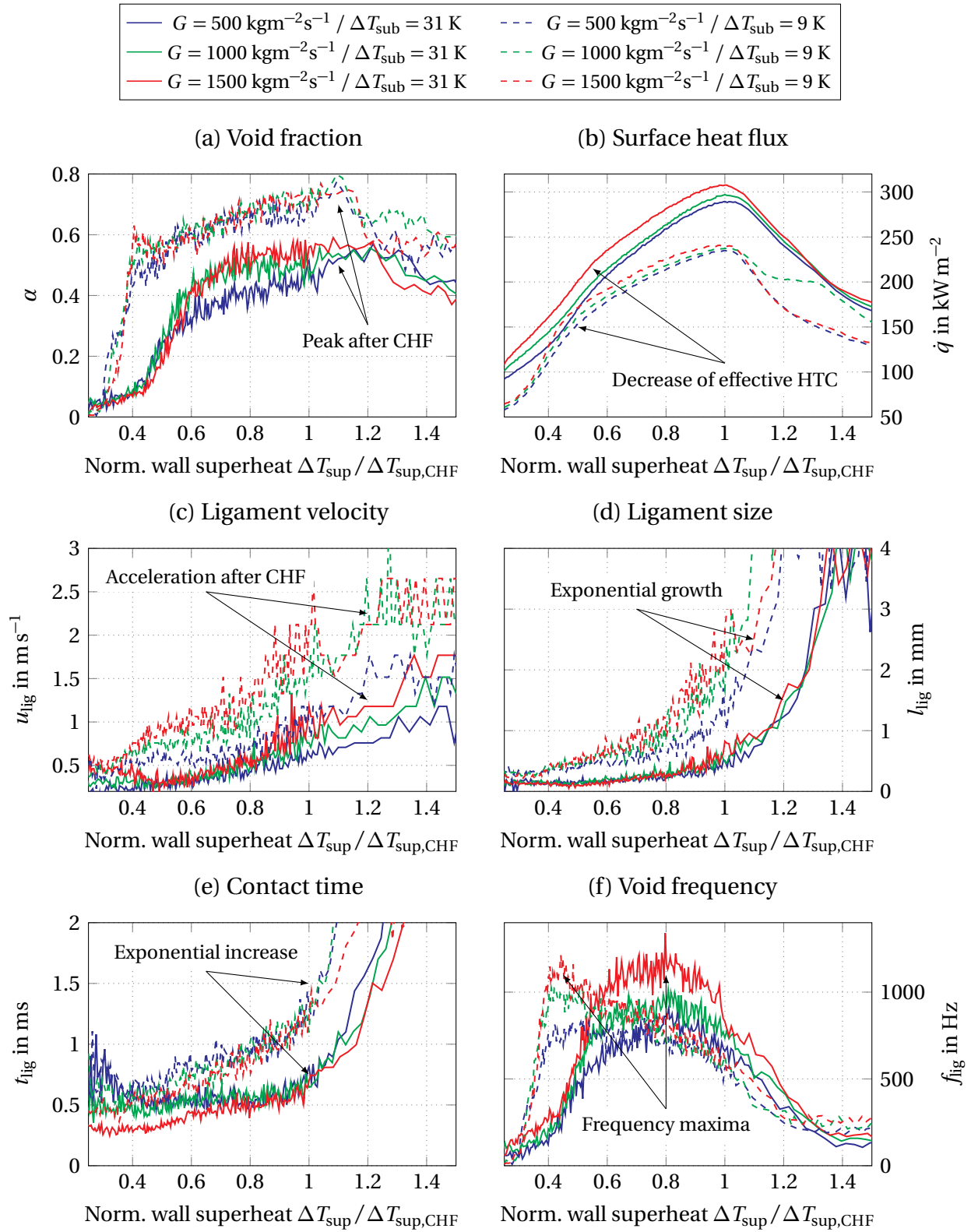
Figure 4.33: Evolution of the morphology of the void phase along the boiling curve beyond critical heat flux for six operating conditions at a wall distance of $y = 100\,\mu$m at the middle measurement position of the wall-mounted copper heater.

and was observed for both heater geometries as evidenced by Fig. 4.27. Because the average size of void structures is still small and void frequencies are at their peak, it is assumed that no significant residual void remains on the heater surface after bubble departure.
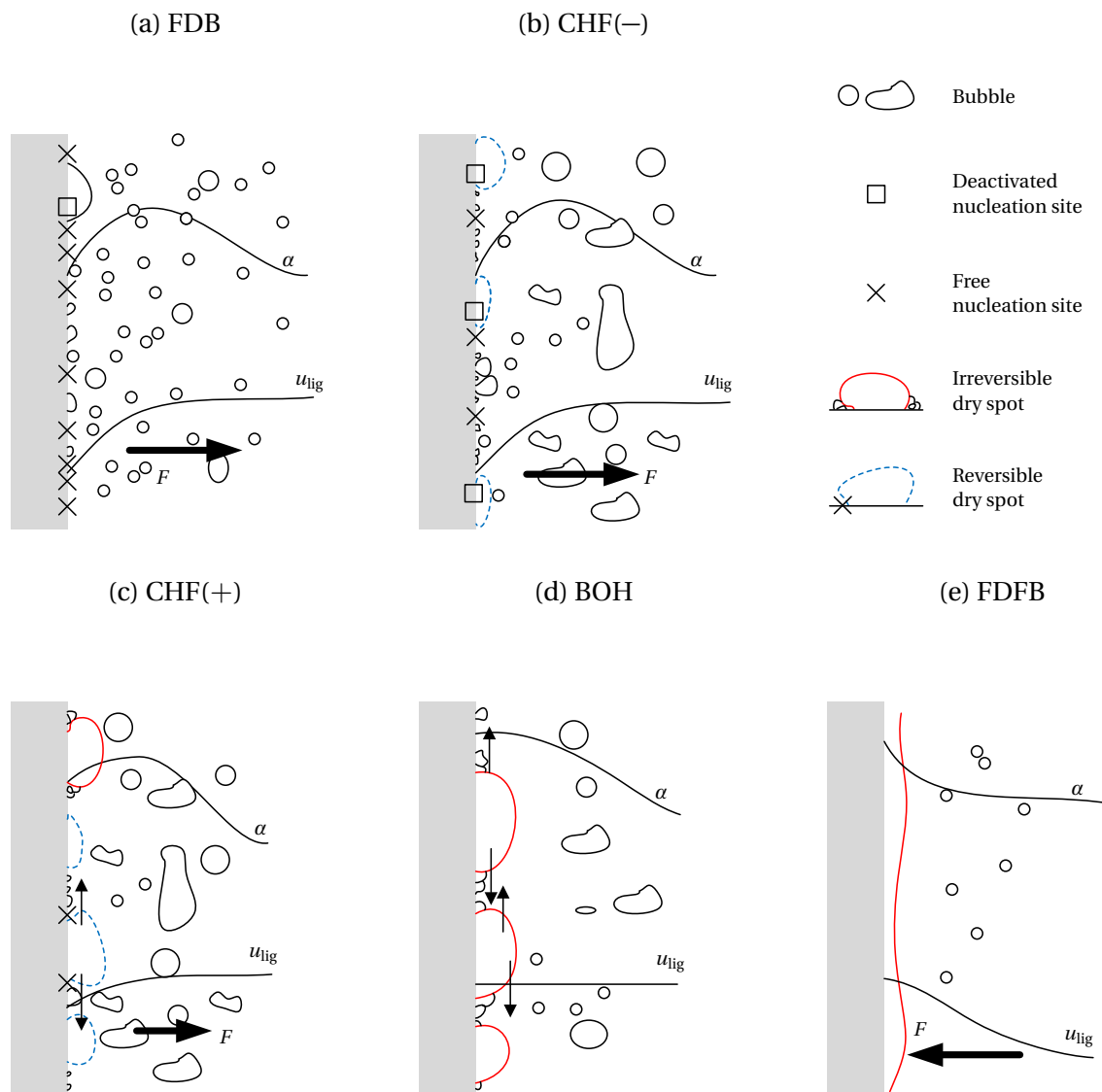
Figure 4.34: Phenomenological conceptualization of the development of void morphology along the boiling curve. (-) and (+) in this figure denote the time before and just after a certain point on the boiling curve. Profiles for α and u_{liq} not to scale.

CHF(-): More void is generated as heat flux increases. The sublayer as postulated in [10] forms, as evidenced by the steep increase of void frequency below a wall distance of $y \approx 200\,\mu\text{m}$ seen in Fig. 4.2 for the wall-mounted

copper heater. This increase was observed similarly albeit less distinctly for the single-rod copper-coated stainless steel heater as shown in Fig. 4.7. Close to CHF, the void structures on the heater surface begin to grow. Concurrently, the dry time at the heater starts to increase significantly. Towards CHF, dry times at the heater surface, ligament sizes and ligament velocities grow at increasing rates, which can be seen in Fig. 4.4c to Fig. 4.4e and in Fig. 4.5. The formation of first reversible dry-spots, which remain attached to the heater surface for a short period of time before being fully rewetted, is postulated to occur.

CHF: At CHF, the qualitative morphology of the flow near the wall at CHF is still unaffected by the onset of an exponential growth of void structures at the wall. This is seen in Fig. 4.4c. No sudden change in flow topology can be observed at CHF. However, as seen in Fig. 4.4d, a similar average dry time per void structure is reached for each measurement position along the direction of flow of the wall-mounted copper heater. Upon reaching this dry time, less heat is removed by the boiling process than provided by the heater. The effective heat transfer coefficient further decreases due to the increased formation of irreversible dry-spots on the heater surface. This assumption is supported by the rapid growth of void structures on the heater surface due to the rise in heater temperature and increased coalescence seen in Fig. 4.4d. This effect was equally observed for the single-rod copper-coated stainless steel heater, as shown in Fig. 4.9.

CHF(+): The morphology of the flow close to the wall begins to change. The velocity of void structures on the heater surface increases and the velocity gradient at the wall becomes flatter. This can be seen by the gradual convergence of void velocities in Fig. 4.5. Subsequently, the shear lift force pulling void away from the heater surface becomes weaker. Significant boiling activity persists as more nucleation sites are activated by increasing wall temperatures. Quenching of reversible dry-spots is further inhibited by many small bubbles in the surrounding of bigger void structures. This is supported by consistently high void frequencies around critical heat flux at $t = 0\,\mathrm{s}$ in Fig. 4.4f and Fig. 4.9. Dry-spots grow in lateral direction and significant coalescence is expected to occur. Ligament sizes and dry times at the surface begin

to increase exponentially, which further amplifies the process (Fig. 4.4d and Fig. 4.4e and Fig. 4.9c).

BOH: The formation of a continuous vapor film on the surface begins. Although no contraction of the coalesced layer into the relevant sublayer was observed as postulated in [10], void fraction at the wall increases. This is evidenced by a distinct peak in void fraction at all measurement positions along the direction of flow after CHF in Fig. 4.4a, Fig. 4.9a and Fig. 4.33a. The velocity gradient at the wall has vanished, as seen in Fig. 4.5 at $t \approx 4\,\mathrm{s}$ after CHF and in Fig. 4.9d at $t \approx 5\,\mathrm{s}$ after CHF. Bubble departure becomes inhibited. It is assumed that at this point, irreversible dry-spots merge on the heater surface, which is supported by the peak in void ligament sizes and void fraction at BOH observed for both heater configurations. This can be seen in Fig. 4.4d and Fig. 4.33a for the wall-mounted copper heater and in Fig. 4.9a for the single-rod copper-coated stainless steel heater. Heat transfer breaks down (Fig. 4.4b) as the majority of active nucleation sites are covered by the coalesced void structures and void frequency rapidly decreases, as seen in Fig. 4.4f and Fig. 4.9b.

FDFB: The heater is covered by a wavy vapor film. Void fraction peaks at the wall and the velocity gradient has inverted.

4.3.4.4 The Stability Limit of the Boiling Process

In recent years, a large consensus has been reached regarding the initiation of the boiling crisis in pool boiling. As illustrated in Sec. 2.4.3, the formation of irreversible dry-spots on the heater surface in conjunction with a rapid increase in surface temperature and the subsequent lack of rewetting is considered to be the governing mechanism leading to the breakdown of heat transfer in pool boiling. As argued above, the quantitative experimental data of this study provides evidence that a dry-spot CHF mechanism is present in subcooled flow boiling on heaters with technically relevant thickness as well. Despite the solid quantitative experimental foundation, the general description of the dry-spot CHF process is of phenomenological nature and so far in

general lacks a clear explanation of why dry-spots begin to form on the heater surface [30]. The proposed refined CHF process at the wall in flow boiling as introduced above is no exception. The cause for the occurrence of CHF remains unclear. In the following, a common stability limit for the boiling process is therefore identified.

Many studies on dry-spot phenomena were conducted using infrared thermometry to measure the surface temperature and heat flux distribution of very thin heaters. This approach disregards the effects of the thermal properties of the heater substrate. The majority of these studies found a single irreversible dry-spot to trigger the breakdown of heat transfer. However, with increasing thickness of the heater, the supposition that the occurrence of a single irreversible dry-spot causes the transition to film boiling looses its plausibility [34]. Blum et al. [187] found that a dry-spot expansion is accompanied by a temperature wave propagating in the heater substrate beneath the boiling surface. For a copper heater with a wall thickness of 10 mm, an extension of a single irreversible dry-spot of more than 8 mm would be required to trigger a temperature wave high enough to prevent the rewetting of the surface. This is approximately one order of magnitude bigger than the average void ligament sizes at CHF observed in the present study, as shown in Fig. 4.29c. The size of dry-spots necessary to trigger CHF diminishes when an ensemble of dry-spots on the heater surface is considered [34]. However, Tab. 4.3 illustrates that no single critical parameter in the void data can be found, which is the same at CHF for the two heater configurations. Therefore, the limiting mechanism of the boiling process must lie in the transient thermal interaction of the heater substrate with the two-phase mixture at the wall.

The Fourier number $\mathrm{Fo} = a\,t\,/\,l^2$ may be physically interpreted as the rate of heat conduction to the rate of change of thermal energy inside a solid body [36]. The rate of heat conduction can be expressed as $\dot{Q} = \lambda l^2 \Delta T\,/\,l$. The rate of change of thermal energy in the heater substrate may be expressed as $\dot{E} = \rho\,l^3 c \Delta T\,/\,t$. The ratio of the rate of heat conduction to the rate of change of thermal energy in the heater substrate can then be expressed by Eq. (4.11).

$$\frac{\dot{Q}}{\dot{E}} = \frac{\lambda\,t}{\rho\,c\,l^2} = \frac{a\,t}{l^2} = \mathrm{Fo} \tag{4.11}$$

F O provides a measure of the effectiveness of heat conduction inside the heater substrate below the boiling surface, which mitigates local temperature gradients, in relation to the concurrent heat storage in the heater substrate. In the case of boiling, void ligaments of size l_{lig} interact with the heater substrate at the boiling surface during a characteristic time $t = 1/f_{lig}$. Using the experimental fiber-optic microprobe data, an instantaneous Fourier number at the heater surface can be defined according to Eq. (4.12).

$$\mathrm{Fo} = \frac{a}{f_{lig} l_{lig}^2} \tag{4.12}$$

Fig. 4.35 shows the evolution of the instantaneous Fourier number along the boiling curve for both heater configurations.
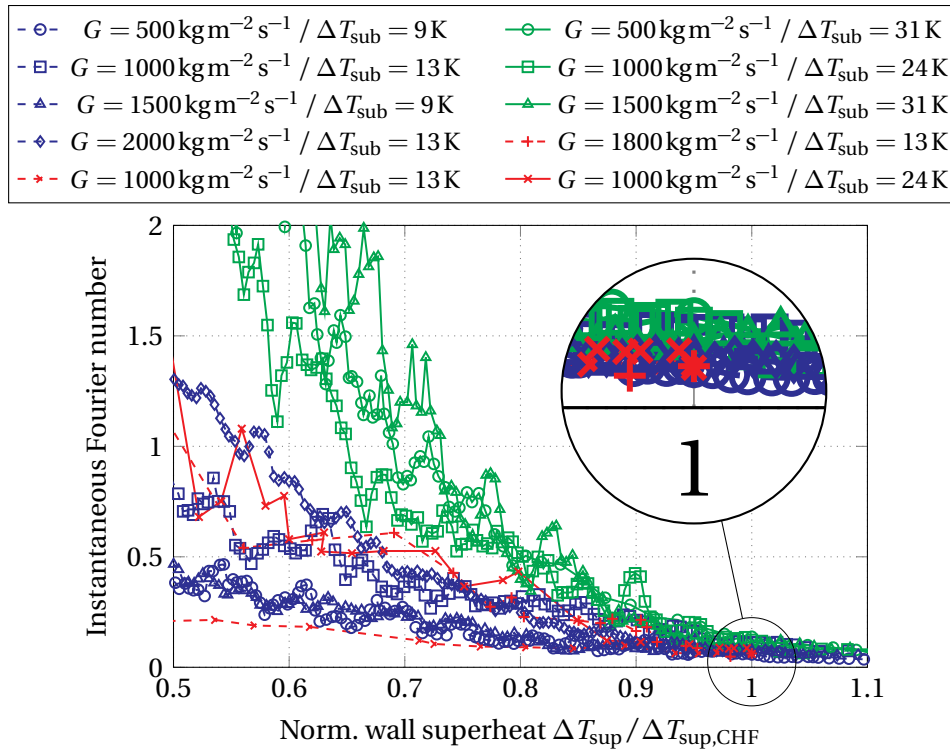
Figure 4.35: Evolution of instantaneous Fourier numbers along the boiling curve for the two heater configurations for all operating conditions. Red graphs denote experimental data from the single-rod copper-coated stainless steel heater.

For all operating conditions and heater configurations, the Fourier number at the surface follows a similar evolution. In the nucleate boiling regime after ONB, the Fourier number is large. This means that the rate of change of thermal energy in the heater substrate is much smaller than the rate of

heat conduction per average void structure. Subsequently, any heat stored in the heater substrate during the interaction of a void structure with the surface can be effectively distributed. As CHF is approached, Fourier numbers rapidly decrease because void structures on the heater surface grow in size due to increased coalescence. This poses an increasing heat transfer resistance between the heater substrate and the two-phase flow at the surface of the heater.

While the instantaneous Fourier numbers at the heater surface vary significantly in the nucleate boiling regime, a universal value range of $\mathrm{Fo} \approx 0.05 - 0.15$ is observed at CHF for all operating conditions and both heater configurations. This finding implicates that the time scales of the boiling process and their influence on transient heat conduction inside the heater substrate play a fundamental role in the initiation of the boiling crisis. The data suggests that the boiling process for Novec 649 remains stable until the average thermal diffusivity time $t_{\mathrm{diff}} = l_{\mathrm{lig}}^2 / a$ of the heater substrates becomes much larger than the average void ligament interaction time $t_{\mathrm{lig}} = 1 / f_{\mathrm{lig}}$ and the ratio of the two reaches a value of $t_{\mathrm{lig}} / t_{\mathrm{diff}} \approx 5\% - 15\%$. Upon reaching this value, local temperature gradients as a result of nucleation events at the surface cannot be distributed inside the theater substrate quickly enough anymore. The locally elevated heater temperature then prevents the rewetting of the residual dry-spots and CHF is triggered.

Chapter 5

Summary and Conclusion

In this study, synchronous and locally coupled measurements of heat flux, surface temperature and local parameters of the void phase were presented along the boiling curve for vertical subcooled flow boiling of the refrigerant Novec 649. Two heaters of technically relevant thickness made of two different heater materials but with identical surface characteristics were investigated in a square flow channel: a wall-mounted copper heater and a single-rod copper-coated stainless steel heater. This makes it possible to investigate the influence of the thermal properties of the heater substrate on the boiling process independently of nucleation site density and nucleation behavior. Data on the morphology of the void phase was obtained along the boiling curve beyond critical heat flux with miniaturized single-fiber and double-fiber microprobes. A high-accuracy traversing mechanism was used to position the fiber-optic microprobes relative to the surface of each heater.

Average boiling curves, void data profiles and time-resolved void data in the immediate vicinity of the boiling surface were presented for both heater configurations. Data was obtained from experiments with a mass flux of $1000\,\mathrm{kg\,m^{-2}\,s^{-1}}$. Inlet subcooling was kept constant at $13\,\mathrm{K}$. Void profiles were provided for three characteristic states along the boiling curve, which are fully-developed boiling, CHF and fully-developed film boiling. Where needed, additional experiments were conducted at other mass fluxes and subcoolings to support the analysis of the data.

Three established mechanistic models for the prediction of CHF in flow boiling were assessed with the experimental data: the bubble crowding model, the sublayer dry-out model and the interfacial lift-off model. First, their universal prediction accuracy was tested with a comprehensive data set of critical heat flux values obtained with the wall-mounted copper heater. Second, the validity of some of their core assumptions was assessed based on data from measurements with the fiber-optic microprobes. Although some as-

sumptions regarding the flow morphology at CHF seem reasonable, it was shown that none of the models are able to predict CHF for the experimental setup of this study.

It was found that the models lack the ability to account for important features of the boiling process and critical heat flux. For example, the thermal interaction between residual dry-spots and the heater surface as well as the wetting properties of the fluid are disregarded in these models, because of their focus on the macrolayer above the boiling surface. Next-generation mechanistic CHF models for the application in multi-phase CFD codes, based on more recent experimental data, attempt to circumvent these shortcomings. Subsequently, two next-generation modeling approaches were investigated in more detail. Their quantitative prediction accuracy could not be assessed, because no set of equations, which would allow for the reprogramming of the models, has been published yet. However, some parts of their physical foundation could be validated with the experimental data of this study. The key improvement of these approaches is the modeling of the interaction between nucleated void structures and the heater material. This was identified as key to the successful modeling of nucleate boiling at high heat fluxes. To substantiate the experimental foundation for the development and validation of current and future boiling models, data on the void morphology at the surface of heaters made of different materials is needed. Therefore, a detailed comparison and analysis of the experimental data from both heater configurations was conducted.

By comparing the data, it was shown that void fraction, void ligament frequency and void ligament size follow a similar evolution along the boiling curve for both heater configurations. It was argued that the contribution of the boiling process to overall heat transfer must therefore be nearly identical for the two heater configurations. Therefore, any difference in overall heat flux arguably arises from differences in the heat transfer due to single-phase liquid convection. It was also observed that the stability limit of the boiling process differs greatly depending on the heater substrate. No common value for any two-phase flow parameter could be identified, for which CHF is triggered for both heater configurations.

The experimental data was subsequently analyzed with respect to the following questions:

1. Is there a set of universal governing parameters, which can be used to accurately correlate the entire boiling curve?

2. Are there similarities between the observed void behavior during the critical heat flux transient and existing literature?

3. Is there a universal criterion at the stability limit of the boiling process, which triggers the breakdown of heat transfer?

Regarding the existence of a set of governing parameters for correlating boiling heat transfer, it was found that the boiling curve up to CHF can be correlated with high accuracy using the interfacial contact line density. This quantity was directly measured in the immediate vicinity of the boiling surface with fiber-optic microprobes. The finding supports the hypothesis from literature that boiling models based on the description of interfacial movement on the boiling surface are conceptually superior to models based on other two-phase flow parameters like for example void fraction on or close to the heater surface.

Regarding the similarities between the observed void behavior during the CHF transient and existing literature, it was shown that void behavior at the wall follows a similar evolution during the critical heat flux transient for a wide range of operating parameters. Several recurrent patterns were identified for both heater configurations. An exponential increase in bubble sizes and dry times in the immediate vicinity of the boiling surface was measured close to CHF. A gradual but fundamental change in flow topology occurred during the transition to film boiling. Approaching CHF, the void phase close to the heater surface is subjected to increased acceleration. It was concluded that this leads to the reversion of the direction of the shear lift force acting on the void structures close to the wall. It was argued that absolute void fraction close to the heater surface is presumably not the causative limiting factor for the boiling process. These findings were compared to the current understanding of the dynamics of dry-spot formation on the heater surface at CHF for pool boiling and a previously developed phenomenological concept for the CHF process in flow boiling. The previously published concept for the CHF process was partly confirmed and partly refuted by the experimental data of this study. Similarities were found between the data of this study and the reported behavior of dry-spots at CHF in literature. It is concluded that

a dry-spot mechanism at CHF also appears viable for flow boiling. A phenomenological extension of the dry-spot CHF mechanism to vertical subcooled flow boiling was developed.

Regarding the existence of a universal criterion describing the breakdown of heat transfer, instantaneous Fourier numbers were calculated along the boiling curve based on measurement data from fiber-optic microprobes. A universal value range for the instantaneous Fourier number on the heater surface of $0.05 - 0.15$ was found at CHF for a range of mass fluxes and subcoolings.

It is concluded that CHF therefore is the result of the complex interaction of the two-phase mixture with the boiling surface and the concurrent transient thermal response of the heater substrate. Void structures at the heater surface continuously interact with the heater substrate along the boiling curve in a way which eventually causes CHF. Critical heat flux is the outcome of the local feedback between the transient thermal response of the heater substrate and an ensemble of larger residual void structures on the heater surface. It is triggered when the thermal diffusivity time of the substrate becomes much larger than the average void interaction time with the heater surface. Hence, both the evolution of the two-phase flow at the wall, as well as the transient thermal response of heater substrate have to be modeled along the boiling curve to achieve a universal and predictive boiling model.

Appendix A

Physical Properties of Novec 649 in Comparison to Water

Table A.1: Main fluid parameters at saturation conditions for 1.15 bar of Novec 649 in comparison to water.

Quantity	Novec 649	Water	Unit
T_{sat}	325.9	376.8	K
Δh_{evap}	86.9	2247.1	kJ kg^{-1}
$c_{\text{p,l}}$	1121.45	4221.28	$\text{J kg}^{-1}\text{K}^{-1}$
$c_{\text{p,g}}$	908.9	2092.1	$\text{J kg}^{-1}\text{K}^{-1}$
ρ_{l}	1504.78	955.77	kg m^{-3}
ρ_{g}	14.21	0.67	kg m^{-3}
σ	10.8	72.8	mN m^{-1}
ν_{l}	2.834×10^{-7}	2.646×10^{-7}	$\text{m}^2\,\text{s}^{-1}$
λ_{l}	0.054	0.682	$\text{W m}^{-1}\text{K}^{-1}$
T_{crit}	441.81	647.10	K
p_{crit}	1.88	22.12	MPa

Appendix B

Boiling Curves Wall-Mounted Copper Heater
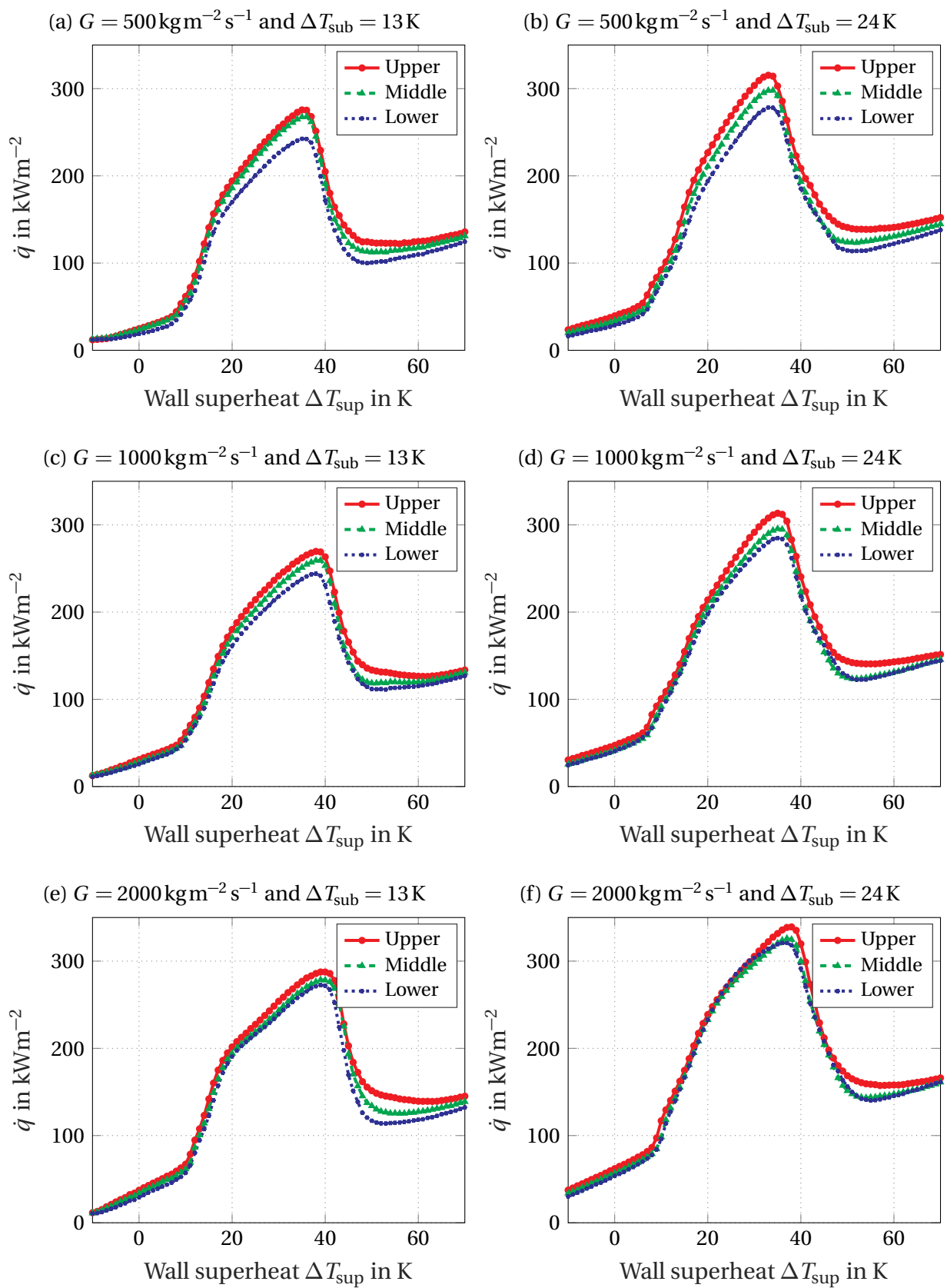
Figure B.1: Average boiling curves for six combinations of operating parameters.

Appendix C

Void Profiles Wall-Mounted Copper Heater
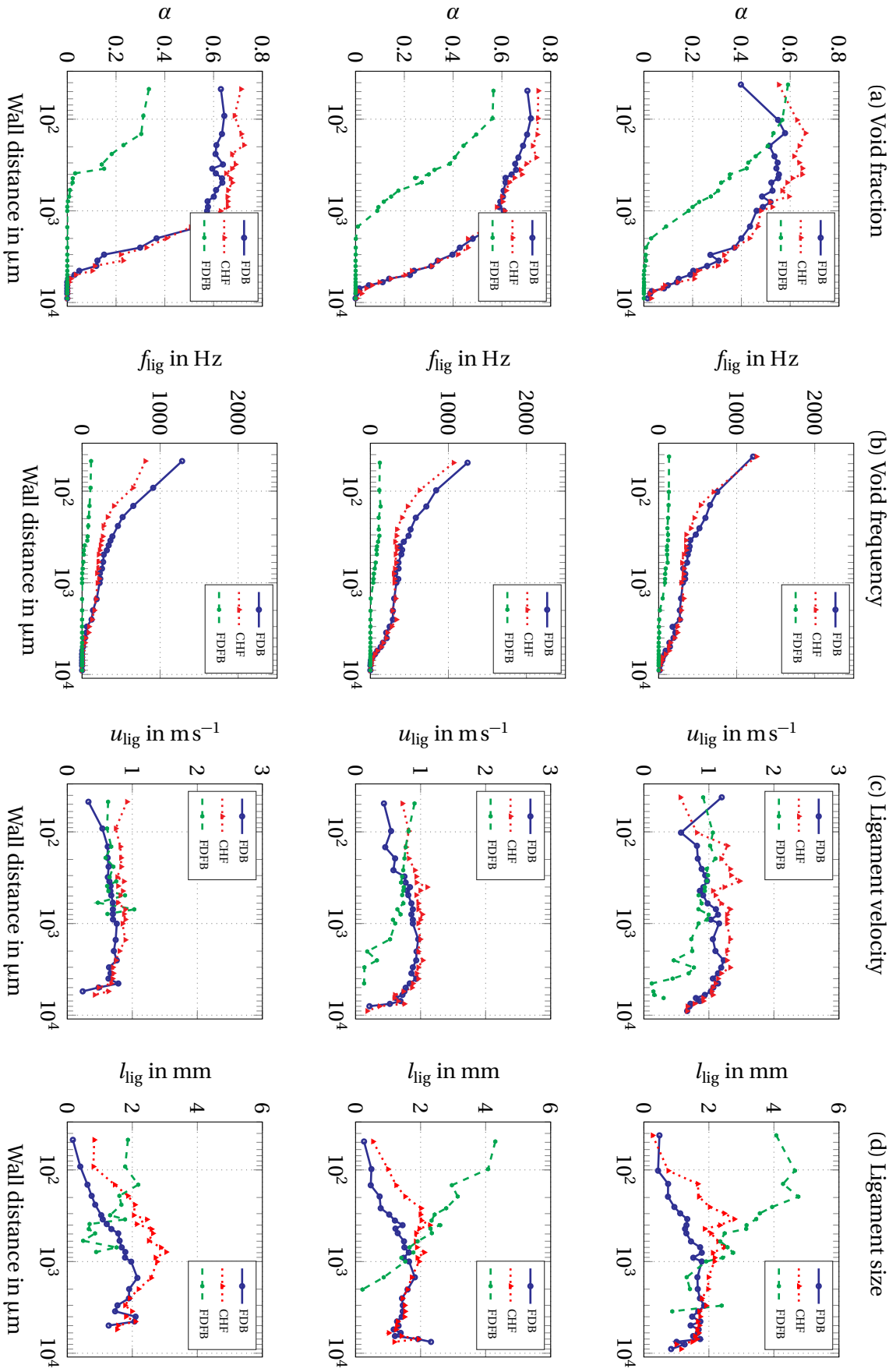
Figure C.1: Void profiles at the upper, middle and lower measurement position (top to bottom) for $G = 500\,\mathrm{kg\,m^{-2}\,s^{-1}}$ and $\Delta T_{\mathrm{sub}} = 13\,\mathrm{K}$.
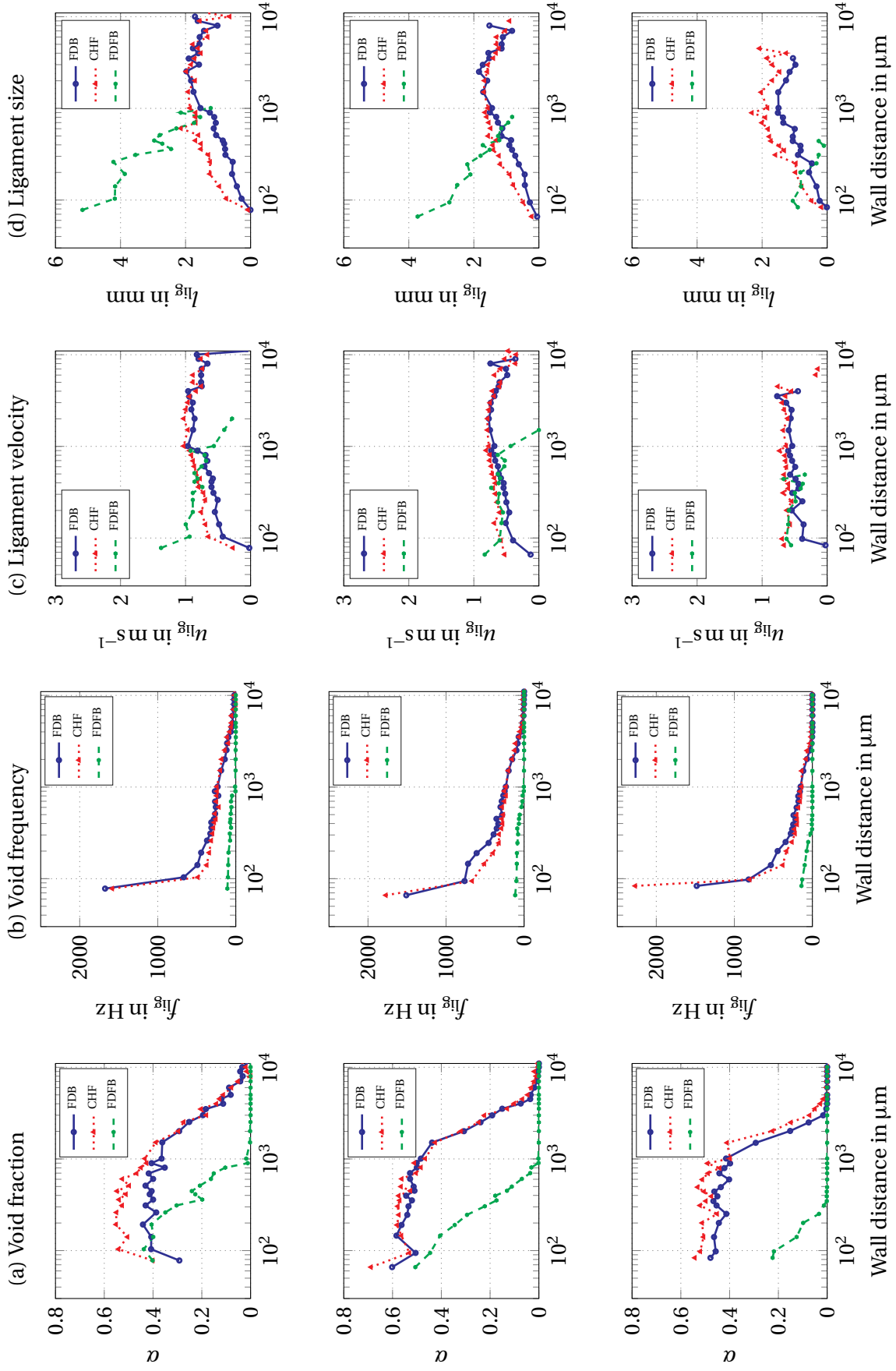
Figure C.2: Void profiles at the upper, middle and lower measurement position (top to bottom) for $G = 500\,\mathrm{kg\,m^{-2}\,s^{-1}}$ and $\Delta T_{\mathrm{sub}} = 24\,\mathrm{K}$.
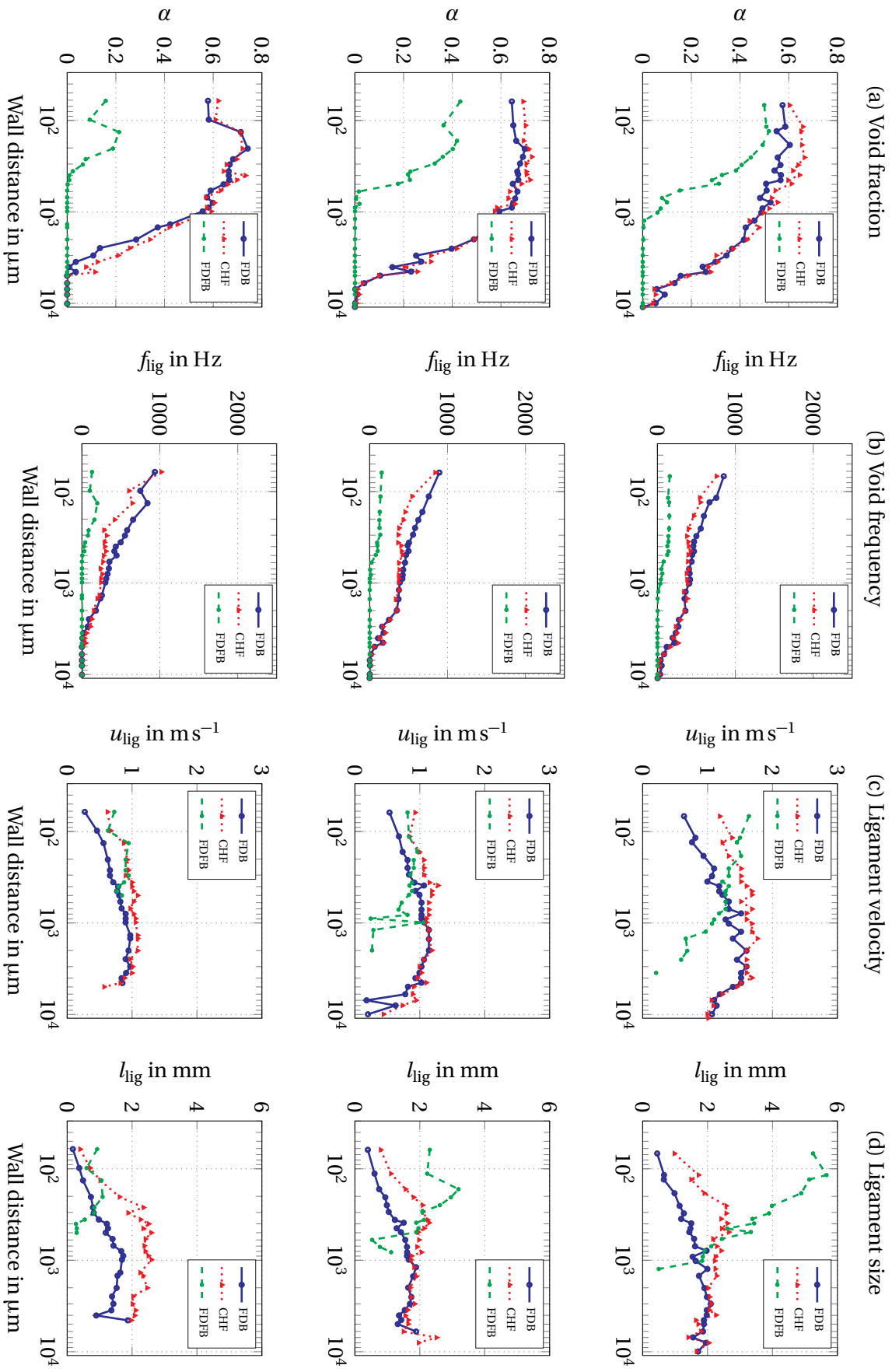
Figure C.3: Void profiles at the upper, middle and lower measurement position (top to bottom) for $G = 1000\,\mathrm{kg\,m^{-2}\,s^{-1}}$ and $\Delta T_{\mathrm{sub}} = 13\,\mathrm{K}$.
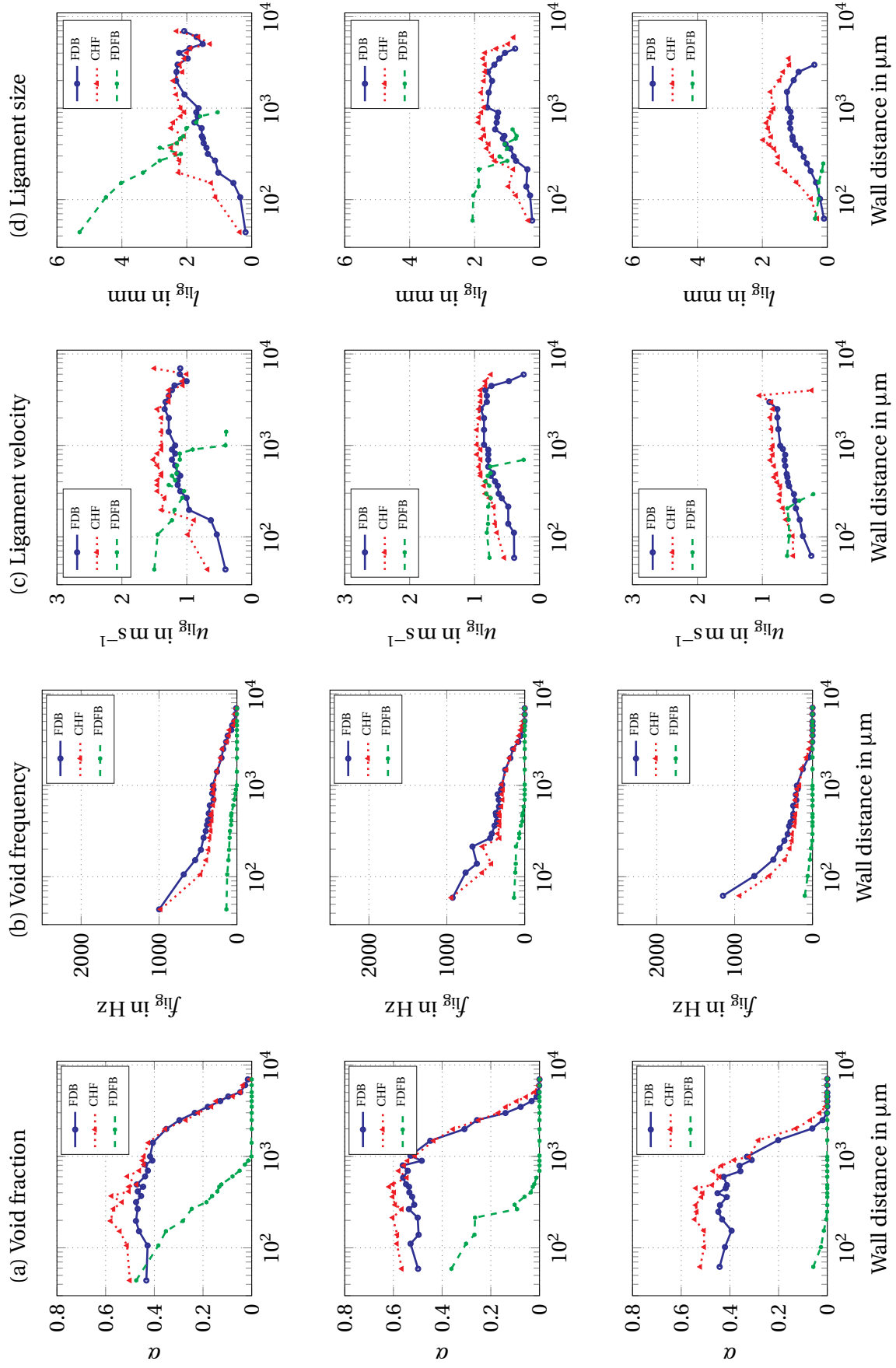
Figure C.4: Void profiles at the upper, middle and lower measurement position (top to bottom) for $G = 1000\,\mathrm{kg\,m^{-2}\,s^{-1}}$ and $\Delta T_{sub} = 24\,\mathrm{K}$.
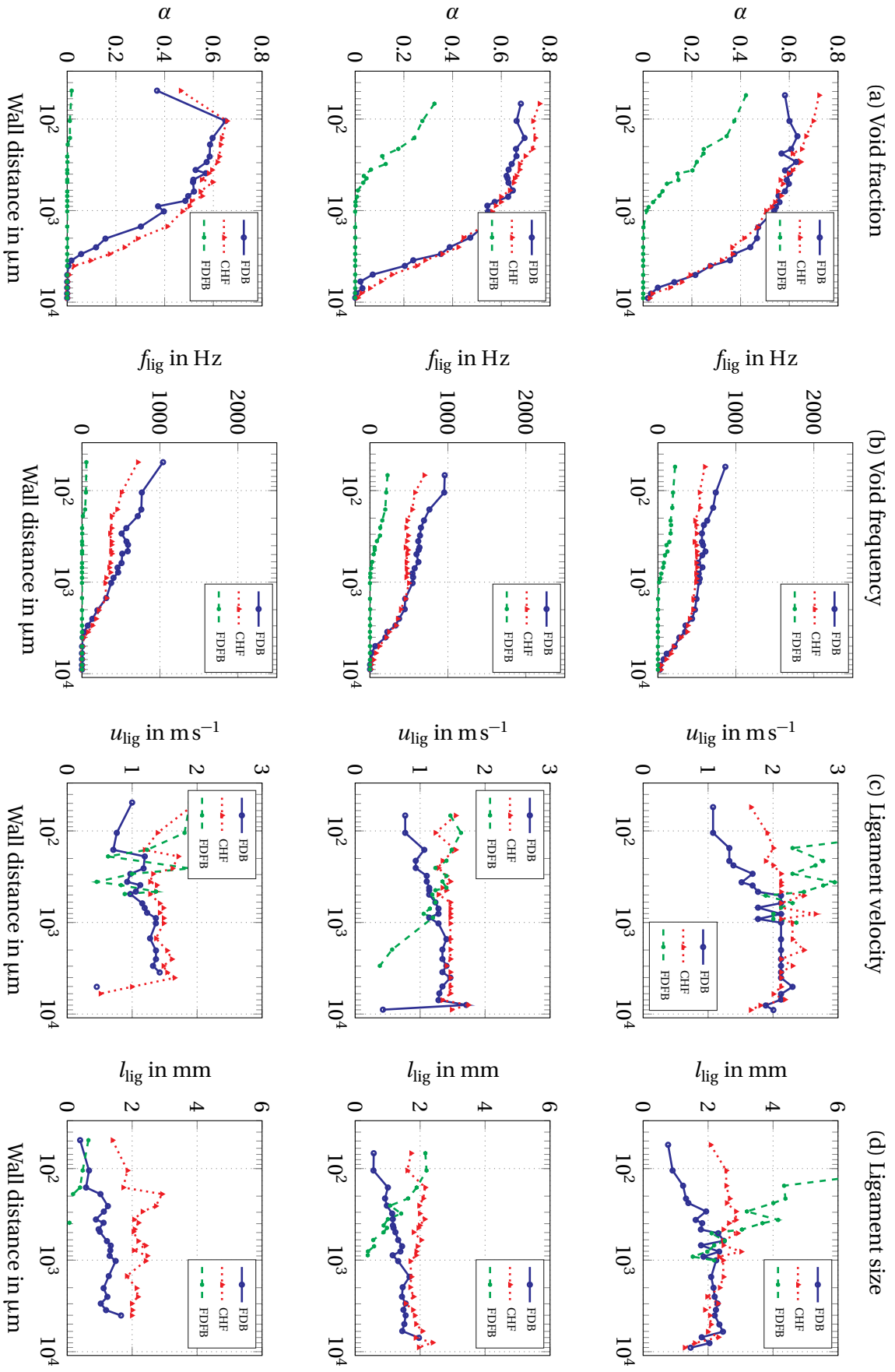
Figure C.5: Void profiles at the upper, middle and lower measurement position (top to bottom) for $G = 2000\,\mathrm{kg\,m^{-2}\,s^{-1}}$ and $\Delta T_{\mathrm{sub}} = 13\,\mathrm{K}$.
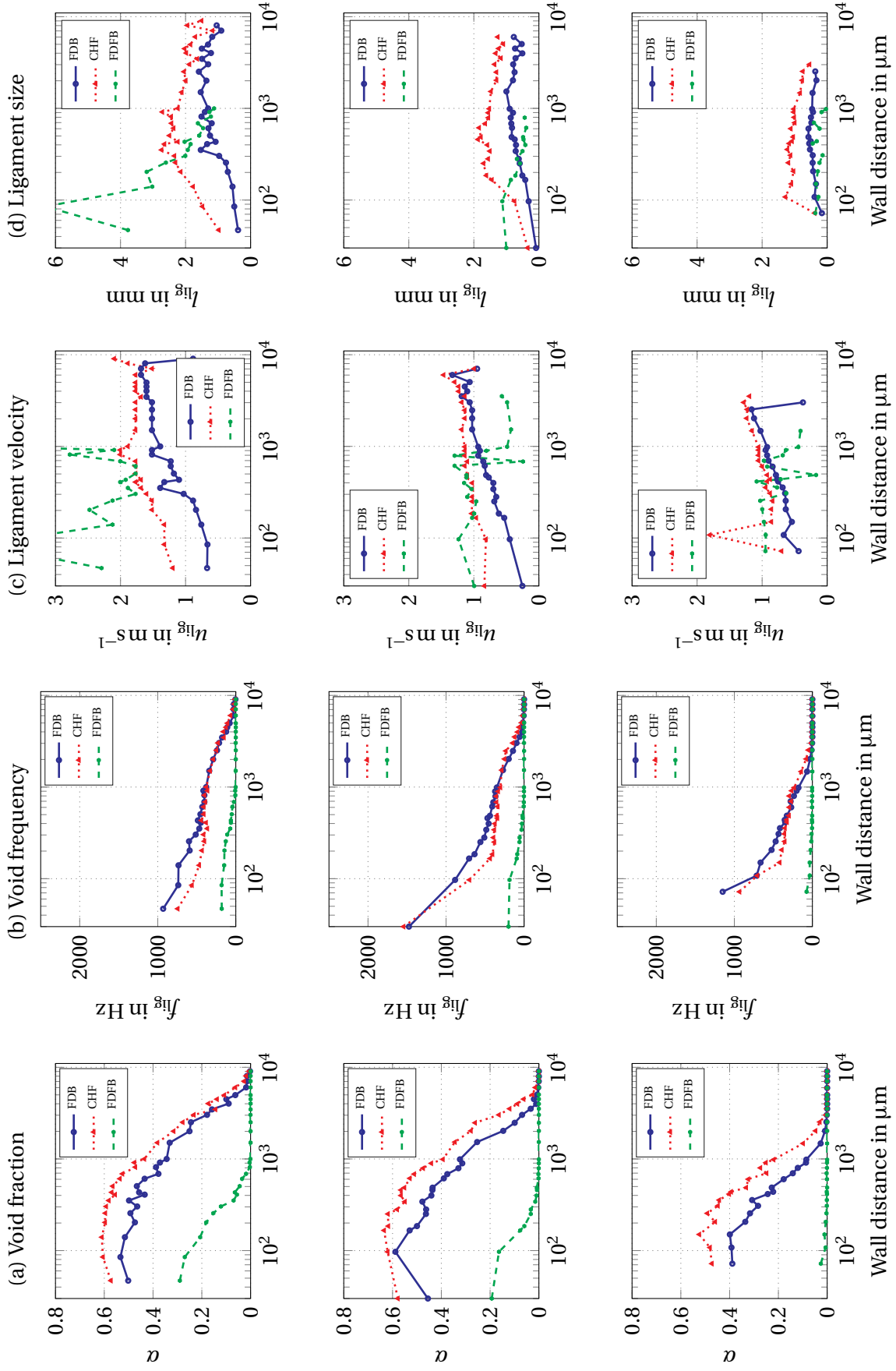
Figure C.6: Void profiles at the upper, middle and lower measurement position (top to bottom) for $G = 2000\,\mathrm{kg\,m^{-2}\,s^{-1}}$ and $\Delta T_{\mathrm{sub}} = 24\,\mathrm{K}$.

Supervised Theses

Associated with this dissertation are a number of student theses as well as works performed by student researchers that were supervised by the author of this work. The theses were prepared at the Thermodynamics Institute of the Technical University of Munich during the years 2015 to 2018 under the close supervision of the present author. Various issues were investigated concerning the development of measurement techniques, the numerical investigation of boiling models as well as the conduction and evaluation of boiling experiments. All theses were written in German. Some parts of these supervised theses may have been incorporated into the present dissertation. The author would like to express his sincere gratitude to all supervised students for their commitment supporting this research project.

| Student	Thesis
Thomas Greß	*Konstruktion, Simulation und Inbetriebnahme einer Messzelle zur experimentellen Untersuchung des unterkühlten Strömungssiedens*, Semesterarbeit, January 27, 2015
Waldemar Parschkoff	*Implementierung und Analyse von Siedemodellen zur Prognose der kritischen Wärmenstromdichte bei unterkühltem Strömungssieden in MATLAB*, Semesterarbeit, December 7, 2015
Patrick Brandl	*Verhalten der Dampfphase an einem vertikalen, wandbündigen Kupferheizer bei unterkühltem Strömungssieden*, Semesterarbeit, March 6, 2016
Korbinian Breitmoser	*Implementierung und Analyse zweier Bubble Crowding Modelle zur Prognose der kritischen Wärmestromdichte bei unterkühltem Strömungssieden in Matlab*, Semesterarbeit, April 15, 2016

Valentin Scharl	*Inbetriebnahme einer faseroptischen Messtechnik zur Geschwindigkeitsmessung von Phasengrenzflächen in unterkühltem Strömungssieden,* Bachelorarbeit, October 28, 2016
Ludwig Sembach	*Experimentelle Untersuchung der Gasphase bei unterkühltem Strömungssieden entlang der Siedelinie,* Masterarbeit, May 15, 2017
Julia Scheck	*Inverse Simulation der Wärmestromdichtenverteilung innerhalb eines Heizers bei der Durchführung von Siedeexperimenten,* Masterarbeit, June 20, 2017
Veronika Krumova	*Experimentelle Untersuchung des Blasenverhaltens bei unterkühltem Strömungssieden mittels faseroptischen Sonden,* Bachelorarbeit, August 10, 2017
Alexander Kürmeier	*Videometrische Untersuchung des Verhaltens der Dampfphase bei unterkühltem Strömungssieden im Bereich der kritischen Wärmestromdichte an einem beheizten Stab,* Bachelorarbeit, December 7, 2017
David Lampl	*Experimentelle Untersuchung der Gasphase im Bereich der kritischen Wärmestromdichte bei unterkühltem Strömungssieden mit optischen Mikrosonden,* Bachelorarbeit, December 7, 2017
Daniel Czech	*Entwurf und Konstruktion von Gehäuse und Transportverpackung für eine faseroptische Messtechnik mit Fokus auf Ergonomie, optischem Erscheinungsbild und Wirtschaftlichkeit,* Bachelorarbeit, December 20, 2017
Manuel Demmelmair	*Phänomenologie und Nachweis der Dampfblasenbildung mit komplementärer Messtechnik in motornahen Otto-Kraftstoffsystemkomponenten,* Masterarbeit, March 30, 2018

Philipp Nöcker

Experimentelle Untersuchung der Gasphase an einem Stabheizer bei unterkühltem Strömungssieden mit optischen Mikrosonden, Bachelorarbeit, August 27, 2018

Bibliography

[1] M. Bruder, G. Bloch, and T. Sattelmayer. "Critical Heat Flux in Flow Boiling - Review of the Current Understanding and Experimental Approaches". In: *Proceedings of the 9th International Conference on Boiling and Condensation Heat Transfer*. Boulder, Colorado, April 26-30, 2015.

[2] M. Bruder, G. Bloch, and T. Sattelmayer. "Critical Heat Flux in Flow Boiling - Review of the Current Understanding and Experimental Approaches". In: *Heat Transfer Engineering* 38.3 (2017), pp. 347–360.

[3] M. Bruder and T. Sattelmayer. "An Empirical Correlation for the Void Fraction at Critical Heat Flux Close to the Wall for Subcooled Flow Boiling of a Low Boiling Refrigerant". In: *Heat and Mass Transfer Research Journal* 2.2 (2018), pp. 1–15.

[4] M. Bruder, L. Sembach, V. Krumova, and T. Sattelmayer. "Local Data of Heat Flux, Wall Temperature and the Void Phase Along the Boiling Curve During Vertical Subcooled Flow Boiling of Refrigerant Novec 649 at a Copper Wall". In: *Data in Brief* 21 (2018), pp. 1415 –1429.

[5] M. Bruder, P. Riffat, and T. Sattelmayer. "Identification of Universal Heat Transfer Characteristics Along the Boiling Curve for Vertical Subcooled Flow Boiling of Refrigerant Novec 649". In: *Heat and Mass Transfer* (in press), pp. 1–15.

[6] P. Riffat, M. Bruder, C. Hirsch, and T. Sattelmayer. "Calibration of the Parameters of the RPI Boiling Model for Novec^{TM}649 Refrigerant". In: *Proceedings of the 8th International Conference and Workshop Remoo*. Venice, Italy, 29-31 May, 2018.

[7] C. Lifante, A. Ben Hadj Ali, H. Eickenbusch, M. Bruder, and F. Kaiser. "Prediction of Convective Boiling up to Critical Heat Flux (CHF) Conditions for Test Facilities with Vertical Heaters". In: *Proceedings of ICONE-27 - 27th International Conference on Nuclear Engineering*. Ibaraki, Japan, May 19-24, 2019.

[8] G. Bloch, J. Loth, M. Bruder, and T. Sattelmayer. "Effects of Turbulence and Longitudinal Vortices on Vapor Distribution and Heat Fluxes in Subcooled Flow Boiling". In: *Proceedings of ECI 8thInternational Conference on Boiling and Condensation Heat Transfer*. Lausanne, Switzerland, 2012.

[9] G. Bloch, M. Bruder, and T. Sattelmayer. "A Critical Review on the Mechanisms Triggering the DNB in Subcooled Flow Boiling Using a Complementary Experimental Approach". In: *Proceedings of the 9th International Conference on Boiling and Condensation Heat Transfer*. Boulder, Colorado, April 26-30, 2015.

[10] G. Bloch, M. Bruder, and T. Sattelmayer. "A Study on the Mechanisms Triggering the Departure from Nucleate Boiling in Subcooled Vertical Flow Boiling Using a Complementary Experimental Approach". In: *International Journal of Heat and Mass Transfer* 92 (2016), pp. 403 –413.

[11] C. R. Kharangate and I. Mudawar. "Review of Computational Studies on Boiling and Condensation". In: *International Journal of Heat and Mass Transfer* 108 (2017), pp. 1164 –1196.

[12] G. Celata and A. Mariani. "CHF and Post-CHF (Post-Dryout) Heat Transfer, Chapter 17". In: *Handbook of Phase Change: Boiling and Condensation, edited by Kandlikar, S.G. and Shoji, M. and Dhir, V.K.* (1999), pp. 443–493.

[13] J. Weisman and B. Pei. "Prediction of Critical Heat Flux in Flow Boiling at Low Qualities". In: *International Journal of Heat and Mass Transfer* 26.10 (1983), pp. 1463 –1477.

[14] C. H. Lee and I. Mudawar. "A Mechanistic Critical Heat Flux Model for Subcooled Flow Boiling Based on Local Bulk Flow Conditions". In: *International Journal of Multiphase Flow* 14.6 (1988), pp. 711–728.

[15] J. Galloway and I. Mudawar. "CHF Mechanism in Flow Boiling From a Short Heated Wall - II. Theoretical CHF Model". In: *International Journal of Heat and Mass Transfer* 36.10 (1993), pp. 2527–2540.

[16] G. Bloch. "An Experimental Study on Vertical Subcooled Flow Boiling Under the Influence of Turbulence and Secondary Flows". PhD thesis. Technische Universität München, 2016.

[17] G. Bloch and T. Sattelmayer. "Validation of Mechanistic CHF Models Using Optical Measuring Techniques". In: *Kerntechnik* 78.1 (2013), pp. 57–59.

[18] E. Baglietto, E. Demarly, R. Kommajosyula, N. Lubchenko, B. Magolan, and R. Sugrue. "A Second Generation Multiphase-CFD Framework Toward Predictive Modeling of DNB". In: *Nuclear Technology* 205.1-2 (2018), pp. 1–21.

[19] W. Ding, E. Krepper, and U. Hampel. "Quantitative Prediction of Critical Heat Flux Initiation in Pool and Flow Boiling". In: *International Journal of Thermal Sciences* 125 (2018), pp. 121 –131.

[20] J. Garnier, E. Manon, and G. Cubizolles. "Local Measurement on Flow Boiling of Refrigerant 12 in a Vertical Tube". In: *Multiphase Science and Technology* 13.1-2 (2001), pp. 1–111.

[21] G. Bartolomej, V. Brantov, Y. Molochnikov, Y. Kharitonov, V. Solodkii, G. Batashova, and V. Mikhailov. "An Experimental Investigation of True Volumetric Vapour Content with Subcooled Boiling in Tubes". In: *Thermal Engineering* 29.3 (1982), pp. 132–135.

[22] M. Etienne. "Contribution à l'Analyse et à la Modélistation Locale des Écoulements Bouillants Sous-Saturés dans les Conditions des Réacteurs à eau sou Pression". PhD thesis. Ecole Centrale Paris, Nov. 6, 2000.

[23] T. Lüttich, W. Marquardt, M. Buchholz, and H. Auracher. "Towards a Unifying Heat Transfer Correlation for the Entire Boiling Curve". In: *International Journal of Thermal Sciences* 43 (2004), pp. 1125–1139.

[24] M. Buchholz, H. Auracher, T. Lüttich, and W. Marquardt. "A Study of Local Heat Transfer Mechanisms Along the Entire Boiling Curve by Means of Microsensors". In: *International Journal of Thermal Sciences* 45 (2006), pp. 269–283.

[25] J. J. Jung, S. J. Kim, and J. J. Kim. "Observations of the Critical Heat Flux Process During Pool Boiling of FC-72". In: *Journal of Heat Transfer* 136.4 (2014), pp. 041501–041501–12.

[26] T. G. Theofanous, J. P. Tu, A. T. Dinh, and T. N. Dinh. "The Boiling Crisis Phenomenon: Part I: Nucleation and Nucleate Boiling Heat Transfer". In: *Experimental Thermal and Fluid Science* 26.67 (2002), pp. 775 –792.

[27] T. G. Theofanous, T. N. Dinh, J. P. Tu, and A. T. Dinh. "The Boiling Crisis Phenomenon: Part II: Dryout Dynamics and Burnout". In: *Experimental Thermal and Fluid Science* 26.67 (2002), pp. 793 –810.

[28] S. Gong, W. Ma, and H. Gu. "An Experimental Investigation on Bubble Dynamics and Boiling Crisis in Liquid Films". In: *International Journal of Heat and Mass Transfer* 79 (2014), pp. 694 –703.

[29] D. E. Kim, J. Song, and H. Kim. "Simultaneous Observation of Dynamics and Thermal Evolution of Irreversible Dry Spot at Critical Heat Flux in Pool Boiling". In: *International Journal of Heat and Mass Transfer* 99 (2016), pp. 409–424.

[30] H. Auracher and W. Marquardt. "Heat Transfer Characteristics and Mechanisms Along Entire Boiling Curves under Steady-State and Transient Conditions". In: *International Journal of Heat and Fluid Flow* 25.2 (2004). Selected Papers from the 5th ECI International Conference on Boiling Heat Transfer, pp. 223 –242.

[31] S. Mancin, A. Diani, and L. Rossetto. "Flow Boiling Heat Transfer, Dewetting-Rewetting, and Dryout Visualization of HFOs in an Asymmetrically Heated Rectangular Plain Channel". In: *Applied Thermal Engineering* 107.C (2016), pp. 960 –974.

[32] J.-M. Le Corre, S.-C. Yao, and C. H. Amon. "Two-Phase Flow Regimes and Mechanisms of Critical Heat Flux under Subcooled Flow Boiling Conditions". In: *Nuclear Engineering and Design* 240.2 (2010). Twelfth International Topical Meeting on Nuclear Reactor Thermal Hydraulics (NURETH-12), pp. 245 –251.

[33] J.-M. Le Corre, S.-C. Yao, and C. H. Amon. "A Mechanistic Model of Critical Heat Flux Under Subcooled Flow Boiling Conditions for Application to One- and Three-Dimensional Computer Codes". In: *Nuclear Engineering and Design* 240.2 (2010), pp. 235–244.

[34] H. Auracher and M. Buchholz. "Experiments on the Fundamental Mechanisms of Boiling Heat Transfer". In: *Journal of the Brazilian Society of Mechanical Science and Engineering* 27.1 (2005), pp. 1–22.

[35] S. Nukiyama. "The Maximum and Minimum Values of The Heat Q Transmitted From Metal to Boiling Water Under Atmospheric Pressure". In: *Journal of the Japanese Society of Mechanical Engineers* 37 (1934), pp. 367–374.

[36] F. P. Incropera, D. P. Dewitt, T. L. Berman, and A. S. Lavine. *Fundamentals of Heat and Mass Transfer*. Ed. by J. Hayton. 6th ed. Hoboken: John Wiley & Sons, 2007.

[37] H. Auracher. "Some Remarks on the Nukiyama Curve". In: *JSME Thermal Engineering Division Newsletter* 42 (2003), pp. 1–4.

[38] L. S. Tong and Y. S. Tang. *Boiling Heat Transfer and Two-Phase Flow*. Ed. by L. Lackenbach and H. Seltzer. Taylor and Francis, Washington, D.C, 1997.

[39] G. P. Celata, M. Cumo, and A. Mariani. "Enhancement of CHF Water Subcooled Flow Boiling in Tubes Using Helically Coiled Wires". In: *International Journal of Heat and Mass Transfer* 37.1 (1994), pp. 53–67.

[40] G. Celata, M. Cumo, and A. Mariani. "Burnout in Highly Subcooled Water Flow Boiling in Small Diameter Tubes". In: *International Journal of Heat and Mass Transfer* 36.5 (1993), pp. 1269 –1285.

[41] L. Cheng and G. Xia. "Experimental Study of CHF in a Vertical Spirally Internally Ribbed Tube under the Condition of High Pressures". In: *International Journal of Thermal Sciences* 41.4 (2002), pp. 396 –400.

[42] S. G. Kandlikar. "Critical Heat Flux in Subcooled Flow Boiling - An Assessment of Current Understanding and Future Directions for Research". In: *Multiphase Science and Technology* 13.3-4 (2001), pp. 207–232.

[43] R. Boyd. "Subcooled Water Flow Boiling Experiments Under Uniform High Heat Flux Conditions". In: *Fusion Science and Technology* 13.1 (1988), pp. 131–142.

[44] R. Boyd. "Subcooled Water Flow Boiling at 1.66 MPa Under Uniform High Heat Flux Conditions". In: *Fusion Science and Technology* 16.3 (1989), pp. 324–330.

[45] R. Boyd. "Subcooled Water Flow Boiling Transition and the L/D Effect on CHF for a Horizontal Uniformly Heated Tube". In: *Fusion Science and Technology* 18.2 (1990), pp. 317–324.

[46] G. Bloch, D. Schmitt, and T. Sattelmayer. "Influence of Turbulence Induced by Perforated Plates on Heat Transfer and Critical Heat Flux in Subcooled Flow Boiling". In: *Proceedings of ITP-2011*. Dresden, Germany, 2011.

[47] G. Bloch, C. Jochum, T. Schechtl, and T. Sattelmayer. "Subcooled Flow Boiling in a Rectangular Channel With Added Turbulence and Longitudinal Vortices". In: *Proceedings of the 2012 20th International Conference on Nuclear Engineering collocated with the ASME 2012 Power Conference*. Anaheim, USA, 2012.

[48] G. Bloch and T. Sattelmayer. "Effects of Turbulence and Secondary Flows on Subcooled Flow Boiling". In: *Heat and Mass Transfer* 50.3 (2014), pp. 427–435.

[49] Y. Katto. "A Physical Approach to Critical Heat Flux of Subcooled Flow Boiling in Round Tubes". In: *International Journal of Heat and Mass Transfer* 33 (1990), pp. 611–620.

[50] A. E. Bergles. "Subcooled Burnout in Tubes of Small Diameter". In: *American Society of Mechanical Engineers Paper 63-WA-182* (1963).

[51] G. Liang and I. Mudawar. "Review of Pool Boiling Enhancement by Surface Modification". In: *International Journal of Heat and Mass Transfer* 128 (2019), pp. 892 –933.

[52] G. Liang and I. Mudawar. "Pool Boiling Citical Heat Flux (CHF) Part 1: Review of Mechanisms, Models, and Correlations". In: *International Journal of Heat and Mass Transfer* 117 (2018), pp. 1352 –1367.

[53] C. K. Yu and D. C. Lu. "Pool Boiling Heat Transfer on Horizontal Rectangular Fin Array in Saturated FC-72". In: *International Journal of Heat and Mass Transfer* 50.17-18 (2007), pp. 3624–3637.

[54] S. J. Reed and I. Mudawar. "Enhancement of Boiling Heat Transfer Using Highly Wetting Liquids with Pressed-on Fins at Low Contact Forces". In: *International Journal of Heat and Mass Transfer* 40.10 (1997), pp. 2379 –2392.

[55] S. G. Kandlikar. "Controlling Bubble Motion over Heated Surface through Evaporation Momentum Force to Enhance Pool Boiling Heat Transfer". In: *Applied Physics Letters* 102.5 (2013), p. 051611.

[56] S. G. Kandlikar and P. Spiesman. "Effect of Surface Finish on Flow Boiling Heat Transfer". In: *Paper presented at the ASME IMECE98 Meeting*. Anaheim, CA, Nov. 15-20, 1998.

[57] B. J. Zhang, J. Park, and K. J. Kim. "Augmented Boiling Heat Transfer on the Wetting-Modified Three Dimensionally-Interconnected Alumina Nano Porous Surfaces in Aqueous Polymeric Surfactants". In: *International Journal of Heat and Mass Transfer* 63 (2013), pp. 224 –232.

[58] G. P. Celata, M. Cumo, and A. Mariani. "Geometrical Effects on the Subcooled Flow Boiling Critical Heat Flux ". In: *Revue Générale de Thermique* 36.11 (1997), pp. 807 – 814.

[59] M. P. Fiori and A. E. Bergles. *Model of Critical Heat Flux in Subcooled Flow Boiling*. Tech. rep. Massachusetts Institute of Technology, Department of Mechanical Engineering, Engineering Projects Laboratory, 1968.

[60] Y. Katto. "Critical Heat Flux". In: *International Journal of Multiphase Flow* 20 (1994), pp. 53–90.

[61] C. Konishi, I. Mudawar, and M. M. Hasan. "Investigation of Localized Dryout Versus CHF in Saturated Flow Boiling". In: *International Journal of Heat and Mass Transfer* 67 (2013), pp. 131–146.

[62] R. D. Boyd. "Review of Subcooled Flow Boiling Critical Heat Flux (CHF) and its Application to Fusion Energy System Components Part II: Microconvective, Experimental and Correlational Aspects". In: *Fusion Technology* 7 (1983), pp. 31–51.

[63] G. Celata, M. Cumo, and A. Mariani. "Assessment of Correlations and Models for the Prediction of CHF in Water Subcooled Flow Boiling". In: *International Journal of Heat and Mass Transfer* 37.2 (1994), pp. 237 –255.

[64] L. S. Tong. "Boundary-Layer Analysis of the Flow Boiling Crisis". In: *International Journal of Heat and Mass Transfer* 11.7 (1968), pp. 1208–1211.

[65] F. C. Gunther. "Photographic Study of Surface-Boiling Heat Transfer to Water With Forced Convection". In: *Transaction of the ASME* 73.2 (1951), pp. 115–123.

[66] D. Lee. *Two-Phase Flow and Heat Transfer*. Ed. by D. Butterworth and G. Hewitt. Oxford University Press, 1977, pp. 295–322.

[67] J. G. Collier and J. R. Thome. *Convective Boiling and Condensation*. Oxford University Press, 1994.

[68] P. Whalley. *Boiling, Condensation, and Gas-Liquid Flow*. Oxford University Press, 1987, pp. 163–166.

[69] R. W. Bowring and United Kingdom Atomic Energy Authority. *A Simple But Accurate Round Tube Uniform Heat Flux, Dryout Correlation Over the Pressure Range 0.7 - 17 MN*. U.K.A.E.A., 1972.

[70] Y. Katto and H. Ohno. "An Improved Version of the Generalized Correlation of Critical Heat Flux for the Forced Convective Boiling in Uniformly Heated Vertical Tubes". In: *International Journal of Heat and Mass Transfer* 27.9 (1984), pp. 1641 –1648.

[71] S. Bertoletti, G. P. Gaspari, C. Lobardi, G. Peterlongo, and F. A. Tacconi. "A Generalized Correlation for Predicting the Heat Transfer Crisis with Steam-Water Mixtures". In: *Energia Nucleare* 11.10 (1964), pp. 571–572.

[72] M. P. Fiori and A. E. Bergles. "Model of Critical Heat Flux in Subcooled Flow Boiling". In: *Heat Transfer 1970, Papers Presented at the Fourth International Heat Transfer Conference*. Paris, Versailles, 1970.

[73] R. Hino and T. Ueda. "Studies on Heat Transfer and Flow Characteristics in Subcooled Flow Boiling - Part 2. Flow Characteristics". In: *International Journal of Multiphase Flow* 11.3 (1985), pp. 283–297.

[74] G. P. Celata, M. Cumo, A. Mariani, M. Simoncini, and G. Zummo. "Rationalization of Existing Mechanistic Models for the Prediction of Water Subcooled Flow Boiling Critical Heat Flux". In: *International Journal of Heat and Mass Transfer* 37.1 (1994), pp. 347–360.

[75] D. B. Kirby and J. W. Westwater. "Bubble and Vapor Behavior on a Heated Horizontal Plate During Pool Boiling Near Burnout". In: *Chemical Engineering Progress Symposium Series*. Vol. 61. 1965, pp. 238–248.

[76] R. J. Mattson. "A Photographic Study of Subcooled Flow Boiling and the Boiling Crisis in Freon-113". PhD thesis. The University of Michigan, College for Engineering, Department of Mechanical Engineering, Cavitation and Multiphase Flow Laboratory, 1972.

[77] G. Bloch, W. Muselmann, M. Saier, and T. Sattelmayer. "A Phenomenological Study on Effects Leading to the Departure From Nucleate Boiling in Subcooled Flow Boiling". In: *International Journal of Heat and Mass Transfer* 67 (2013), pp. 61–69.

[78] W. Hebel, W. Detavernier, and M. Decreton. "A Contribution to the Hydrodynamics of Boiling Crisis in a Forced Flow of Water". In: *Nuclear Engineering and Design* 64 (1981), pp. 433–445.

[79] J. Weisman and S. Ying. "A Theoretically Based Critical Heat Flux Prediction for Rod Bundles at PWR Conditions". In: *Nuclear Engineering and Design* 85.2 (1985), pp. 239 –250.

[80] S. H. Ying and J. Weisman. "Prediction of Critical Heat Flux in Flow Boiling at Intermediate Qualities". In: *International Journal of Heat and Mass Transfer* 29.11 (1986), pp. 1639–1648.

[81] J. Weisman and S. Illeslamlou. "Phenomenological Model for Prediction of Critical Heat Flux Under Highly Subcooled Conditions". In: *Fusion Technology* 13.4 (1988), pp. 654–659.

[82] J. C. Lim and J. Weisman. "A Phenomenologically Based Prediction of the Critical Heat Flux in Channels Containing an Unheated Wall". In: *International Journal of Heat and Mass Transfer* 33.1 (1990), pp. 203–205.

[83] J. Weisman, J. Y. Yang, and S. Usman. "A Phenomenological Model for Boiling Heat Transfer and the Critical Heat Flux in Tubes Containing Twisted Tapes". In: *International Journal of Heat and Mass Transfer* 37.1 (1994), pp. 69–80.

[84] J. Y. Yang and J. Weisman. "A Phenomenological Model of Subcooled Flow Boiling in the Detached Bubble Region". In: *International Journal of Multiphase Flow* 17.1 (1991), pp. 77 –94.

[85] S. H. Chang and K. W. Lee. "A Critical Heat Flux Model Based on Mass, Energy, and Momentum Balance for Upflow Boiling at Low Qualities". In: *Nuclear Engineering and Design* 113.1 (1989), pp. 35 –50.

[86] Y. M. Kwon and S. H. Chang. "A Mechanistic Critical Heat Flux Model for Wide Range of Subcooled and Low Quality Flow Boiling". In: *Nuclear Engineering and Design* 188.1 (1999), pp. 27 –47.

[87] S. Levy. "Forced Convection Subcooled Boiling - Prediction of Vapor Volumetric Fraction". In: *International Journal of Heat and Mass Transfer* 10.7 (1967), pp. 951–965.

[88] R. T. Lahey and F. F. J. Moody. *The Thermal Hydraulics of a Boiling Water Nuclear Reactor*. Monograph Series on Nuclear Science and Technology. American Nuclear Society, 1977.

[89] Y. Haramura and Y. Katto. "A New Hydrodynamic Model of Critical Heat Flux, Applicable Widely to Both Pool and Forced Convection Boiling on Submerged Bodies in Saturated Liquids". In: *International Journal of Heat and Mass Transfer* 26 (1983), pp. 389–399.

[90] Y. Katto. "Prediction of Critical Heat Flux of Subcooled Flow Boiling in Round Tubes". In: *International Journal of Heat and Mass Transfer* 33.9 (1990), pp. 1921–1928.

[91] G. P. Celata, M. Cumo, A. Mariani, and G. Zummo. "The Prediction of the Critical Heat Flux in Water-Subcooled Flow Boiling". In: *International Journal of Heat and Mass Transfer* 38 (1995), pp. 1111–1119.

[92] L. Payan-Rodriguez, A. Gallegos-Munoz, G. Porras-Loaiza, and M. Picon-Nunez. "Critical Heat Flux Prediction for Water Boiling in Vertical Tubes of a Steam Generator". In: *International Journal of Thermal Sciences* 44.2 (2005), pp. 179 –188.

[93] M. Ishii and N. Zuber. "Drag Coefficient and Relative Velocity in Bubbly, Droplet or Particulate Flows". In: *AIChE Journal* 25.5 (1979), pp. 843–855.

[94] F. W. Staub. "The Void Fraction in Subcooled Boiling - Prediction of the Initial Point of Net Vapor Generation". In: *Journal of Heat Transfer* 90.1 (1968), pp. 151–157.

[95] R. Martinelli. "Heat Transfer to Molten Metals". In: *Transactions of ASME* 69 (1947), pp. 947–951.

[96] J. Galloway and I. Mudawar. "CHF Mechanism in Flow Boiling From a Short Heated Wall - I. Examination of Near-Wall Conditions With the Aid of Photomicrography and High-Speed Video Imaging". In: *International Journal of Heat and Mass Transfer* 36.10 (1993), pp. 2511–2526.

[97] C. O. Gersey and I. Mudawar. "Effects of Heater Length and Orientation on the Trigger Mechanism for Near-Saturated Flow Boiling Critical Heat Flux - II. Critical Heat Flux Model". In: *International Journal of Heat and Mass Transfer* 38.4 (1995), pp. 643–654.

[98] H. Zhang, I. Mudawar, and M. M. Hasan. "CHF Model for Subcooled Flow Boiling in Earth Gravity and Microgravity". In: *International Journal of Heat and Mass Transfer* 50 (2007), pp. 4039–4051.

[99] C. Konishi, H. Lee, I. Mudawar, M. M. Hasan, H. K. Nahra, N. R. Hall, J. D. Wagner, R. L. May, and J. R. Mackey. "Flow Boiling in Microgravity: Part 2 - Critical Heat Flux Interfacial Behavior, Experimental Data, and Model". In: *International Journal of Heat and Mass Transfer* 81 (2015), pp. 721–736.

[100] C. R. Kharangate, I. Mudawar, and M. M. Hasan. "Experimental and Theoretical Study of Critical Heat Flux in Vertical Upflow with Inlet Vapor Void". In: *International Journal of Heat and Mass Transfer* 55.1-3 (2012), pp. 360–374.

[101] J. C. Sturgis and I. Mudawar. "Critical Heat Flux in a Long, Rectangular Channel Subjected to One-Sided Heating - I. Flow Visualization". In: *International Journal of Heat and Mass Transfer* 42 (1999), pp. 1835–1847.

[102] S. Jung and H. Kim. "Observation of the Mechanism Triggering Critical Heat Flux in Pool Boiling of Saturated Water under Atmospheric Pressure". In: *International Journal of Heat and Mass Transfer* 128 (2019), pp. 229 –238.

[103] V. K. Dhir. "Boiling Heat Transfer". In: *Annual Review of Fluid Mechanics* 30.1 (1998), pp. 365–401.

[104] V. Janecek and V. S. Nikolayev. "Triggering the Boiling Crisis: A Study of the Dry Spot Spreading Mechanism". In: *Interfacial Phenomena and Heat Transfer* 2.4 (2014), pp. 363–383.

[105] M. G. Cooper and A. J. P. Lloyd. "The Microlayer in Nucleate Pool Boiling". In: *International Journal of Heat and Mass Transfer* 12.8 (1969), pp. 895 –913.

[106] Y. Zhao and T. Tsuruta. "Prediction of Bubble Behavior in Subcooled Pool Boiling Based on Microlayer Model". In: *JSME International Journal Series B* 45.2 (2002), pp. 346–354.

[107] Y.-H. Zhao, T. Masuoka, and T. Tsuruta. "Unified Theoretical Prediction of Fully Developed Nucleate Boiling and Critical Heat Flux Based on a Dynamic Microlayer Model". In: *International Journal of Heat and Mass Transfer* 45.15 (2002), pp. 3189 –3197.

[108] Y.-H. Zhao, T. Masuoka, and T. Tsuruta. "Theoretical Studies on Transient Pool Boiling Based on Microlayer Model". In: *International Journal of Heat and Mass Transfer* 45.21 (2002), pp. 4325 –4331.

[109] C. Kunkelmann, K. Ibrahem, N. Schweizer, S. Herbert, P. Stephan, and T. Gambaryan-Roisman. "The Effect of Three-Phase Contact Line Speed on Local Evaporative Heat Transfer: Experimental and Numerical Investigations". In: *International Journal of Heat and Mass Transfer* 55.7 (2012), pp. 1896 –1904.

[110] S. Nishio, T. Gotoh, and N. Nagai. "Observation of Boiling Structures in High Heat-Flux Boiling". In: *International Journal of Heat and Mass Transfer* 41.21 (1998), pp. 3191 –3201.

[111]   I.-C. Chu, H. C. No, and C.-H. Song. "Visualization of Boiling Structure and Critical Heat Flux Phenomenon for a Narrow Heating Surface in a Horizontal Pool of Saturated Water". In: *International Journal of Heat and Mass Transfer* 62 (2013), pp. 142 –152.

[112]   I.-C. Chu, H. C. No, C.-H. Song, and D. J. Euh. "Observation of Critical Heat Flux Mechanism in Horizontal Pool Boiling of Saturated Water". In: *Nuclear Engineering and Design* 279 (2014). SI : CFD4NRS-4, pp. 189–199.

[113]   H. Kim, Y. Park, and J. Buongiorno. "Measurement of Wetted Area Fraction in Subcooled Pool Boiling of Water Using Infrared Thermography". In: *Nuclear Engineering and Design* 264 (2013). Special Issue: NURETH-14, pp. 103 –110.

[114]   S. J. Ha and H. C. No. "A Dry-Spot Model of Critical Heat Flux Applicable to Both Pool Boiling and Subcooled Forced Convection Boiling". In: *International Journal of Heat and Mass Transfer* 43.2 (2000), pp. 241–250.

[115]   S. J. Ha and H. C. No. "A Dry-Spot Model of Critical Heat Flux Applicable to Both Pool Boiling and Subcooled Forced Convection Boiling". In: *International Journal of Heat and Mass Transfer* 41.2 (1998), pp. 303–311.

[116]   H. J. Chung and H. C. No. "Simultaneous Visualization of Dry Spots and Bubbles for Pool Boiling of R-113 on a Horizontal Heater". In: *International Journal of Heat and Mass Transfer* 46.12 (2003), pp. 2239 –2251.

[117]   J. Y. Choi, H. C. No, and J. Kim. "Development of a Dry Patch Model for Critical Heat Flux Prediction". In: *International Journal of Heat and Mass Transfer* 100 (2016), pp. 386 –395.

[118]   N. V. Vasiliev, Y. A. Zeigarnik, and K. A. Khodakov. "Evolution of Steam-Water Flow Structure under Subcooled Water Boiling at Smooth and Structured Heating Surfaces". In: *Journal of Physics: Conference Series* 891.1 (2017), pp. 1–7.

[119]   M. Buchholz, T. Lüttich, H. Auracher, and W. Marquardt. "Experimental Investigation of Local Processes in Pool Boiling Along the Entire Boiling Curve". In: *International Journal of Heat and Fluid Flow* 25 (2004), pp. 243–261.

[120]   E. Baglietto, E. Demarly, and R. Kommajosyula. "Predicting Critical Heat Flux With Multiphase CFD: 4 Years in the Making". In: *Fluids Engineering Division Summer Meeting*. Vol. 1C. Waikoloa, Hawaii, USA, July 30 - August 3, 2017.

[121]   N. Kurul and M. Z. Podowski. "Multidimensional Effects in Forced Convection Subcooled Boiling". In: *Proceedings of the Ninth International Heat Transfer Conference*. Vol. 2. 1990, pp. 19–24.

[122]   E. Baglietto and M. A. Christon. *Demonstration & Assessment of Advanced Modeling Capabilities for Multiphase Flow with Sub-cooled Boiling*. Tech. rep. CASL-U-2013-0181- 001. Massachusetts Institute of Technology, 2013.

[123]   T. J. Drzewiecki, I. M. Asher, T. P. Grunloh, V. E. Petrov, K. J. Fidkowski, A. Manera, and T. J. Downar. "Parameter Sensitivity Study of Boiling and Two-Phase Flow Models in CFD". In: *The Journal of Computational Multiphase Flows* 4.4 (2012), pp. 411–425.

[124]   T. Hibiki and M. Ishii. "Active Nucleation Site Density in Boiling Systems". In: *International Journal of Heat and Mass Transfer* 46.14 (2003), pp. 2587–2601.

[125] L. Gilman and E. Baglietto. "A Self-Consistent, Physics-Based Boiling Heat Transfer Modeling Framework for Use in Computational Fluid Dynamics". In: *International Journal of Multiphase Flow* 95.C (2017), pp. 35 –53.

[126] G. F. Hewitt. *Measurement of Two Phase Flow Parameters*. Academic Press, 1978.

[127] C. Boyer, A.-M. Duquenne, and G. Wild. "Measuring Techniques in Gas- Liquid and Gas- Liquid- Solid- Reactors". In: *Chemical Engineering Science* 57 (2002), pp. 3185–3215.

[128] M. Lehner, D. Mewes, U. Dinglreiter, and R. Tauscher. *Applied Optical Measurements.* Ed. by M. Lehner and D. Mewes. Berlin: Springer, 1999.

[129] F. Mayinger and O. Feldmann. *Optical Measurements - Techniques and Applications.* Berlin: Springer, 2001.

[130] G. P. Celata, M. Cumo, D. Gallo, A. Mariani, and G. Zummo. "A Photographic Study of Subcooled Flow Boiling Burnout at High Heat Flux and Velocity". In: *International Journal of Heat and Mass Transfer* 50 (2007), pp. 283–291.

[131] H. Zhang, I. Mudawar, and M. M. Hasan. "Photographic Study of High-Flux Subcooled Flow Boiling and Critical Heat Flux". In: *International Communications in Heat and Mass Transfer* 34.6 (2007), pp. 653 –660.

[132] C. R. Kharangate, I. Mudawar, and M. M. Hasan. "Photographic Study and Modeling of Critical Heat Flux in Horizontal Flow Boiling with Inlet Vapor Void". In: *International Journal of Heat and Mass Transfer* 55.15-16 (2012), pp. 4154–4168.

[133] T. P. Davies. "Schlieren Photography - Short Bibliography and Review". In: *Optics and Laser Technology* 13.1 (1981), pp. 37–42.

[134] J. M. Desse and R. Deron. "Shadow, Schlieren and Color Interferometry". In: *The Onera Journal Aerospace Lab* 1 (2009), pp. 1–10.

[135] M. J. Hargather, M. J. Lawson, G. S. Settles, and L. M. Weinstein. "Seedless Velocimetry Measurements by Schlieren Image Velocimetry". In: *AIAA Journal* 49.3 (2011), pp. 611–620.

[136] D. R. Jonassen, G. S. Settles, and M. D. Tronosky. "Schlieren "PIV" for Turbulent Flows". In: *Optics and Lasers in Engineering* 44.3-4 (2006), pp. 190–207.

[137] G. Bloch, J. Kuczaty, and T. Sattelmayer. "Application of High-Speed Digital Holographic Interferometry for the Analysis of Temperature Distributions and Velocity Fields in Subcooled Flow Boiling". English. In: *Experiments in Fluids* 55.2 (2014), pp. 1–12.

[138] U. Schnars and W. Jüptner. *Digital Holography.* Berlin/Heidelberg: Springer, 2005.

[139] F. Mayinger. "Heat Transfer at the Phase Interface of Bubbles Collapsing in Subcooled Liquids and During Subcooled Boiling". In: *Heat and Mass Transfer* 42 (2006), pp. 869–874.

[140] A. Lucic and F. Mayinger. "Transport Phenomena in Subcooled Flow Boiling". In: *Heat and Mass Transfer* 46 (2010), pp. 1159–1166.

[141] M. Raffel, C. Willert, and J. Kompenhans. *Particle Image Velocimetry - A practical guide.* Berlin/Heidelberg: Springer, 1998.

[142] A. K. Prasad. "Particle Image Velocimetry". In: *Current Science* 79.1 (2000), pp. 51–60.

[143] J. Chaouki, F. Larachi, and M. P. Dudukovic. "Noninvasive Tomographic and Veloci-metric Monitoring of Multiphase Flows". In: *Industrial and Engineering Chemistry Research* 36 (1997), pp. 4476–4503.

[144] R. Mann, F. J. Dickin, M. Wang, T. Dyakowski, R. A. Williams, R. B. Edwards, A. E. For-rest, and P. J. Holden. "Application of Electrical Resistance Tomography to Interro-gate Mixing Processes at Plant Scale". In: *Chemical Engineering Science* 52.13 (1997), pp. 2087 –2097.

[145] C. Sodtke, J. Kern, N. Schweizer, and P. Stephan. "High Resolution Measurements of Wall Temperature Distribution Underneath a Single Vapour Bubble under Low Gravity Conditions". In: *International Journal of Heat and Mass Transfer* 49.5 (2006), pp. 1100 –1106.

[146] M. Piasecka, B. Maciejewska, and K. Zietala. "Research on Flow Boiling in Minichan-nels with Enhanced Heating Walls Using Liquid Crystal Thermography and Infrared Thermography". In: *Proceedings of the 9th International Conference on Boiling and Condensation Heat Transfer*. Boulder, Colorado, April 26-30, 2015.

[147] A. Megahed. "Local Flow Boiling Heat Transfer Characteristics in Silicon Microchan-nel Heat Sinks using Liquid Crystal Thermography". In: *International Journal of Mul-tiphase Flow* 39 (2012), pp. 55 –65.

[148] D. Hollingsworth. "Liquid Crystal Imaging of Flow Boiling in Minichannels". In: *ASME 2004 2nd International Conference on Microchannels and Minichannels*. ICMM2004-2320. Rochester, New York, 2004, pp. 57–66.

[149] D. B. R. Kenning, T. Kono, and M. Wienecke. "Investigation of Boiling Heat Transfer by Liquid Crystal Thermography". In: *Experimental Thermal and Fluid Science* 25.5 (2001), pp. 219 –229.

[150] C. Gerardi, J. Buongiorno, L. wen Hu, and T. McKrell. "Study of Bubble Growth in Water Pool Boiling through Synchronized, Infrared Thermometry and High-Speed Video". In: *International Journal of Heat and Mass Transfer* 53 (2010), pp. 4185 –4192.

[151] R. Visentini, C. Colin, and P. Ruyer. "Experimental Investigation of Heat Transfer in Transient Boiling ". In: *Experimental Thermal and Fluid Science* 55 (2014), pp. 95 – 105.

[152] Y. A. Hassan, C. E. Estrada-Perez, and J. S. Yoo. "Measurement of Subcooled Flow Boil-ing using Particle Tracking Velocimetry and Infrared Thermographic Technique". In: *Nuclear Engineering and Design* 268 (2014), pp. 185 –190.

[153] D. Krebs, V. Narayanan, J. Liburdy, and D. Pence. "Local Wall Temperature Measure-ments in Microchannel Flow Boiling Using Infrared Thermography". In: *ASME 2008 2nd International Conference on Energy Sustainability collocated with the Heat Trans-fer, Fluids Engineering, and 3rd Energy Nanotechnology Conference*. HT2008-56253. Jacksonville, Florida, USA, August 10-14, 2008.

[154] H.-M. Prasser, A. Böttger, and J. Zschau. "A New Electrode-Mesh Tomograph for Gas-Liquid Flows". In: *Flow Measurement and Instrumentation* 9 (1998), pp. 111–119.

[155] M. Da Silva, E. Schleicher, and U. Hampel. "Capacitance Wire- Mesh Sensor for Fast Measurement of Phase Fraction Distributions". In: *Measurement Science and Technology* 18 (2007), pp. 2245–2251.

[156] S. Sharaf, M. Da Silva, U. Hampel, C. Zippe, M. Beyer, and B. Azzopardi. "Comparison between Wire Mesh Sensor and Gamma Densitometry Void Measurement in Two-Phase Flows". In: *Measurement Science and Technology* 22 (2011), pp. 1–13.

[157] H.-M. Prasser, D. Scholz, and C. Zippe. "Bubble Size Measurement Using Wire-Mesh Sensors". In: *Flow Measurement and Instrumentation* 12.4 (2001), pp. 299–312.

[158] M. Utiger, C. Guy, F. Stuber, A.-M. Duquenne, and H. Delmas. "Local Measurements for the Study of External Loop Airlift Hydrodynamics". In: *The Canadian Journal of Chemical Engineering* 77.2 (1999), pp. 375–382.

[159] T. Lüttich, W. Marquardt, M. Buchholz, and H. Auracher. "Identification of Unifying Heat Transfer Mechanisms Along the Entire Boiling Curve". In: *International Journal of Thermal Sciences* 45 (2006), pp. 284–298.

[160] A. Cartellier. "Optical Probes for Local Void Fraction Measurements: Characterization of Performance". In: *Review of Scientific Instruments* 61 (1990), pp. 874–886.

[161] A. Cartellier. "Simultaneous Void Fraction Measurement, Bubble Velocity, and Size Estimate Using a Single Optical Probe in Gas- Liquid Two- Phase Flows". In: *Review of Scientific Instruments* 63 (1992), pp. 5442–5453.

[162] A. Cartellier. "Measurement of Gas Phase Characteristics Using new Monofiber Optical Probes and Real-Time Signal Processing". In: *Nuclear Engineering and Design* 184 (1998), pp. 393–408.

[163] A. Cartellier. "Optical Probes for Multiphase Flow Characterization: Some Recent Improvements". In: *Chemical Engineering and Technology* 24.5 (2001), pp. 535–538.

[164] A. Cartellier and J. L. Achard. "Local Phase Detection Probes in Fluid/Fluid Two- Phase Flows". In: *Review of Scientific Instruments* 62 (1991), pp. 279–303.

[165] A. Cartellier and E. Barrau. "Monofiber Optical Probes for Gas Detection and Gas Velocity Measurements: Conical Probes". In: *International Journal of Multiphase Flow* 24 (1998), pp. 1265–1294.

[166] M. Hong, A. Cartellier, and E. J. Hopfinger. "Characterization of Phase Detection Optical Probes for the Measurement of the Dispersed Phase Parameters in Sprays". In: *International Journal of Multiphase Flow* 30 (2004), pp. 615–648.

[167] P. C. Mena, F. A. Rocha, J. A. Teixeira, P. Sechet, and A. Cartellier. "Measurement of Gas Phase Characteristics Using A Monofibre Optical Probe in a Three-Phase Flow". In: *Chemical Engineering Science* 63 (2008), pp. 4100–4115.

[168] J. Vejrazka, M. Vecer, S. Orvalho, P. Sechet, M. C. Ruzicka, and A. Cartellier. "Measurement Accuracy of a Mono-Fiber Optical Probe in a Bubbly Flow". In: *International Journal of Multiphase Flow* 36 (2010), pp. 533–548.

[169] G. Bloch, J. Elfner, K. Finke, and T. Sattelmayer. "Setup and Fabrication of Cost Effective, Robust Fiber Optical Needle Probes for Application in Multiphase Flows". In: *Lasermethoden in der Strömungsmesstechnik*. München, Germany, 2013.

[170] H.-J. Lim, K.-A. Chang, C. B. Su, and C.-Y. Chen. "Bubble Velocity, Diameter, and Void Fraction Measurements in a Multiphase Flow Using Fiber Optic Reflectometer". In: *Review of Scientific Instruments* 79 (2008), pp. 1–11.

[171] L. Liao, R. Bao, and Z. Liu. "Compositive Effects of Orientation and Contact Angle on Critical Heat Flux in Pool Boiling of Water". In: *Heat and Mass Transfer* 44.12 (2008), pp. 1447–1453.

[172] E. J. Julia, W. K. Harteveld, R. F. Mudde, and H. E. A. Van den Akker. "On the Accuracy of the Void Fraction Measurements Using Optical Probes in Bubbly Flows". In: *Review of Scientific Instruments* 76 (2005), pp. 1–13.

[173] M. Löffler-Mang. *Optische Sensorik: Lasertechnik, Experimente, Light Barriers.* Vieweg+Teubner Verlag, 2012.

[174] T. Saito, K. Matsuda, Y. Ozawa, S. Oishi, and S. Aoshima. "Measurement of Tiny Droplets Using a Newly Developed Optcal Fibre Probe Micro- Fabricated by a Femtosecond Pulse Laser". In: *Measurement Science and Technology* 20 (2009), pp. 1–12.

[175] C. Morel, N. Goreaud, and J.-M. Delhaye. "The Local Volumetric Interfacial Area Transport Equation: Derivation and Physical Significance". In: *International Journal of Multiphase Flow* 25.6 (1999), pp. 1099 –1128.

[176] J. Hartung, B. Elpelt, and K.-H. Klösener. *Statistik: Lehr- und Handbuch der angewandten Statistik.* De Gruyter Oldenbourg, June 3, 2009.

[177] D. A. Drew and R. T. Lahey. "Phase-distribution Mechanisms in Turbulent Low-quality Two-phase Flow in a Circular Pipe". In: *Journal of Fluid Mechanics* 117 (1982), pp. 91–106.

[178] A. Tomiyama, H. Tamai, I. Zun, and S. Hosokawa. "Transverse Migration of Single Bubbles in Simple Shear Flows". eng. In: *Chemical Engineering Science* 57.11 (2002), pp. 1849–1858.

[179] D. Bothe, M. Schmidtke, and H.-J. Warnecke. "VOF-Simulation of the Lift Force for Single Bubbles in a Simple Shear Flow". In: *Chemical Engineering & Technology* 29.9 (2006), pp. 1048–1053.

[180] Y. M. Kwon and S. H. Chang. "An Improved Mechanistic Model to Predict Critical Heat Flux in Subcooled and Low Quality Convective Boiling". In: *Journal of the Korean Nuclear Society* 31.2 (1999), pp. 236–255.

[181] J. Griffel and C. F. Bonilla. "Forced-Convection Boiling Burnout for Water in Uniformly Heated Tubular Test Sections". In: *Nuclear Structural Engineering* 2.1 (1965), pp. 1 – 35.

[182] H. Zhang, I. Mudawar, and M. M. Hasan. "Investigation of Interfacial Behavior During the Flow Boiling CHF Transient". In: *International Journal of Heat and Mass Transfer* 47.6-7 (2004), pp. 1275–1288.

[183] NUBEKS Consortium and C. Hirsch. *Summary Report: CFD-Methoden zur Berechnung der Kritischen Wärmestromdichte (NUBEKS), FKZ 1501473 A-D.* Tech. rep. Technische Universität München, 2019.

[184]   W. Polifke and J. Kopitz. *Wärmeübertragung: Grundlagen, Analytische und Numerische Methoden.* München: Person Studium, 2009.

[185]   W. M. Kays and M. Crawford. *Convective Heat and Mass Transfer.* 2nd ed. New York: McGraw-Hill, 1980.

[186]   A. Richenderfer, A. Kossolapov, J. H. Seong, G. Saccone, E. Demarly, R. Kommajosyula, E. Baglietto, J. Buongiorno, and M. Bucci. "Investigation of Subcooled Flow Boiling and CHF using High-Resolution Diagnostics". In: *Experimental Thermal and Fluid Science* 99 (2018), pp. 35 –58.

[187]   J. Blum, T. Lüttich, and W. Marquardt. "Temperature Wave Propagation As a Route from Nucleate to Film Boiling?" In: *Two-Phase Flow Modelling and Experimentation 1999 : Proceedings of the 2. International Symposium on Two-Phase Flow Modelling and Experimentation.* Vol. 1. Rome, Italy, 23-26 May, 1999, pp. 137–144.